

BOSTON UNIVERSITY
GRADUATE SCHOOL OF ARTS AND SCIENCES

Dissertation

**MEASURING NEURON/GLIAL CELLULAR ARRANGEMENT IN THE
MAMMALIAN CORTEX**

by

ANDREW INGLIS

B.S., University of Virginia, 2000

M.A.T., Johns Hopkins University, 2002

Submitted in partial fulfillment of the
requirements for the degree of
Doctor of Philosophy

2010

Approved by

First Reader

H. Eugene Stanley, Ph.D.
University Professor and Professor of Physics

Second Reader

William J. Skoepol, Ph.D.
Professor of Physics

To Howard, my father, Karl, my grandfather, and Steve, my friend.

I am here because of you.

Acknowledgments

MEASURING NEURON/GLIAL CELLULAR ARRANGEMENT IN THE MAMMALIAN CORTEX

(Order No.)

ANDREW INGLIS

Boston University Graduate School of Arts and Sciences, 2009

Major Professor: H. Eugene Stanley, University Professor and Professor of Physics

ABSTRACT

The spatial arrangement of cells in the mammalian cortex directly relates to how the brain performs functionally. These cells include neurons, the fundamental building block of the neural network, and glia, which provide regulation, insulation, mechanical support, and nutrition for neurons and their processes. Currently, most analyses of pathological changes in spatial arrangement of neuron and glial cells rely on aberrations of cell placements large enough to be visible by the naked eye. We present a method that enables quantification of subtle spatial arrangement properties, or patterns, which exist right above biological noise and that may not be visually apparent due to the pattern's subtlety or lack of spatial cohesion. This method enables new comparisons between functional behavior of brain regions and quantitative measurements of detailed morphology within those regions. The method requires a three-fold effort of digitization, recognition, and analysis: we first develop the experimental platform needed to digitize tissue automatically at high resolution ($1\mu m$ per pixel) throughout whole tissue samples spanning the entire brain. We then develop the algorithms necessary to recognize cells within this digitized tissue, focusing on the challenge of delineating between neuron and glial cells in the same tissue sample. Finally, we show the analysis methods that are enabled by the new dataset. Among the methods are traditional measurements of total cell count and density, microcolumnar arrangement of neurons, and cross-correlation analysis between two cell populations such as neurons

and glial cells. These measurements are either taken in known regions of the cortex or as “running windows” which show changes in spatial properties through the tissue irrespective of region delineations. The statistical robustness of the method is validated by comparing the results with models of multiple cell populations and changing spatial properties. We use the method to analyze cortical tissue samples from the rat and Rhesus monkey, and discuss current theories on mechanisms within the brain that may affect spatial arrangement of cells. Lastly, we describe future directions of study.

Contents

1	Introduction	1
1.1	Studying the brain with the brain	1
1.2	A need for quantitative spatial arrangement tools	3
1.3	Overview of the Dissertation	7
2	Theory and Literature Review	14
2.1	Brain Anatomy Review	14
2.1.1	Cell types in the brain	14
2.1.2	Basic anatomy	17
2.2	Spatial arrangement	17
2.2.1	Development	17
2.2.2	Aging and Disease	20
2.2.3	Mechanisms	21
2.2.4	Cortical Microcolumn	22
2.3	Measurement Theory	25
2.3.1	Raw Data	25
2.3.2	Stereology	28
2.3.3	Correlation measurements	29
3	Experimental Method	42
3.1	Introduction	42
3.2	Methods	45

3.2.1	Image Input and Preprocessing	45
3.2.2	Main segmentation tool: OSM	47
3.2.3	Step I: Image Acquisition	58
3.2.4	Step II: Segmentation Training	58
3.2.5	Step III: Application	60
3.2.6	Comparison method	62
3.2.7	Density Map Method and Microcolumnar Strength	62
3.3	Results	63
3.4	Discussion	69
3.5	Software	72
3.6	Validation by comparing with Stereology	72
4	Results	75
4.1	Macaque Monkey	75
4.1.1	Subjects	75
4.1.2	Area 46 Dorsal Ventral Studies	76
4.1.3	Area TE Studies	83
4.1.4	Area TE Comparison with model	86
4.2	Rat Tissue	93
	Appendices	97
	Bibliography	98
	Curriculum Vitae	107

List of Figures

1.1	Method Phase Space	2
1.2	Epileptic Seizure Displasia	4
1.3	Example of the measurement of the columnarity of neurons	5
2.1	Examples of neurons	15
2.2	Examples of glial	16
2.3	Theory of glial-neuron interactions	18
2.4	Side view of the brain	19
2.5	Human development from 0 to 2 months gestation	20
2.6	Example of microcolumnar structure	23
2.7	Example of tissue	26
2.8	Example of tissue with cell locations	26
2.9	Properties of cells	27
2.10	Region of interest	27
2.11	Stereological sample	28
2.12	Correlation mapping sample	30
2.13	Coordinate space to density map space	31
2.14	Raidal correlation between neurons and glial cells	32
2.15	Density maps for common dementias	33
2.16	Microcolumnar measures	34
2.17	Quantifying microcolumnar measures	35
2.18	Map analysis of tissue properties	36

2.19	Running Window analysis of tissue properties	37
2.20	Running Window measurement example	38
2.21	Additinal correlation measurements	38
2.22	Required cell numbers for correlation analysis	40
3.1	Challenges of automated neuron recognition	44
3.2	Automated Neuron Recognition Algorithm (ANRA)	46
3.3	Image pre-processing	48
3.4	Steps of the overall segmentation method (OSM)	50
3.5	Active contour control points	52
3.6	Examples of active contour movement	53
3.7	Energies of active contour during movement	55
3.8	Control point movement	55
3.9	Overlap of segmentations	61
3.10	Receiver operating characteristic (ROC)	61
3.11	Recognition quality definitions	65
3.12	Active contour segmentation results	65
3.13	Detailed active contour segmentation results	66
3.14	ANRA / semiautomatic comparison	68
3.15	Comparison of ANRA with stereology for a neuron counting study	73
4.1	Raw data overview, 46dv, female monkey	77
4.2	Average values of measures of microcolumnarity	78
4.3	Microcolumnar relationships in area 46 of the female monkey	79
4.4	Microcolumnar strength in dorsal vs. ventral portion of the brain	80
4.5	Microcolumnar strength in relation to behavior	82
4.6	Data Aquisition for area TE	84
4.7	Raw data overview, TE, female monkey	85

4.8	Microcolumnar relationships in area TE of the female monkey, compared with 46dv	85
4.9	Microcolumnarity of TE vs age, compared with 46dv	86
4.10	Schematic diagram showing the variables in the model	87
4.11	Schematic diagram and example figures showing the rotation and cutting of one realization of the model neuronal block	88
4.12	Front and top view of examples of model neuron configurations	89
4.13	Correlations of microcolumnar properties with each other and density . . .	91
4.14	Model generation to align with features of area TE	92
4.15	Depiction of 5 million neuron and glial locations within the rat brain	94
4.16	Probe analysis focusing on different layers of the rat cortex	96

List of Abbreviations

ANRA	Automatic Neuron Recognition Algorithm
SS	Somatosensory Cortex
MC	Motor Cortex
FCD	focal cortical displacias
ROI	region of interest

Chapter 1

Introduction

1.1 Studying the brain with the brain

The past decade has witnessed a surge in research effort dedicated to investigating the mammalian brain. In addition to the large motivating factor of understanding how our minds work, the surge is supported by an continually advancing set of computer aided measurement tools to allow higher resolution and more complex measurements. Even with the increased effort and technology, however, there still remains only a handful fundamental ways to measure brain activity, processes and makeup (ie: fMRI, stereology, individual neuron potentials, etc.). These methods contribute distinct measurements of the brain by falling within particular ranges of three scales: spatial, ranging from inches to nanometers, temporal, ranging from years to milliseconds, and extent scale, ranging from individual neuron measurements to whole brain measurements. It is worth noting that no measurement tool is maximized in all three categories. For example, while fMRI measurements span the entire brain, the spatial resolution only allows the combined effect of hundreds of neurons firing together to be resolved. Another example, individual neuron voltage measurements, have a high temporal resolution within the millisecond range, but cannot identify single neurons, and only extends thousands of neurons, or cubic millimeters, of volume. All in all, researchers have attempted to fill this phase space in order to leave no stone unturned in the difficult task of understanding brain processes.

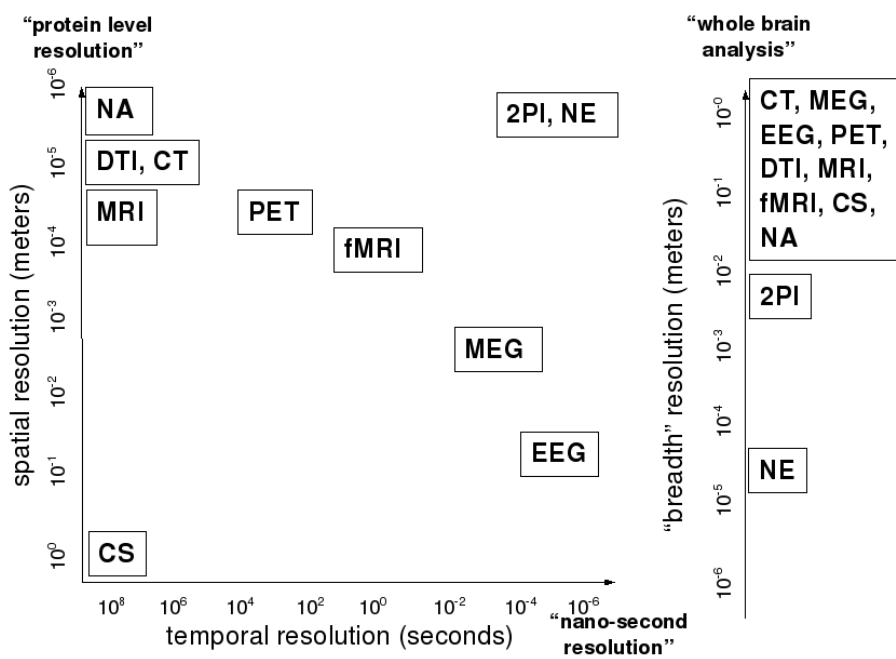


Figure 1.1: Symbols stand for the following things: neuroanatomy (NA), diffusion tensor imaging (DTI), computed tomography (CT), magnetic resonance imaging (MRI), positron emission tomography (PET), functional magnetic resonance imaging (fMRI), two-photon imaging (2PI), needle electrodes (NE), magnetoencephalography (MEG), electroencephalography (EEG), case studies (CS).

We add a fundamentally new way to understand the brain by shedding light on a previously unmeasured area within this triptych of temporal scale, spatial scale, and extent. By collecting individual neuron and other cell body properties (such as glial cells) of location, size, and shape, from every neuron within an extent of the entire brain at micron resolution, we are able to create a map of spatial arrangement properties of the cell bodies with respect to each other throughout the entire cortex.

1.2 A need for quantitative spatial arrangement tools

In a recent special issue of *Child's Nervous System*, researchers and doctors gave an update on the best methods for treating children with severe epileptic seizures (Hildebrandt et al., 2005). Two reports in the issue gave overviews of an affect called *focal cortical displacias*, which means that there are drastic changes (*displacias*) that occur in the local (*focal*) arrangement of cells in the regions that are affected by the seizures (*cortical*) (Rickert, 2006; Rocco and Tamburrini, 2005). In the task of stopping seizures from occurring, understanding these “subtle but statistically significant neuroanatomical abnormalities” (Hildebrandt et al., 2005) is a fundamental step to understanding how the seizures occur, how they damage the brain, and how to stop them in the future. An interesting example is that of a heightened tendency for neurons to align vertically into so-called microcolumns (described in detail later) in areas of that experienced epileptic activity compared to those that did not (Fig. 1.2).

Many questions arise from the findings of this study. How is the alignment of the neurons related to the epileptic firing of that particular brain area? Are brains with higher columnarity more prone to epileptic activity, or is the columnarity an affect of the seizures? How is the structure of the neurons hint to how the neurons are connected with one another? The answers to these and many other questions can come in many forms, such as performing the analysis on many more human subjects, by recreating the effect of epileptic seizure in another animal type, such as a rat, or by modelling the connections of the neurons *en silica* (with computers).

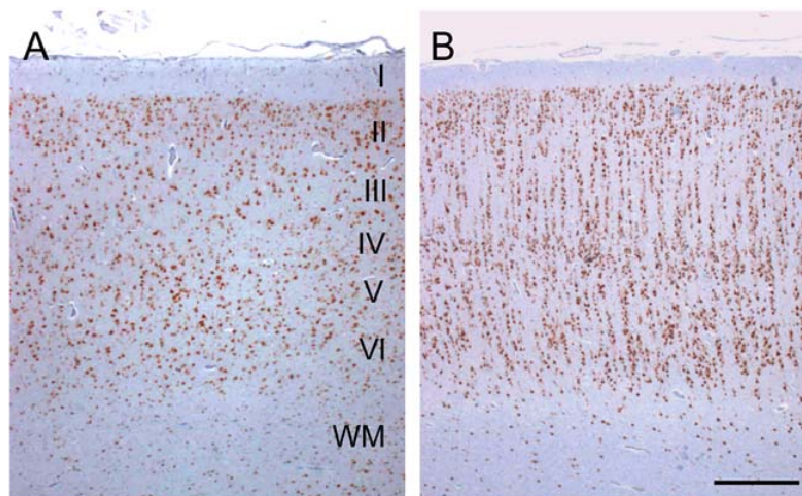


Figure 1.2: Cortical architecture in a young control specimen (A) vs a patient with catastrophic epilepsy, showing prominent columnar arrangements of cortical neurons. *Reproduced from Hildebrandt et al. (2005).*

There is a fundamental question that underlies the exploration of all of these questions: How can the spatial arrangement patterns within the brain be measured quantitatively? Quantitative analysis is needed in order to build upon the investigation in a scientifically coherent manner. We could make a distinction between a qualitative measurement of a spatial pattern (ie: “the neurons are aligned into columns”) and a quantitative one (ie: “the neurons are aligned X%, where 0% is no alignment, and 100% is complete alignment”). The former result can only motivate other researchers to study the system with more quantitative analysis, and the latter creates a base analysis that can be expanded and built upon: the measurement can be compared with others in other studies, statistical significance between two populations can be determined, ranges of the measurement can be related to ranges in functional behavior of the system, new studies can change the system and see the effect of the measurement, rudimentary correlations between variables can be constructed, new hypothesis can be constructed, and so on.

With this benefit of quantitative analysis in mind, Hildebrandt et al. (2005) provide such a measurement: The visual field of the images was divided into horizontal segments of

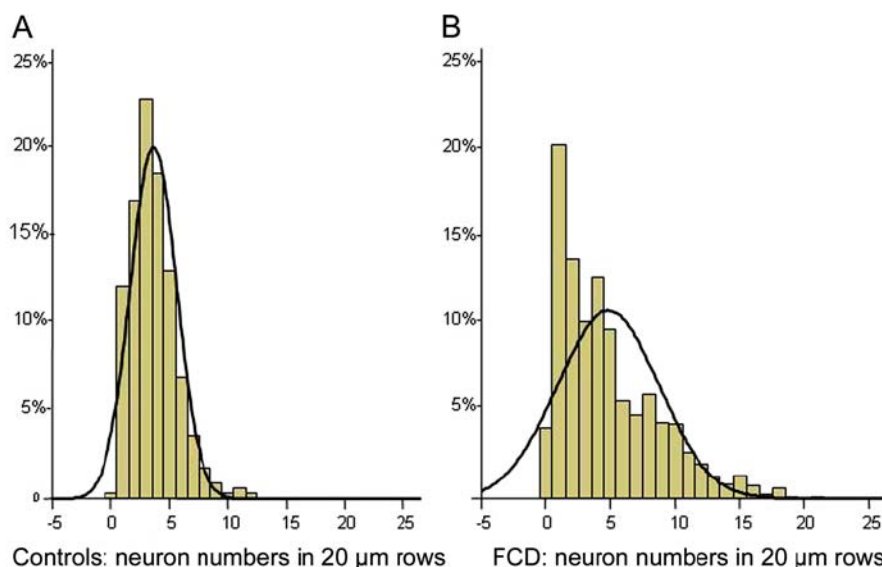


Figure 1.3: Gaussian distribution of vertically oriented neuronal cell cluster in FCD and controls. Mean neuronal numbers are higher in FCD specimens compared to controls. The variance of neuron numbers is also significantly broader in specimens with FCD compared to controls. *Reproduced from Hildebrandt et al. (2005).*

20 μm width (according to the average diameter of NeuN-stained cortical neurons in lamina III). The numbers counted were then histogrammed (Fig. 1.3). A difference between the two populations can clearly be seen, and a statistically significant difference can be seen in the numbers.

Hildebrandt et al. (2005)'s methods are an example of a new desire of neuroanatomists to go beyond the traditional methods available to them in the field of neuroanatomy. Traditionally, a method called *stereology* has been used to analyze brain tissue. Stereology is a powerful sampling algorithm that measures a property in defined regions of interest (ROI) of the brain by only requiring a small sample of that ROI to be measured accurately by a researcher. An analogous situation is to determine the total number of people that use a building's entrance in a week by only picking several five minute intervals to count, and scaling the result up by multiplying by the ratio of one week's time to how long was measured. If done correctly, an unbiased measurement can be performed, which is exactly what

Stereology offers to the field of neuroscience (Mayhew, 1991; Schmitz and Hof, 2005).

Although there are many benefits, stereology has some limitations for studies that involve comparatively large ROIs and large number of subjects. The time and effort required to perform stereology limits the number of areas and questions that can be studied. Also, the stereologist performing the study must be vigilant against shifting cell selection criteria throughout the experiment (an issue known as experimental drift).

Most importantly, stereology only can measure so-called “first order” stereological parameters like total cell count, which only partially describe the structural organization of the brain. It cannot in its current form efficiently quantify so-called “second order” parameters that measure more complex spatial properties of neuron organization, such as the cortical changes occurring in the epileptic study. In addition to the epileptic study (Hildebrandt et al., 2005), other recent findings show that the heterogeneity of spatial patterns among cells is also important to understanding cortical organization and potential alterations in aging or other conditions (Asare, 1996; Schmitz et al., 2002; Duyckaerts and Godefroy, 2000; Krasnoperov and Stoyan, 2004; Hof et al., 2003; Urbanc et al., 2002; Cruz et al., 2005; Buldyrev et al., 2000; Buxhoeveden and Lefkowitz, 1996).

In thinking of new types of measurements of cortical tissue, one can learn much from the very strong attributes of Stereology. First, it can be unbiased, which means that the measurements are not affected by systematic errors that can deviate the results in unknown ways. Secondly, the algorithm is able to quantify its ability to discern subtle differences, and its discernability can be adapted by sampling more tissue. Lastly, it is able to measure through the entire brain. It is these three properties that make stereology such a powerful method. It is our goal to incorporate these properties into a measurement tool for “second order”, spatial arrangement properties of the brain.

We attempt to satisfy such qualities by automatically collecting individual neuron and other cell body properties (such as glial cells) of location, size, and shape, from every neuron within an extent of the ROI. The automatic nature of the measurement allows it to be performed in large datasets, and reduces biases that are attributal to experimental drift

mentioned earlier. It also allows for measurements based on the highest level of statistics as possible, in order to have the highest level of discernability above biological noise. The basic pillars of stereology thereby (attempted) to be covered, we also mention an additional and exciting quality of such a method: *it moves the neuroanatomical exploration of the brain away from a hypothesis driven model to a more of a data driven model*. Due to the time consuming nature of stereology, studies that investigate detailed anatomy are resource intensive, therefore only the most salient investigations which have been heavily prepared for, are performed. The ability to perform quick hypothesis driven questions, or to search for unknown correlations is not available in the field. Our method enables such studies in the neuroanatomy research, and therefore can open new understandings of anatomical organization than can be thought of by researchers.

There are several technologies that are allowing this type of analysis is being developed now. First, the data storage and retrieval capacities needed to inexpensively store terabytes of image data of brain tissue has only recently become available. Also, the computing power to measure millions of neuron properties from slices of brain tissue in a timely manner has also only recently become available. Furthermore, the advances in CCD imaging technology and computer operated microscope stages now allow for high speed digitization of the tissue to be automatically analyzed by a computer. Lastly, efficient machine learning algorithms have become advanced enough to solve complex automatic recognition problems. This type of development in fast computing and storage space is commonly known to have revolutionized the study of genetics and computer science, but is also advancing brain sciences in this project and others, most notably that of the Allen Institute for Brain Science.

1.3 Overview of the Dissertation

In this first chapter of this Dissertation, we have given a motivation for the need to be able to measure subtle patterns of cellular arrangement in the brain, and have given a brief overview of the our method.

In Chapter 2 we further motivate the main investigation of spatial arrangement of brain cells by reviewing known and possible sources of cell arrangement features within the brain, then describe the the discernment of such such hypthesis to be studied. We then review the mathematical framework used in the analysis.

In Chapter ?? we motivate and describe the new experimental tool to collect data from the brain, called the Automatic Neuron Recognition Algorithm, or ANRA. Individual locations of many neuronal cell bodies ($> 10^4$) are needed to enable statistically significant measurements of spatial organization within the brain such as nearest-neighbor and micro-columnarity measurements, as well as enable investigations on the heterogeneity of neuron properties within a given region. As mentioned earlier, the acquisition of such numbers of neurons by manually or semi-automatically identifying and marking the location of each is prohibitively time-consuming and open to user bias. ANRA is the experimental technique that allows the acquisition of such large numbers of neuron properties with the maximal efficiency and accuracy afforded by current computing techniques.

ANRA automatically obtains the (x,y,z) location of individual neurons within digitized images of single or multiple stained tissue. Nissl-staining has the unique advantage of being the least expensive, easiest applied, and most durable method for staining both neurons and glia, and vast stores of archival material that exist in laboratories and research collections around the world. Proper identification of neurons within such Nissl-stained sections is inherently difficult however due to the variability in neuron staining, the overlap of neurons, the presence of partial or damaged neurons at tissue surfaces, and the presence of non-neuron objects, such as glial cells, blood vessels, and random artifacts. To overcome these challenges and identify neurons, ANRA applies a combination of image segmentation and machine learning (A. Inglis and Rosene, 2008). The steps involve “teaching” the computer to find cells by giving it examples, then the computer performing color selection on the tissue (in the case of counter-stained tissue), segmentation to find outlines of potential neuron and glial cell bodies, then artificial neural network training using the segmentation properties (size, optical density, gyration, etc.) in order to distinguish between neurons,

glia, and non-neuron segmentations.

Furthermore, ANRA allows the user to explore various segmentation and training methods that give the optimal result for varying image type and quality. It then stores the parameter selection and training created by the neuro-anatomist in order to be reused as similar areas of other serial sections to be analyzed. The end result is a platform that combines the most advanced machine learning and segmentation technology available today in order to analyze readily available tissue samples and create datasets of millions of neuron properties for further analysis.

Through the control of a motorized stage, images are acquired with a slight overlap, allowing the creation of whole hemisphere photomontages that can serve as input to any of our proposed analyses. Neurons are automatically found within the montage using ANRA on large regions of the brain using a single coordinate system, rather than thousands of disjointed images. The viewing interface for ANRA allows the researcher to fly through the montaged tissue samples and neuron measurement results similar to BrainMaps.org (S. Mikula and Jones, 2007). This enables researchers and expert neuroanatomists to perform the host of experimental techniques on the project such as machine training, verification, marking traditional boundaries, making contours to perform running window analysis, and organize data storage during the data acquisition process. It also enables the user to display the results of the correlative analysis in a topographical manner. A further advance is to use to acquire the images at multiple distances from the microscope objective, which allows the retrieval of the z component of the neuron information.

In Chapter ?? We describe the new measurements motivated by statistical physics that are used on the experimental data. As described in the previous section, the data that we want to analyze is millions of neuron properties such as location, size and shape. As within many fields of physics, our goal is to condense the inherent complexity and biological variability of this system by condensing the information into single measurements, but also be careful not to throw out meaningful qualities and information during the process. We investigate and use several analysis tools, ranging from traditional density and neuron count,

to histogram distributions of properties, to multi-dimensional correlative analysis.

We start by showing how the overall method can recreate the methods of stereology, and also add additional insight to the traditional methods by enabling heterogeneities of traditional features such as density and count to be seen in the ROI. We then move to pair-correlation analysis, which observes the relationships between particles rather than just the average properties of individual particles in a system. Such measurement's ability to glean illustrative properties of noisy complex systems of particles make them appealing as tools to study biological systems with many particles such as neurons. Pair correlation methods have been used to explore relationships between two different types of objects such as neurons and neurofibrillary plaques (Urbanc et al., 2002), and explore the relationship between neuron cell bodies (Buldyrev et al., 2000). By using a two-dimensional pair-correlation involving the relative separations of neurons, we discover the tendency for neurons to align perpendicularly to the cortex surface, and are able to measure discerning properties of spatial arrangement, such as the strength of microcolumnar order and microcolumnar width and length (Cruz et al., 2005). In addition to these correlation methods, which use the locational spatial properties, we also investigate correlations using the measured size and shape properties which can give axon/dendrite process directions and neuron/cell type information. We also investigate cross correlations between glial cells and neurons.

Motivated by the heterogeneous nature of spatial arrangement properties, we develop a method of exploring changing properties as one probes in a linear dimension through the cortex. Because of the photomontaging ability, we are able to measure changes of spatial arrangement features seamlessly across tens of thousands of microns. Because of the intrinsic curvature of the cortex, we create tracks using the visualization system that serve as a guide to our running window analysis. Once the tracks have been defined, a "running window", or section of the track, is selected, and the x,y locations acquired with ANRA within the running window are used for spatial measurements. The analysis window is lengthened or shortened depending on the number of data points (neurons) that are needed for a statistically significant measurement.

Because of the biological noise, recognition error (from the automatic recognition measurements), and the dependence of the statistical measurements on the complex coordinate system of the brain, there is a need to validate the data recognition and measurement tools on a model system. This type of study allows us to be as true to the high standards that stereology has brought to the study of neuroanatomy by determine the effects of recognition and orientation on the ability to discern subtle changes in the measurements as we either probe the tissue, or pass across the tissue in a “running window” analysis. One main goal is to determine what amount of variation from the real values (values obtained if unlimited data of similar spatial arrangement was available) occurs depending on how many particles are incorporated in a given measurement. This variation determines the resolution we can see changes in neuron spatial organization across the cortex. We investigate this relationship between noise, sample size and resolution for all of the measures implemented in the study. We investigate these properties explicitly by introducing known distributions of noise into the analysis calculations. We also empirically determine variance levels by modeling biological and recognition variance into a model of neuron organization .

In Chapter ??, we review results that we have obtained from the initial use of statistical techniques, give initial results using the new method, and describe the future studies that will be performed.

Also, we first show a comparative study of the counting of neuron and glial numbers retrieved from both stereology and ANRA in the supragranular, granular and infragranular laminar subdivisions of the monkey primary visual cortex. the same ROIs within the same tissue sections, and use the stereological windows and enumerated cells as a gold standard to determine recognition accuracy of ANRA throughout the cases. The result shows that ANRA performs as good as stereology counting cells, motivating the use of ANRA to replace stereology for more traditional studies.

We also show results of ANRA on the analysis to Nissl-stained sections of adult Fischer-344 rat somatosensory cortex revealed a microcolumnar strength of 1.10, exceeding a value of 1.00 which indicates a non-columnar, uniform distribution. These data provide evidence

for an identifiable, statistical tendency among neurons to be organized into microcolumns in rat neocortex. Extension of these methods to compare the cortex of young and old rats will allow determination of whether rat cortex shows age-related changes in microcolumns and if there is region selective vulnerability.

We then review the studies involving the Macaque monkey data provided by the BU Department of Neuroanatomy. The functional data consists of a battery of tests performed by the subjects relating to cognitive ability in specific brain areas. For such comparisons, we attempt to find the observed relationships between changes in the spatial arrangements of cell bodies with age and cognitive ability using correlative analysis. Without the automated methods described in this dissertation, the numerous correlations combined with the relatively small number of subjects for each correlative test make it difficult to minimize both Type 1 (finding correlations that are not there) and Type 2 (throwing out a correlation) errors to make an overall interpretation from the data. We show how the problem is reduced by increasing the subject data using the automation capabilities of ANRA. In future investigations we will include data aided by the ANRA platform to acquire an order of magnitude more neuron locations than previous studies (one million neuron locations) from a sample of 50 Macaque monkey subjects. The goal in this study is to quantify the important spatial organization in the cortex of the monkeys to determine how values of the measures vary across and within known cytoarchitectonic regions, and thus correlate with function. This will also identify areas that change with age and allow examination of the relationship of changes in multiple regions with age-related cognitive impairments. We will also analyze those areas in the cortex showing significant age-related changes in neuron organization for specific changes in their dendrite structure and structure of the supporting matrix of glia cells.

We also describe the further integration of modelling into the analysis, especially by “branching” into networking analysis on the model of neuron location in order to discover how subtle arrangement pattern and shifts in these patterns influence the connective properties of the nodes. For this study, the model is extended to incorporate different neuron

types, sizes, and orientation , in order to allow important complexities to influence the network structure. We move from simple to more complex scenarios of node placement (grid, randomized, neuron model block), network connectivity (static radius of connectivity, distributions, experimentally motivated (?), and analysis tools (average path length, connection type distributions, degree correlations). We finally apply such tools to our models of brain aging in order to explore how connective structure is affected by changing node (neuron cell body) organization.

Chapter 2

Theory and Literature Review

In this chapter we will further motivate our overall method by reviewing current challenges of investigating the cortex using traditional spatial arrangement methods then introducing the theory behind our new methods as an additional and necessary tool. This chapter also reaffirms the study of neuroanatomy as one of the most powerful fields to investigate the brain, even with the advent of newer methods as described in section 1.1.

2.1 Brain Anatomy Review

2.1.1 Cell types in the brain

The two major cell types in the brain are neurons and glial cells.

Neurons are thought to be the fundamental building block of the electrical network that produces the major actions of the brain, such as sensory input, motor control, memory, and consciousness. Neurons share a common set of properties that have led researchers to believe that they are the fundamental processing unit of the brain. These features are the so called “processes” that emit from the main part of the cell body and which connect to other neuron cell bodies. The two main categories of processes are those that receive information from other neurons called *dendrites*, and processes that transmit information to other cells called *the axon*. There are usually many dendrites, and usually one axon. The neuron therefore is thought to “integrate” all of the signals that enter from the dendritic processes, and use

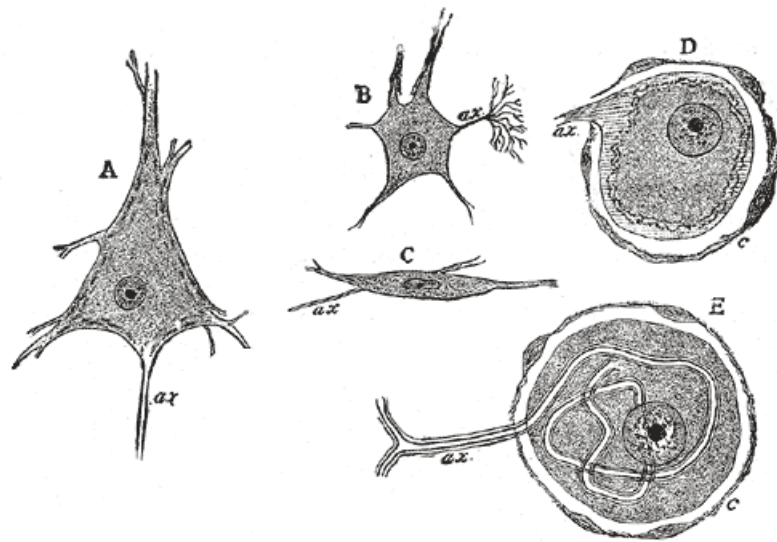


Figure 2.1: Examples of neuron shape, size, and type. A. Pyramidal cell. B. Small multipolar cell, in which the axon quickly divides into numerous branches. C. Small fusiform cell. D and E. Ganglion cells (E shows T-shaped division of axon). ax. Axon. c. Capsule. *Reproduced from Gray (1918)*

this information to “decide” whether, and how, to fire it’s own signal from its axon, a signal that is then picked up by the dendrites of other processes. The signals that enter the cell body from the dendrites (and sometimes from the surface of the cell body) do not affect this firing decision of the cell equally, rather have different “weights” based on the intensity of the input signal, the temporal pattern of the signal (the neurons can fire with pulses of different frequencies), the location of the signal along the dendritic processes (or the cell body). Neuron cells can be very differently volumed (having diameters from 2 – 200 μm) and differently shaped (having 1-100 processes coming off of their cell bodies, and those processes spanning very short distances - 10’s of μm to nearby neuron cell bodies to meters to cells in different areas of the brain). Lastly, the firing properties of neurons are created by certain types and combinations of neurotransmitting elements.

There have been numerous categorizations of neurons according to shape, location, and behavior (Abeles, 1991; Braitenberg and Shuz). For our purposes, we can mention the

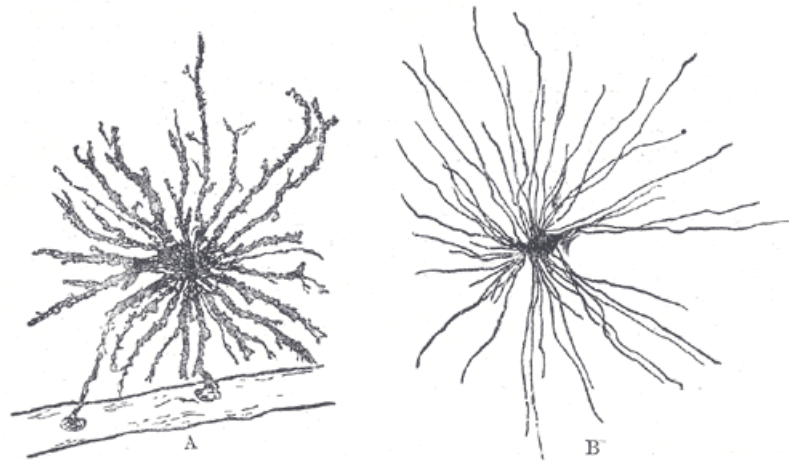


Figure 2.2: Examples of astrocyte glial cells. *Reproduced from Gray (1918)*

main categorizations of neurons: those that interact only with other neurons in the brain region that they are located, or in their vicinity (stellate cells) vs. those whose processes leave the given section of tissue (pyramidal cells), and those that reduce the chance of activity in the cells whose dendrites their axon is attached to (inhibitory) vs those that increase the chance of activity in the cells whose dendrites their axon is attached to (excitatory).

Glial cells are the other, lesser known and studied cell population within the brain, although they comprise half of the total cell count within the brain. Glial cells are known to play a supportive role for neurons, and are usually broken into 3 main categories. “Oligodendrites” provide support for the myelin sheaths that preserve the potentiation inside of the axonic process for the neurons. “Astrocytes” connect neurons with the blood supply (as vessels inside the brain). “Microglia” recycle dead cells and unused cell tissue from the cortex.

Because glial cells do not communicate in this traditional neuron-like manner where cells fire based on an integration of signal from the dendrites, and because of the other straightforward purposes described in the previous paragraph, they have not been studied as thoroughly as the neuron population in terms of the network of the brain. However, other than this ability to fire and action potential, glial cells have been shown to possess features

that can directly affect the network of the brain. Astrocytes have been shown to receive signals similar to dendritic process of neurons, many of the other features of neurons, such as neurotransmitters, which allow it to communicate with the neural network (Fields and Stevens-Graham, 2002; Bezzi and Volterra, 2001).

For this reason, along with the arguments spelled out in Sec. 2.2.1 when exploring spatial arrangement within the brain, we include glial cells in the larger set of cells that are of importance to investigate.

2.1.2 Basic anatomy

The brain is a biological system that does not adhere to a given rectilinear coordinate system. Rather, it is comprised of a set of several major regions that have developed for general tasks such as those necessary for survival (brain stem), muscle coordination (cerebellum) and higher level processing of sensory input (cortex) (see Fig.2.4).

We focus on the cortex, which can be split up further into areas that focus on certain aspects of higher level processing of sensory input, such as integration of sensory information (parietal lobe), visual processing (occipital lobe), auditory processing (temporal lobe), and executive function (frontal lobe). The cortex is comprised of the gray matter, the layer of neuron and glial cells on the folded surface of the cortex, and white matter, the area which is mainly processes (axons) travelling between different brain regions.

2.2 Spatial arrangement

2.2.1 Development

The mammalian brain develops in a particular way that is important to our study of spatial arrangement of cells and other processes. Just as for the rest of the body, the brain begins to grow and come into shape during the gestation period, or the time between the fertilization of the egg and birth. In the earliest stages of gestation, the brain is a sheet of similar cells that is on the outer surface of a disk-like embryo. During growth, these cells begin to differentiate, or irreversibly change into the cells that they will stay as during the life of

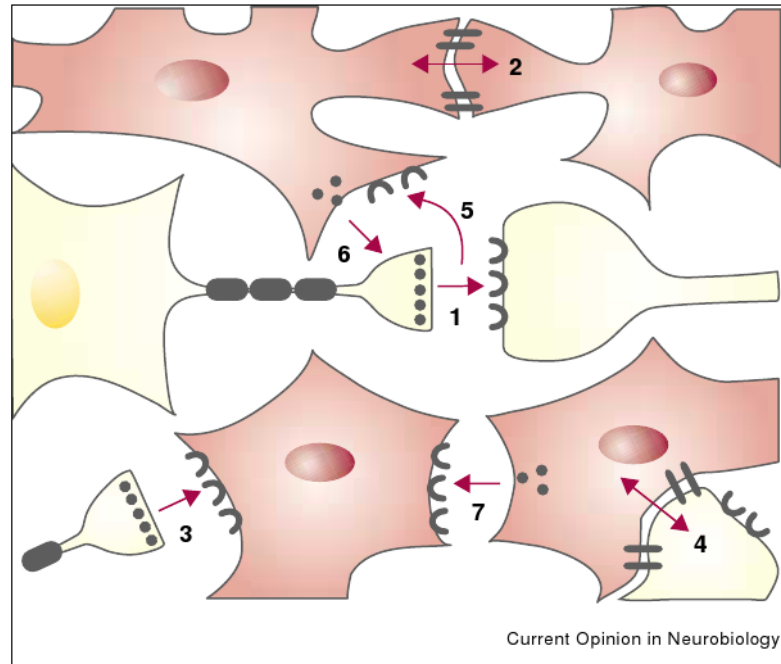


Figure 2.3: Examples of the interactions between neurons and glial. Glial cells in pink and neurons are in white. The traditional interactions known in the field are of traditional electrical connections of axons of one neuron cell with a dendrite of another neuron (1) and of glial-glial interactions. Recent studies have shown neuronal axon signals received by glial cells (3), direct coupling of glial cell bodies and neuron cell bodies (4), influence of neuron transmitter on nearby glial cell bodies (5) release of neurotransmitters from glial cells which affect the firing of neurons (6), and passing of neurotransmitter from one glial cell to another (7). This schematic shows a very different type of network in the brain than the traditional network comprised only of neurons. *Reproduced from Bezzi and Volterra (2001)*

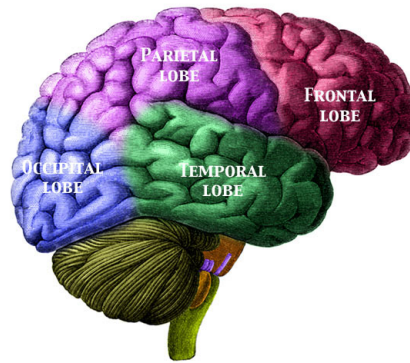


Figure 2.4: Shows three main areas of the brain: the cortex (top), the cerebellum (lower left), and brain stem (bottom). The cortex is split into its main functional areas: the frontal lobe, the parietal lobe, the occipital lobe, and the temporal lobe. *Reproduced from Gray (1918)*

the animal, such as neuron and glial cells. As the brain changes into the shape that it will eventually become, these cells travel and migrate to final destinations in the overall brain structure, and begin to connect with one another (see Fig. 2.5). Fig. 2.5 shows two times in the development of the human brain when the number of differentiated cells develop more rapidly (20 weeks into gestation for neurons and several months after birth for glial cells).

We highlight this development process to stress the dynamic nature of cell movement because the disruption of this process is one of the main mechanisms that can affect spatial arrangement of cells within the developed brain. Several diseases such as schizophrenia and epilepsy has been studied to be attributable to the improper migration of certain cell types during gestation (Anderson SA, 1996; Jones LB, 2002). With many conditions it is not clear what is to cause for the loss in function. For example studies have demonstrated that abnormal synaptic pruning in early development or childhood, and abnormal functional connectivity in adulthood may be causal factors in schizophrenia (Feinberg, 1982; Meyer-Lindenberg and Berman, 2001) et al., 2001; Andreasen et al. 1996). Brain metabolic abnormalities have been observed in bipolar disorder (Dager, 2004), while structural abnormalities have been found to be associated with schizophrenia but not bipolar disorder in

in our popular culture, this idea has not withstood scientific scrutiny as careful studies of both animals and humans have now demonstrated that there is no significant loss of cortical neurons in gray matter (Peters and Hyman, 1998). Instead, it seems likely that age-related atrophy of the forebrain is largely due to loss of cortical white matter (Peters and Rosene, 2003). These observations stand in stark contrast to the frank loss of neurons, gray matter, and white matter that occurs in neurodegenerative diseases like Alzheimers disease and has forced researchers to look elsewhere to understand the neuroanatomical basis of cognitive decline in normal aging. Even in neurodegenerative diseases such as Lewy-Body dementia, there is a loss in function that does not correlate with neuron loss (Buldyrev et al., 2000).

2.2.3 Mechanisms

Changes in spatial arrangement may reflect small displacements of the soma, but it is likely that these somal displacements merely reflect more widespread alterations in spatial relationships of elements in the surrounding neuropil. Candidates for this are changes in dendrites that have been demonstrated to undergo atrophy in a number of models of normal aging. It is possible that age-related changes in microcolumnar coherence occur in part from underlying changes in dendrite structure on a per-region and per-case basis.

In addition to neurons and dendrites, glial cells are also present in the neuropil and spatially associated with dendrites, axons, and neurons. Of the three different glial cells, the oligodendroglia are critical to maintain normal myelination; astrocytes are intimately invested around neuronal somata, dendrites, and synapses as well as nodes of Ranvier on myelinated fibers; and microglia respond to damage and produce inflammation. Moreover, astrocyte and microglial processes are known to be relatively motile but the spatial relationship of glia to microcolumnar structure is completely unknown. Hence, changes in any of these glial elements could affect neurons and their processes. It is therefore possible that that age-related changes in microcolumnar coherence or changes in dendrites are associated with changes in glial cell distribution.

2.2.4 Cortical Microcolumn

Since the 1980s, the application of unbiased stereological approaches to quantify objects of biological interest has allowed for rigorous measurements of many parameters of brain structure including total neuron number, area, and volume and have contributed greatly to the examination of the brain for age-related changes. These approaches are based on systematic random sampling from defined regions of interest using unbiased estimators (Mayhew, 1991; Schmitz et al., 2002). Although these measurements have produced extremely valuable insights into the structural organization of the brain, including age-related preservation of neuron numbers (Peters and Hyman, 1998), these “first order” stereological parameters only partially describe the structural organization of the brain, as they cannot efficiently quantify “second order” parameters that measure more complex spatial properties of neuron organization, such as the nearest neighbour arrangement (Asare, 1996; Duyckaerts and Godefroy, 2000; Schmitz et al., 2002; Urbanc et al., 2002; Hof et al., 2003; Krasnoperov and Stoyan, 2004) (see Sec. 2.2). Stereology also disallows the measurement of another important spatial feature of the cortex: the microcolumn.

In terms of age-related deficits in cognitive function and the possible underlying neurobiological substrates, the microcolumn is a distinct unit of vertically arranged neurons that is second only to horizontal lamination as a distinct feature of the spatial organization of cerebral cortex. Studies of the horizontal lamination have flourished for over a century and have consistently demonstrated that observable differences in horizontal lamination pattern that parcellate the cortex into different areas (e.g. Brodmanns or Vogts numbered or lettered areas) have consistently turned out to reflect real functional differences. But in contrast to the horizontal lamination that was studied at a scale of centimeters or millimeters and can be related to macroscopic variables such as damage due to stroke or experimental lesion, the vertical organization exists on a microscopic scale with vertical arrays spacing ranging from 20 to 100 microns for the microcolumn and multiple microcolumns making up macrocolumns that dont exceed 1 mm (EG, 2000). In fact, despite the visual identification of this vertical organization the potential functional significance of the microcolumn was

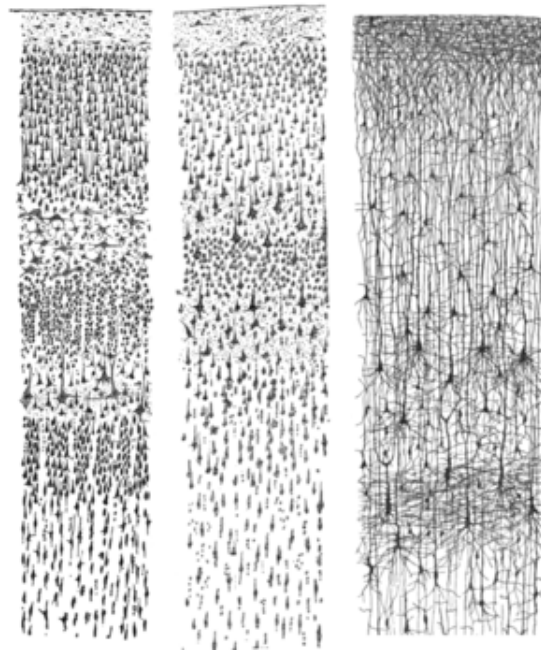


Figure 2.6: Three drawings by Santiago Ramon y Cajal showing the microcolumnar structure of a sample of gray matter of the cortex from the pia surface (outer surface of the brain)(top) to the white matter (bottom). Left: Nissl-stained visual cortex of a human adult. Middle: Nissl-stained motor cortex of a human adult. Right: Golgi-stained cortex of a 1 1/2 month old infant. To note are the tendency of the cells to line up with one another
Reproduced from y Cajal (1899)

only appreciated after the Neurophysiological studies in somatosensory cortex (Mountcastle, 1957, 1997, 2003) and in visual cortex (Hubel DH, 1963, 1977) demonstrated that each microcolumn had unique receptive field properties. Since then the microcolumn has received occasional attention at a fundamental level (Swindale, 1990; D. Purves and LaMantia, 1992; Saleem et al., 1993; Tommerdahl et al., 1993; Peters and Sethares, 1991; Vercelli et al., 2004) and more recently in the context of cortical pathologies (Buxhoeveden and Lefkowitz, 1996; Buxhoeveden and Casanova, 2002; Casanova et al., 2002). Our interest in the microcolumn stems from a growing body of studies that relate the anatomy of the microcolumn to loss of function, and which implicate structural changes in microcolumns in cognitive changes seen in normal aging and disease states. For example, differences in neuron distribution in general and within microcolumns are observed in normal aging (Cruz et al., 2004; Chance SA and MM, 2006) and in Alzheimers Disease (VanHoesen and Solodkin, 1993; Buldyrev et al., 2000). Alterations in microcolumnarity have also been reported in schizophrenia (Benes and Bird, 1987; Buxhoeveden et al., 2000), Downs syndrome (Buxhoeveden and Casanova, 2002), autism (Casanova, 2003), dyslexia (Buxhoeveden and Casanova, 2002), and even secondary to drug (cocaine) manipulation during development (Buxhoeveden et al., 2006). Interestingly, in normal aging monkeys where, as we have noted, cortical neurons are largely preserved in a number of areas including primary visual cortex (Peters and Hyman, 1998), evidence of age-related physiological disruption of orientation selective microcolumns has been reported (Schmolesky et al., 2000; Leventhal et al., 2003). These studies all confirm that regional differences in the mini or microcolumn, like cytoarchiteconic parcellations, likely reflects specific functional specializations such that the microcolumn may be a fundamental computational unit of the cortex. It also suggests that alterations in microcolumn structural organization may reflect alterations in its function and hence of the specific functions of any affected regions. The problem is that the enumerations methods of modern stereology do not yield information about the spatial relationships among the enumerated objects, even if they are mainly in microcolumns. In addition, because of the inherent variation of vertical organization due to the intrinsic curvature of the cortex, the systematic

random sampling methods of modern stereology (perhaps the most important contribution of stereology to brain science) also makes it impossible to use this data to study spatial organization on the scale of tens of microns.

To quantitatively assess microcolumnar structure and possible changes, we have adapted methods derived from statistical physics to analyze local spatial relationships among neurons as they are organized into microcolumns (Buldyrev et al., 2000; Cruz et al., 2005; A. Inglis and Rosene, 2008) and application of these methods to study the effects of normal aging forms the basis of this application. We will now discuss this method.

2.3 Measurement Theory

In this section I will describe the main analysis techniques that we perform with the data that we pull from the tissue. Although this is the third of the three steps in the experimental setup, I discuss it first due to its importance in motivation. Also, knowledge of the analysis techniques will allow us to understand the process of obtaining the data via the first two steps.

2.3.1 Raw Data

The raw data that is used in measurements of the tissue are that of the cell bodies inside of the tissue.

The raw information extracted from the image (as described in Sec. ??) can be represented by a density of a certain nominal cell type i where i can be neurons or glial cells) in a phase space of ordinal cell properties, such as x,y,z location, size, shape (Fig 2.10)

As an example to such a space, we can imagine the field of neurons in Fig. 2.9 represented in a phase space shown in Fig. 2.10, the i th the nominal index comprised of neurons and glial cells, and the ordinal phase space having the dimensions $x,y,size, and$ cell orientation.

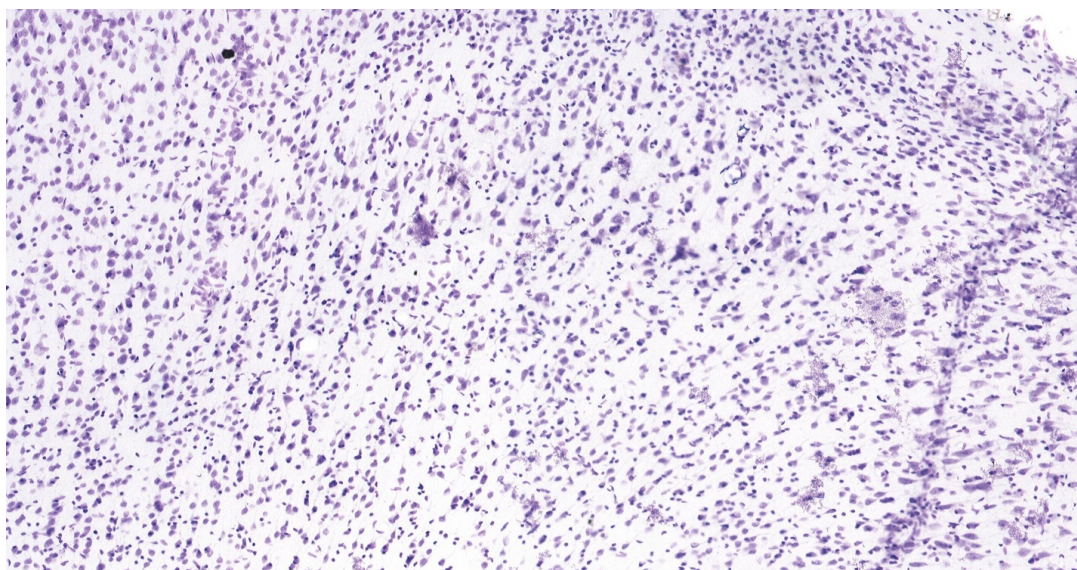


Figure 2.7: Example of tissue sample from the rat brain.

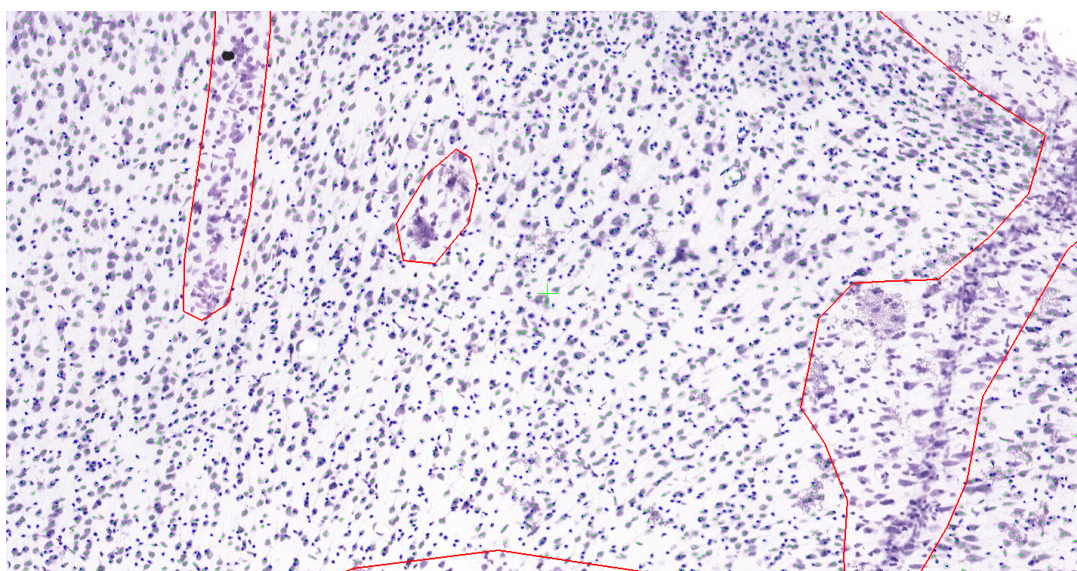


Figure 2.8: Example of tissue sample from the rat brain with borders and neurons and glial found (See Sec. 3 for steps to obtain points).

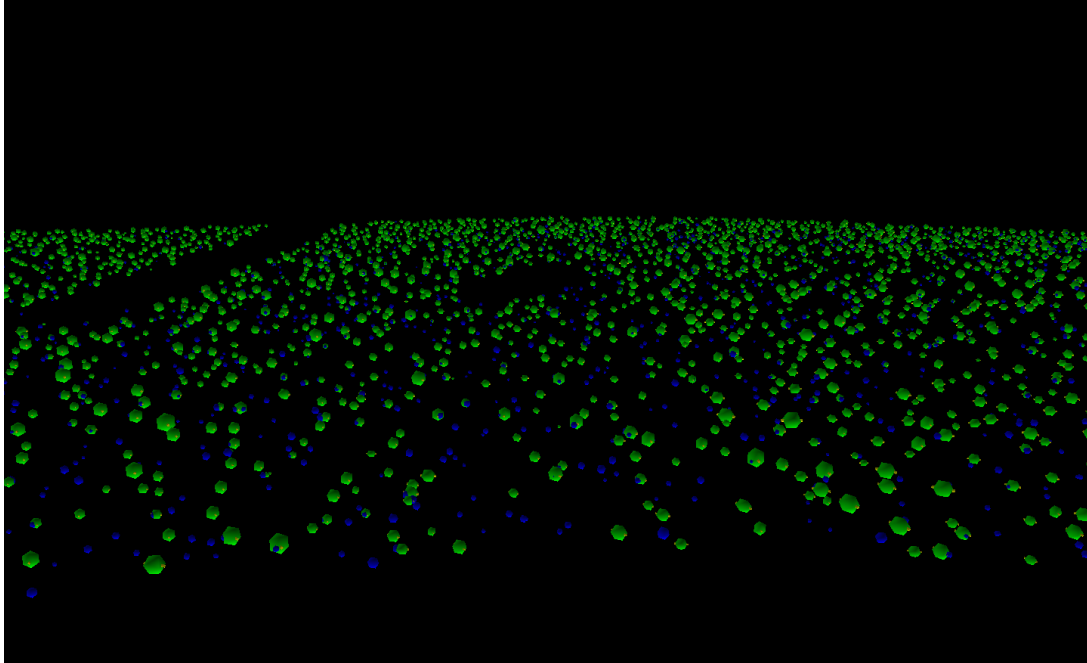


Figure 2.9: Properties such as x,y location, observed size, and angular orientation can be determined and extracted to a dataset independent of the original images .

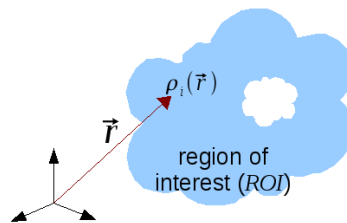


Figure 2.10: for a given region of interest, the cell information can be represented by a density of a certain nominal cell type i in a phase space of ordinal cell properties, such as x,y,z location, size, shape.

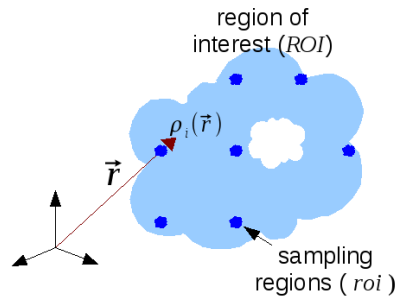


Figure 2.11: Using Stereology, a detailed measurement can be made on a smaller region of interest called a sampling region (*roi*), then that information is used to determine what the measurement would be on the entire region.

2.3.2 Stereology

The traditional method of condensing this large amount of data into a measurement of the ROI is to integrate the density over the space to obtain a measurement M :

$$M = \int_{ROI} \rho_i(\vec{r}) d\vec{r} \quad (2.1)$$

If this was the final equation that is used to obtain a measurement, then the process would quickly become prohibitively time consuming. Recall from Illustration 1at there are no methods that can obtain the resolution and breadth measurement of these densities other than neuroanatomy, which involves the laborious task of slicing the brain tissue, staining the tissue, mounting the tissue onto glass slides, and manually observing the cells underneath a microscope. For large areas of millions of neurons, the direct calculation would quickly become impossible. The solution is a method called Stereology, which is the equations and methods used to take unbiased samples of the ROI and used them to closely determine any total measurement of the tissue M (see Fig. 2.11).

Using the sampling concept of stereology, the equation to determine the measurement M is:

$$M = \int_{roi} \rho_i(\vec{r}) d\vec{r} \cdot \left[\frac{\int_{ROI} d\vec{r}}{\int_{roi} d\vec{r}} \right] \quad (2.2)$$

The large amount of work of determining the density in the whole region is now reduced to a sample of the region, and an additional measurement of the ratio of volume of the region of interest (ROI) and the sampling region (roi) must be recorded (this is never more work since the ROI must be delineated in any case). The application of design-based stereology to obtain estimates of total cell number has led to valuable insights into structural features of the brain. Although there are many benefits, stereology has some limitations for studies that involve comparatively large regions of interest (ROIs) and large number of subjects. The time and effort required to perform stereology limits the number of areas and questions that can be studied. Also, the speleologist performing the study must be vigilant against shifting cell selection criteria throughout the experiment (an issue known as experimental drift). Most importantly, stereology assumes that the distribution of the objects being assessed in the ROI is homogeneous, yet recent findings show that the heterogeneity of spatial patterns among cells is also important to understanding cortical organization and potential alterations in aging or other conditions.

2.3.3 Correlation measurements

Types of measurement

As discussed in Section 2.2, these shortcomings of stereology are compounded with the most critical concerning our investigations of the brain: although these measurements have produced extremely valuable insights into the structural organization of the brain, including age-related preservation of neuron numbers (Peters and Hyman, 1998), these “first order” stereological parameters only partially describe the structural organization of the brain, as they cannot efficiently quantify “second order” parameters that measure more complex spatial properties of neuron organization, such as the nearest neighbour arrangement (Asare, 1996; Duyckaerts and Godefroy, 2000; Schmitz et al., 2002; Urbanc et al., 2002; Hof et al., 2003; Krasnoperov and Stoyan, 2004) and arrangement into mini- or microcolumns (Buxhoeveden and Lefkowitz, 1996; Buldyrev et al., 2000; Cruz et al., 2005). Several approaches can be used to quantify “second order” parameters. Stereological methods can quantify

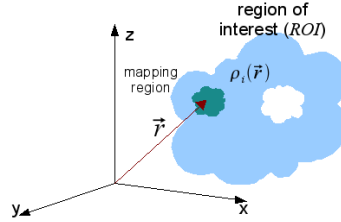


Figure 2.12: The sampling region for more detailed heterogenous and correlation data exists as a small mapping region centered around an arbitrary location in the ROI.

nearest-neighbor arrangement (Schmitz et al., 2002), but the methods are labor intensive and would be difficult to apply to large brain areas. Image Fourier methods do not require manual marking of neuron locations and can quantify “vertical bias” of objects within an image (Casanova et al., 2006), but do not discern between the contribution from glial and neuronal cell bodies. Alternatively, pair correlation methods use concepts from statistical physics to calculate correlation properties such as cross-correlation between two different types of objects (Urbanc et al., 2002) and microcolumnar organization (Buldyrev et al., 2000) of neurons, as well as more discerning.

In terms of the representation of the *ROI* shown in Figs. 2.10 and 2.11, we want to know the cell densities $\rho_i(\vec{r})$ for every location \vec{r} within the *ROI* (See Fig. 2.12).

From this knowledge of the tissue, we can create positional dependent measurements of *ROI*:

$$M(\vec{r}) = \int_{roi} \rho_i(\vec{r}) d\vec{r} \quad (2.3)$$

with allows us to probe the heterogeneity of the tissue. In addition, we can create correlation measurements describing local cell organization. We do this by focusing on an arbitrary sampling region. When focusing, we can perform two transformations. First, we can form a phase space that is a projection (out of desire or necessity) of the full property phase space. For example, if we do not have z information of location, or size information, these dimensions can be integrated over, reducing the dimensions that will be analyzed

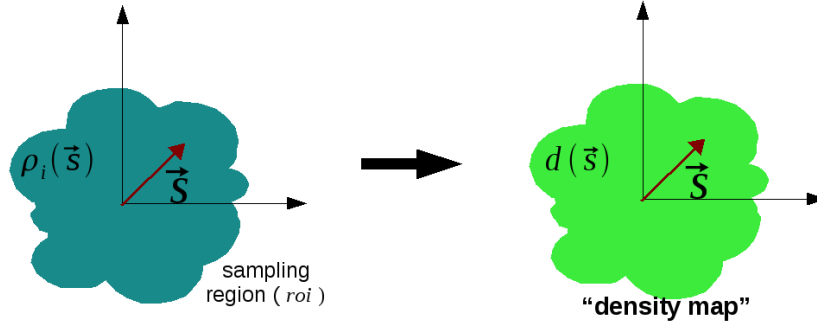


Figure 2.13: Graphic depicting the transformation from the projected and rotated density space to the density map space.

further. Second, the coordinate system remaining after the projection can be rotated in some way to align with other sampling regions that will be summed for better statistics. After these transformations of the space, a density map can be created with the following equation:

$$d(\vec{s}) = \int_{roi} \rho_i(\vec{s}') \rho_j(\vec{s}' - \vec{s}) d\vec{s}' \quad (2.4)$$

where \vec{s} denotes the new projected and rotated space at each sampling region (See Fig. 2.13).

An example of such a correlation measurement is the x,y correlation of neuron location to investigate the columnar structure of tissue (See Sec. 2.2.4). If we take samples regions (roi) of x,y neuron location from a given region of the brain as shown in Fig. 2.9 then we have a density of $\rho_i(\vec{r})$ where i represents the neuron population and $\vec{r} = \{x, y\}$. We have already condensed the space to two dimensions, and rotated each mapping region so that the x direction is perpendicular to the general microcolumnar structure. The equation for the density map is then:

$$d(x, y) = \int_{roi} \rho_{neuron}(x', y') \rho_{neuron}(x' - x, y' - y) dx' dy' \quad (2.5)$$

The more common radial correlation can be employed by integrating over the surface of radial surface of the density map (see Fig. 2.14).

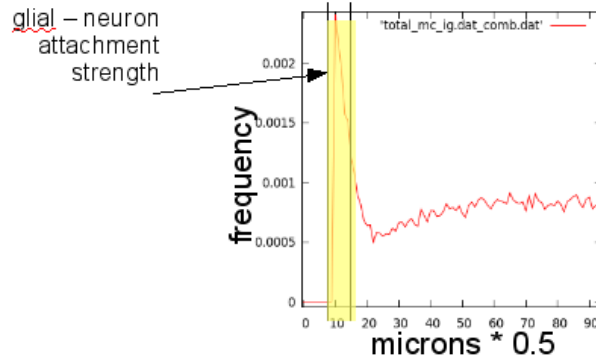


Figure 2.14: The plot is created by first creating a cross correlation between neurons and glial cells, then integrating over the surface of radial surface of the density map.

$$d(r) = \oint_{surface} d(x, y) d\vec{r} \quad (2.6)$$

where $d(x, y)$ is defined in Eq. 2.5. Using this correlation technique, we examined the structural integrity of this new architectural feature in two common dementia illnesses, Alzheimer disease and dementia with Lewy bodies. In Alzheimer disease, there is a dramatic, nearly complete loss of microcolumnar ensemble organization. The relative degree of loss of microcolumnar ensembles is directly proportional to the number of neurofibrillary tangles, but not related to the amount of amyloid-B deposition. In dementia with Lewy bodies, a similar disruption of microcolumnar ensemble architecture occurs despite minimal neuronal loss. These observations show that quantitative analysis of complex cortical architecture can be applied to analyze the anatomical basis of brain disorders (see Fig. 2.15).

From such density maps, we want to measure a quantitative property that defines the particular strength of a given correlative structure. To do this, we quantitatively measure features inside of the density map. For a given density map as shown in Fig. ref{mcolMeasures can measure properties such as the column strength, periodicity of the microcolumn, width, and length. With respect to strength, these measurements are determined by the relative density of the density map inside verses outside of certain areas. With respect to width, an summation of rows of the density map can be made, then the width of the main peak outside

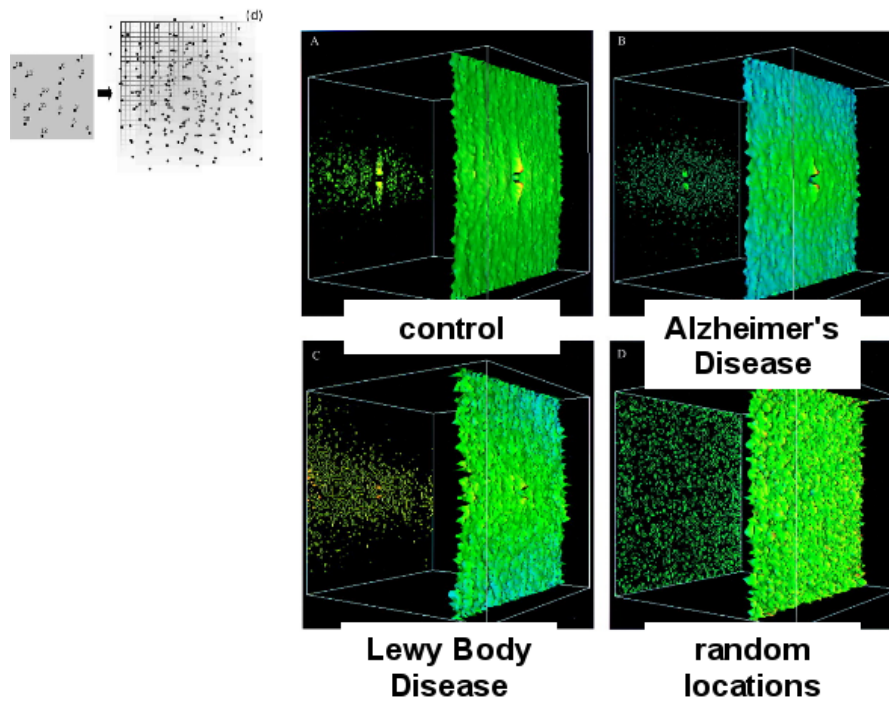


Figure 2.15: The creation of the density map from the double summation of rotated and aligned, x,y neuron locations in sample regions (left). (right) shows resultant density maps for tissue samples of several different dementia diseases. *Reproduced from Buldyrev et al. (2000).*

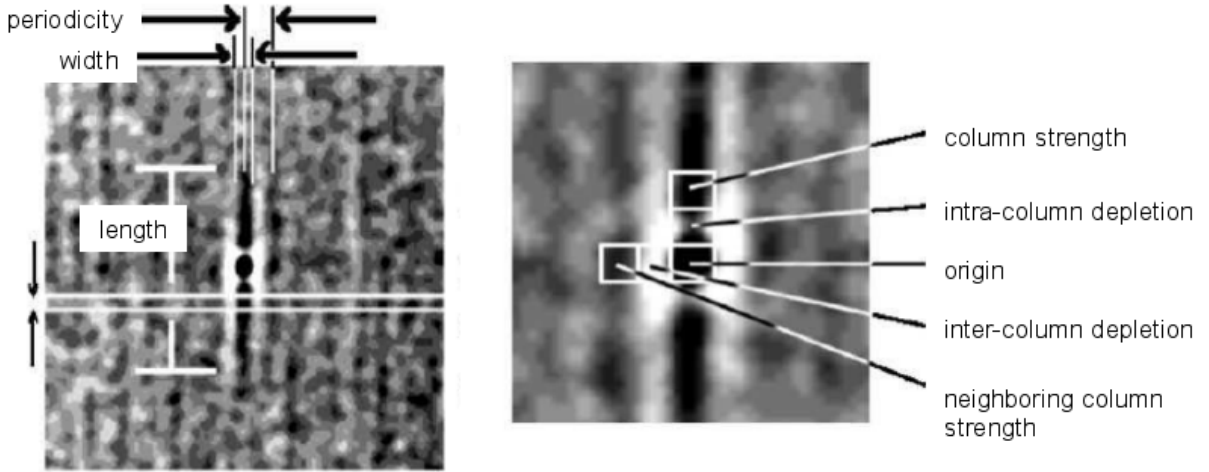


Figure 2.16: Specific measurements that can be pulled from the 2-D x,y density map as described in Eq. 2.5. *Reproduced from Cruz et al. (2005).*

of the noise of the image is measured. With respect to periodicity, a similar summation of rows is performed, then a peak to peak measurement is made.

Quantitative measurements are extracted from the density map shown in Fig. 2.16, like the distance between columns, length and width of columns, and “strengths” of columnar properties, which are the relative tendency for cells to be in spatial arrangement locations with respect to one another. The strengths are calculated by measuring the relative difference in density of a particular small region of interest (represented as *roi* in lowercase) compared to the density average of the entire density map region of interest (*ROI*):

$$M = \frac{\int_{roi} d(\vec{s}') d\vec{s}'}{\int_{ROI} d(\vec{s}') d\vec{s}'} \quad (2.7)$$

(the quantities S_{num} and T_{num} mean that they have not been normalized by the overall average density. In certain cases as will be discussed it is better to know the actual density inside the column rather than the ratio)

Motivated by the heterogeneous nature of spatial arrangement properties, we develop a method of exploring changing properties as one probes in a linear dimension through the cortex. Because of the photomontaging ability (see Sec.??, we are able to measure

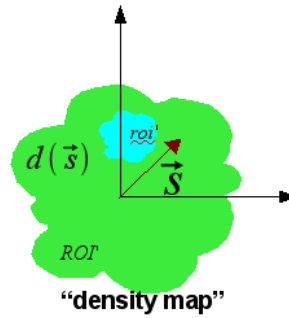


Figure 2.17: the *roi* that is measured are shown in Fig. 2.16 as column strength (known as measurement S), intra-column depletion, origin, inter-column depletions, and neighboring column strength (known as measurement T).

changes of spatial arrangement features seamlessly across tens of thousands of microns. Measurements from this analysis can take one of three forms. First, the measurement can act as a probe, so that for a given area of the brain, multiple overlapping samples are taken, and a cumulative density map is formed based on all sampling regions of a known location. Or, local measurements of the correlations can be made by taking a local set of sampling regions and creating a density map for each one (See Fig. 2.18). The benefit of this type of analysis is that regions don't need to be defined before the analysis occurs as they need to be in the probe method. Lastly, because of the intrinsic curvature of the cortex, we create tracks using the visualization system that serve as a guide to our running window analysis. Once the tracks have been defined, a "running window", or section of the track, is selected, and the x,y locations acquired with ANRA within the running window are used for spatial measurements. The analysis window is lengthened or shortened depending on the number of data points (neurons) that are needed for a statistically significant measurement. Therefore, properties are recorded through a direction parallel to the pia surface in the gray matter (See Fig. ??). This type of measurement straddles the two previously mentioned, by grabbing a maximum amount of statistics spanning a given layer, but seeing changes of the cortex as the probe moves through the tissue. Preliminary results using this type of method show that in similar regions of the brain, there are fundamentally different structures of

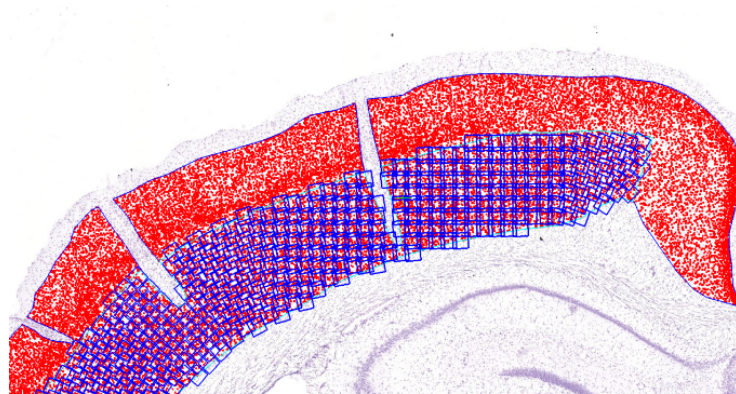


Figure 2.18: Example of a grid of sampling regions within the infragranular layers (5,6) of the rat. Notice that the sampling regions have been rotated according to the general coordinate system of the gray matter: perpendicular to the pia and white matter surface.

microcolumnar structure in different subjects in the same regions of the brain. Lastly, from this additional data, we can create other density maps, projected and oriented if needed:

In addition to these correlation methods, which use the locational spatial properties, we also investigate correlations using the measured size and shape properties which can give axon/dendrite process directions and neuron/cell type information (see Fig. 2.21).

Measurement error

Because of the biological noise as well as recognition noise (from the automatic recognition measurements; see Sec. 3.3), there is a need to determine what amount of variation from the real values (values obtained if unlimited data of similar spatial arrangement was available) called *biological variance* occurs depending on how many particles are incorporated in a given measurement. This variation determines the resolution we can see changes in neuron spatial organization across the cortex. We investigate this relationship between noise, sample size and resolution for all of the measures implemented in the study. We investigate these properties explicitly by introducing known distributions of noise into the analysis calculations. We also empirically determine variance levels by modeling biological and recognition variance into a model of neuron organization.

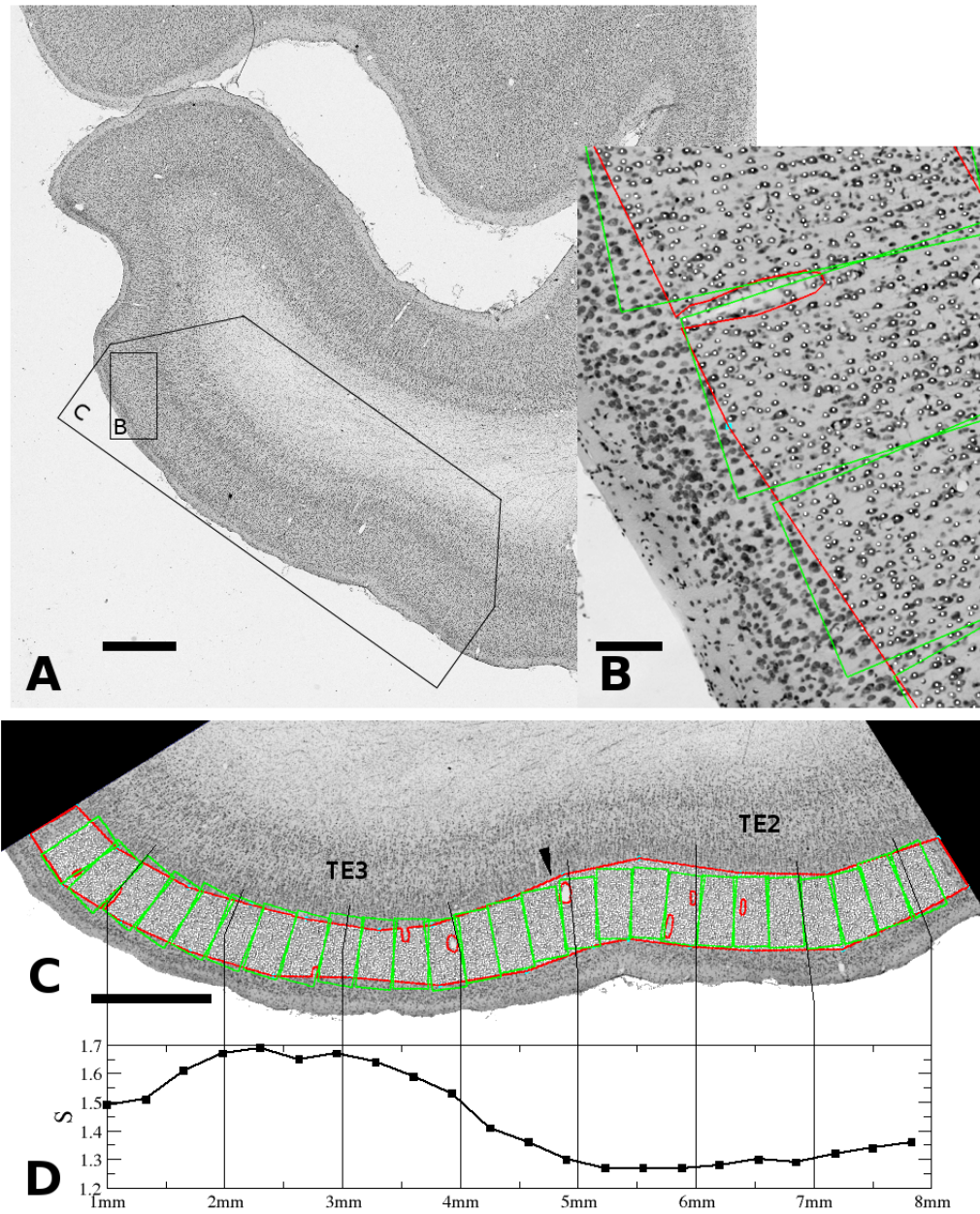


Figure 2.19: Example of a grid of sampling regions within the infragranular layers (5,6) of the rat. Notice that the sampling regions have been rotated according to the general coordinate system of the gray matter: perpendicular to the pia and white matter surface.

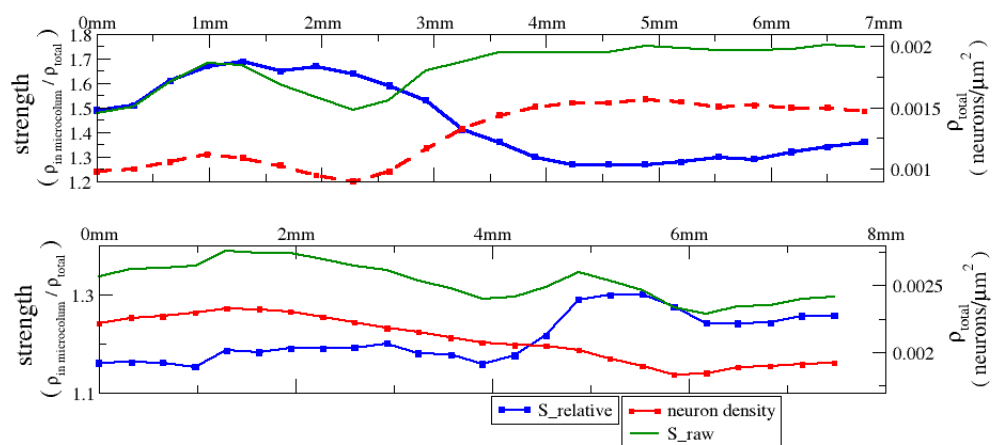


Figure 2.20: Comparison of running window analysis between two macaque monkey subjects in the temporal lobe.

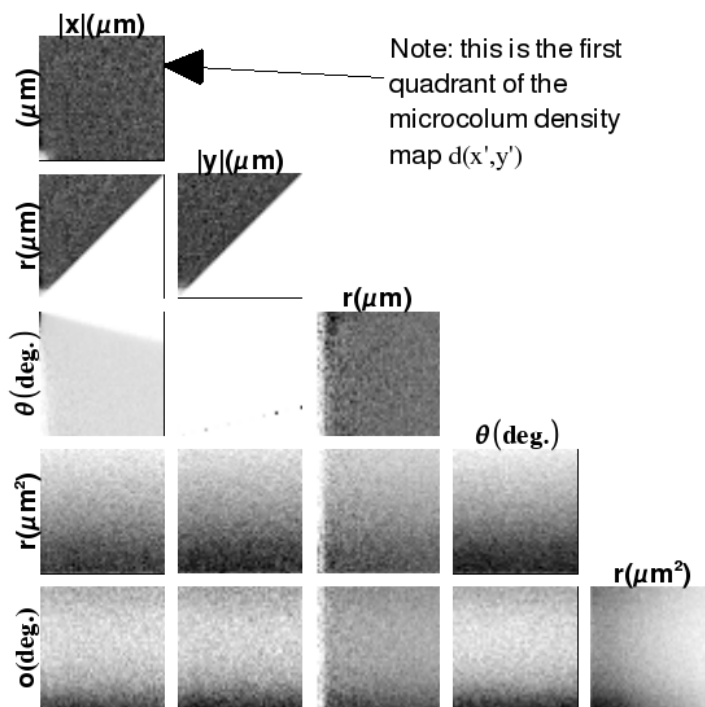


Figure 2.21: Density maps showing additional correlations of cell properties.

It is possible to estimate the upper limit of error that is obtained with such a measurement by assuming that the cell information is randomly distributed throughout the tissue. Here we follow the logic of Buldyrev et al. (2000), but adapt the question from one of being able to see a statistically significant feature on a pixel by pixel basis (in order to visualize spatial arrangement properties as in Fig. 2.15) to one of seeing statistical significance in a measurement over a given *ROI*. For such a random sample, the average number of cells $\langle n_i \rangle$ from one cells correlation in the measurement area (such as the column strength area in Fig.2.16) is represented by ρa , where ρ is the average density of cells and a is the area of the measurement window. The standard deviation of the cell count in a Poisson distribution is given as $\sqrt{\langle n_i \rangle}$. The standard deviation of the density in area ρa is then

$$\sigma_\rho = \frac{\sqrt{\rho a}}{a} = \sqrt{\frac{\rho}{a}} \quad (2.8)$$

The final density map is an integral, or summation in discrete terms, of the total number of cells N in the *ROI*, therefore the standard deviation of the density maps is $\sigma_\rho \div \sqrt{N}$. Finally, the error of the measurement of the density map is then

$$e = \frac{1}{\sqrt{\rho a N}}. \quad (2.9)$$

We then solve for the number of cell locations needed for a given area measurement, average density of cells, and error tolerance:

$$N = \frac{1}{\rho e^2 a}. \quad (2.10)$$

A similar logic can be performed for the radial correlation (see Fig. 2.14). Because there is a multiplicity of correlations further away from the origin, there is a dependence on the distance r from the origin that the measurement is taken, and the area of measurement is now the length l :

$$N = \frac{1}{2\pi r \rho e^2 l}. \quad (2.11)$$

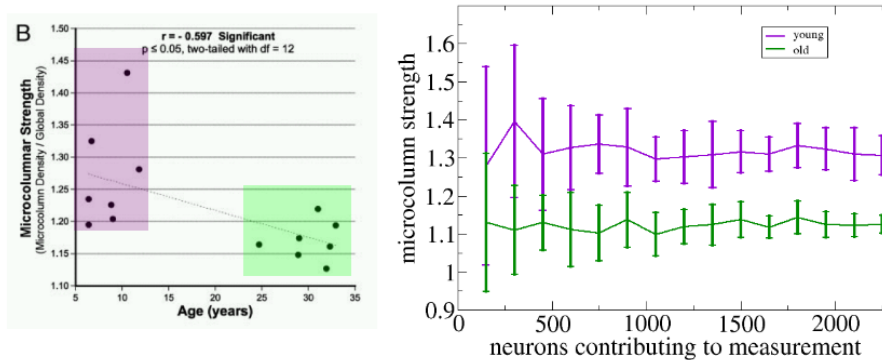


Figure 2.22: (left) Shows a result of microcolumnar strength changes in young vs old monkeys (Cruz et al., 2004). (right) 10 random selections of images from each cohort (old, green, lower measure, and young, re, higher measure), number of images correspond to total neurons within the images selected. For two measurements of roughly 10% difference (1.3 vs 1.15), the number of neurons needed is around 500 to reach a result of significance between the two groups.

These equations show that many cell locations are needed in order to create low error measurements of spatial properties of cells. For example, for a standard density of 0.002 cells per μm , and a measurement area of $100 \mu m^2$ - the diameter of a standard cell body ($10 \mu m$), the number of cells to reach an error of 10%/5%/1% is 500/2000/50000 cells. For the radial correlation of a measurement of two cell diameters ($20 \mu m$), the numbers needed for the same errors are 60/230/5700 cells.

As an experimental verification of this estimate, we used data from an earlier study showing microcolumnar strength changes in young vs old monkeys (Cruz et al., 2004). Taking the total number of tissue images and subsequent neuron locations for the young and old as two separate datasets (a total of 10,000 neuron locations in each set), we randomly pulled subsequently larger number of images (and hence neuron locations) to incorporate in the measurement of S (see Fig. 2.17). What we find is for two measurements of roughly 10% difference (1.3 vs 1.15), the number of neurons needed is around 500 to reach a result of significance between the two groups. This is the point where the measurement “statistical noise” is becoming less than the “biological noise” of the tissue.

In this chapter we have reviewed the many ways that cells in the brain can be influenced and subsequently change their spatial arrangement with respect to one another, and we have reviewed how these changes can be linked to many other more hidden changes of how the network of the neurons and glial cells is changing. We introduced tools that can be used to measure heterogeneity of average properties of individual cells within the brain, and can also quantitatively measure the spatial relationships between cells of the same and different populations. We tested the statistical robustness of these measurements of real data, and found that we can tune the statistical noise of the measurement to the desired level to be able to see subtle changes in patterns right above biological noise that are not visible by the naked eye. We also noted that the number of cells needed for these measurements is large, and must be performed locally wherever the measurement is performed.

With this motivation, we move to the next Chapter, which discusses the experimental technique needed to obtain the large datasets needed for the true power of correlative analysis to be applied to the cortex.

Chapter 3

Experimental Method

The purpose of this section is to describe the automated methods developed to quickly and efficiently acquire individual cell information.

3.1 Introduction

Since the 1980s, the application of unbiased stereological approaches to quantify objects of biological interest has allowed for rigorous measurements of many parameters of brain structure including total neuron number, area, and volume. These approaches are based on systematic random sampling from defined regions of interest using unbiased estimators (Mayhew, 1991; Schmitz and Hof, 2005). While these measurements have produced extremely valuable insights into the structural organization of the brain, including age-related preservation of neuron numbers (Peters and Hyman, 1998), these “first order” stereological parameters only partially describe the structural organization of the brain, as they cannot efficiently quantify “second order” parameters that measure more complex spatial properties of neuron organization, such as the nearest neighbor arrangement (Asare, 1996; Schmitz et al., 2002; Duyckaerts and Godefroy, 2000; Krasnoperov and Stoyan, 2004; Hof et al., 2003; Urbanc et al., 2002) and arrangement into mini- or microcolumns (Cruz et al., 2005; Buldyrev et al., 2000; Buxhoeveden and Lefkowitz, 1996).

Several approaches can be used to quantify “second order” parameters. Stereological

methods can quantify nearest-neighbor arrangement (Schmitz et al., 2002), but the methods are labor intensive and would be difficult to apply to large brain areas. Image Fourier methods do not require manual marking of neuron locations and can quantify “vertical bias” of objects within an image (Casanova et al., 2006), but do not discern between the contribution from glial and neuronal cell bodies.

Alternatively, pair correlation methods use concepts from statistical physics to calculate correlation properties such as 1D nearest-neighbor (Urbanc et al., 2002) and 2D microcolumnar organization (Buldyrev et al., 2000) of neurons, as well as more discerning properties of spatial arrangement, such as the strength of microcolumnar order and microcolumnar width and length (Cruz et al., 2005). The multitude of spatial organization quantities that can be calculated with pair correlation analysis makes it appealing to apply to large brain areas. To do that, we first need to address the major challenge to this approach: how to obtain the necessarily large number of neuron locations ($10^3 - 10^4$ locations per measurement) to get statistically significant results (see Sec. 3.2.7 and Discussion) over large regions of the brain, reaching $\sim 10^6$ for a large study. The acquisition of such numbers of neurons by manually or semi-automatically identifying and marking the location of each is prohibitively time-consuming and open to user bias. Hence, correlative analysis of spatial relationships among neurons (as well as non-stereology based cell counts (Todtenkopf et al., 2005)) would be dramatically facilitated by an automatic method for identifying and locating the visible centers of neurons accurately and efficiently.

While various other immunohistochemical methods could facilitate automated discrimination of neurons and glia better than Nissl, there are important advantages to develop automated methods for Nissl-stained tissue. Nissl-staining is the least expensive, easiest applied method for staining both neurons and glia. Furthermore, there are thousands of unique and often irreproducible collections of Nissl-stained brain material in clinical and research labs around the world that could be analyzed using the ANRA.

There are several challenges to automatically retrieve neuron locations from two-dimensional digitized images of Nissl-stained brain tissue (Fig. 3.1a). A major challenge is to distinguish

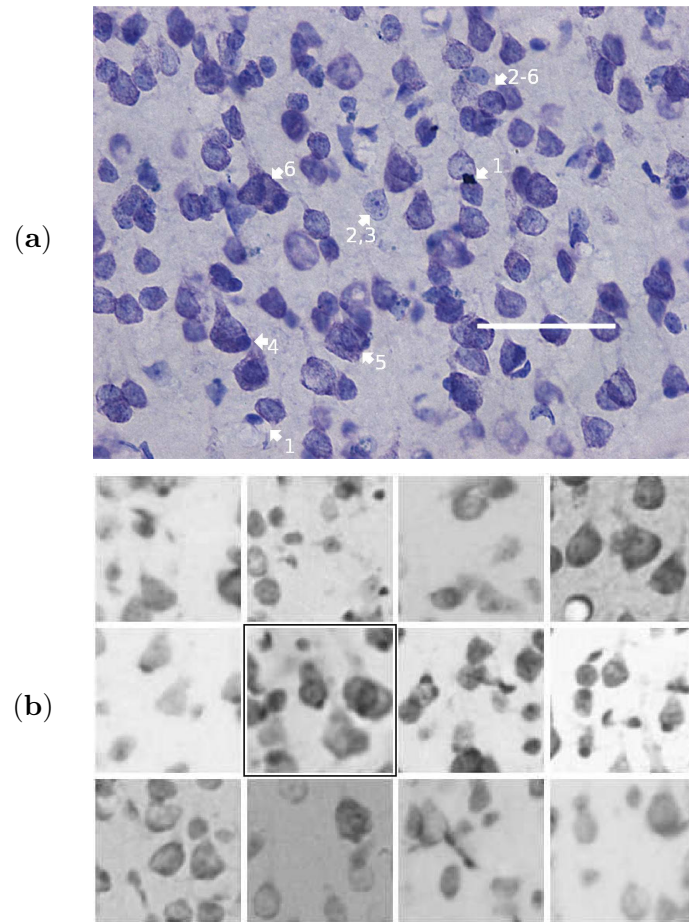


Figure 3.1: (a) 20x micrograph (scale bar: $50\mu m$) of a typical section showing the difficulties of separating neurons from glial cells and other artifacts in Nissl-stained tissue: 1. capillaries, and unidentified material, 2. large glia (astrocytes), 3. glial as light as neurons in some cases, 4. neurons overlapped by glia (oligodendrocytes), 5. neurons overlapped by other neurons, 6. multiple neurons and glial overlapped. (b) 10x micrograph examples showing varying image quality. The highlighted micrograph is selected as an “ideal” contrast to be used in image normalization.

between neuron and non-neuron objects, including staining errors, tissue folds, and dirt particles, as well as blood vessels and glial cells. Another challenge is to identify neurons that differ almost as widely from each other as they do from non-neuronal objects. Neuron cell bodies are naturally diverse in size and shape and have different orientations with respect to their dendrite and axon processes. Neurons can also be cleaved at the cutting surface or damaged by the cutting process, which affects their shape in the tissue. These variables lead to diverse neuron cell profiles within the tissue slice. A further challenge is to discriminate between neurons that overlap, a common finding as tissue sections are 3D volumes projected onto a 2D image.

There are currently several published approaches to automatic retrieval of cell bodies from images. Some methods use segmentation techniques based on thresholding (Slater et al., 1996; Benali et al., 2003), Potts model (Peng et al., 2003), watershed (Lin et al., 2005), and active contours (Ray et al., 2002). Others use trained neural networks to mark appropriately sized “pixel patches” as cells of interest. The “pixel patch” training methods use artificial neural networks (Sjöström et al., 1999), local linear mapping (Nattkemper et al., 2001), Fischer’s linear discriminant (Long et al., 2005), and support vector machines (Long et al., 2006). Another method based on template matching has been recently introduced by Costa and Bollt (2006).

In this paper we introduce and test an Automatic Neuron Recognition Algorithm (ANRA) (Fig. 3.2) which uses a combination of segmenting and training to overcome the challenges of retrieving neuron location in Nissl-stained tissue sections. ANRA automatically identifies neurons from digital images and retrieves their (x,y) locations.

3.2 Methods

3.2.1 Image Input and Preprocessing

The inputs for ANRA are photomicrographs of 30 micron thick Nissl-stained tissue section taken at 10x magnification and a resolution of 1.5 microns per pixel. Because the 30 micron

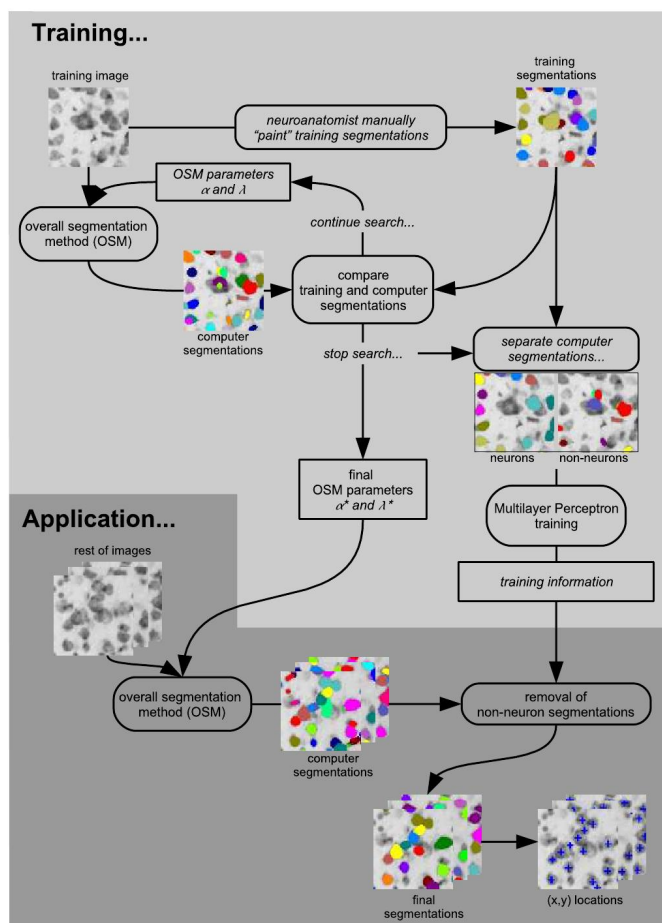


Figure 3.2: A schematic diagram showing processes involved in the Automated Neuron Recognition Algorithm (ANRA). The schematic describes the two main steps of the algorithm: training and application. Rectangles denote parameters that pass through the algorithm. Ovals, such as the OSM, are the computational parts of the algorithm, which can have images, segmentations, and parameters as their inputs and outputs.

tissue section shrinks during processing to a thickness of less than 10 microns, all of the tissue is in focus when viewed at microscopic magnifications of 20X or lower, thus the 2D image properly represents neuron locations . Since the color information is not as useful in the monotone Nissl-stained images (Fig. 3.1a) the images are converted to gray scale images ranging from 0 (black) to 255 (white).

The photomicrographs are taken from different areas of the brain from different subjects at different times. Therefore, images are of different “quality”, reflecting a combination of variations in morphology, staining, slide preparation, and digitization (Fig. 3.1b). To reduce this variability, the images are first “normalized” such that every image has the same background and foreground average optical density. This is done by thresholding each image into foreground and background pixels and finding the average optical density for the foreground and background separately. For each image, the optical density histogram is then shifted to match the foreground/background averages of an ideal image (Fig. 3.3a). Fig. 3.3b shows the images final normalization as compared to the original images in Fig. 3.1b. This preprocessing step removes most of the image variations due to processing (staining, slide preparation, digitization, etc.) and is a key step toward applying ANRA to an unlimited number of images that do not vary drastically in intrinsic morphological differences (neuron density, shape, size, etc.). There is no need for other preprocessing steps such as blurring or sharpening since ANRA, by design, overcomes the challenges of noisy images and weak boundary information.

3.2.2 Main segmentation tool: OSM

Here we describe the segmentation procedure presented in Fig. 3.2, called the overall segmentation method (OSM).

Over-marking the image

An initial step of the segmentation process is “seeding” the image with one or more points for each possible neuron cell body. A combination of two methods is used (Fig. 3.4a): a

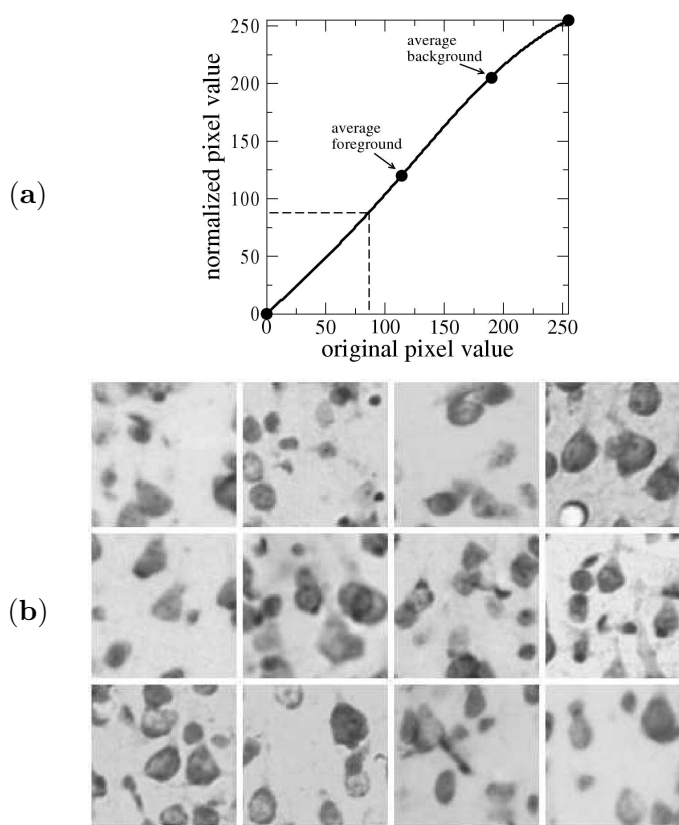


Figure 3.3: (a) Preprocessing “normalizes” the images so that every image has the same background and foreground average optical densities, thereby removing the challenge of varying image type within Nissl-stained tissue. This is done by mapping optical density values of non-ideal images to an ideal image so that the average foreground and background averages are the same. The graph shows the optical density ranges of the ideal and non-ideal images (0..255), and a Bezier curve that passes through 4 points: (0,0), the background and foreground averages of the ideal and non-ideal images, and (255,255). (b) Examples of image normalization.

hexagonal grid of points is placed over the thresholded foreground of the image and the center points of objects identified by the traditional watershed segmentation (Javi, 2002).

Active contour segmentation

We employ active contour segmentation with statistical shape knowledge (Cremers et al., 2000) because the method is designed to overcome the challenges of noisy images and missing boundary data, the main identification challenge in Nissl-stained tissue. Also, the method uses low-dimensional shape representations which are ideal for modeling cell contours (outlines of cells). Because the image is initially over-marked, the calculations of contour splitting (Zimmer et al., 2002) are not needed.

The image f_{ij} is a digital image of sliced brain tissue which defines the optical density (gray scale value) of each pixel (ij) . We assume that the image contains at least one type of object of interest (neurons) mixed with other objects (non-neurons). The goal of a single run of the segmentation is to “segment” a single object of interest (a single neuron) from the rest of the image (all other neurons, non-neurons, and background). It does this by “evolving” a loop of pixels called a *contour* (C) from a circle of typical neuron diameter ($12\mu m$) starting at one of the over-marked starting points, to a location and shape that surrounds a potential neuron cell body (Fig. 3.4b). This process is repeated for each starting location until all starting locations have been exhausted.

The movement of C is controlled by a set of N points called *control points* $\{(x_n, y_n)\}_{n=1..N}$ for which we use the compact notation (Cremers et al., 2000)

$$z = (\mathbf{r}_1, \dots, \mathbf{r}_N) = (x_1, y_1, \dots, x_N, y_N) \quad (3.1)$$

The control points are parameters in a closed quadratic Bezier-spline (B-spline) curve (Blake and Isard, 1998) that define the exact location (pixels) of C (see Fig. 3.5 for definition). Hence, C moves and changes shape by the iterative motion of the control points z . At each time step, each control point z makes a small movement towards encircling an object close to its starting location by minimizing a total energy E based on two energy considerations,

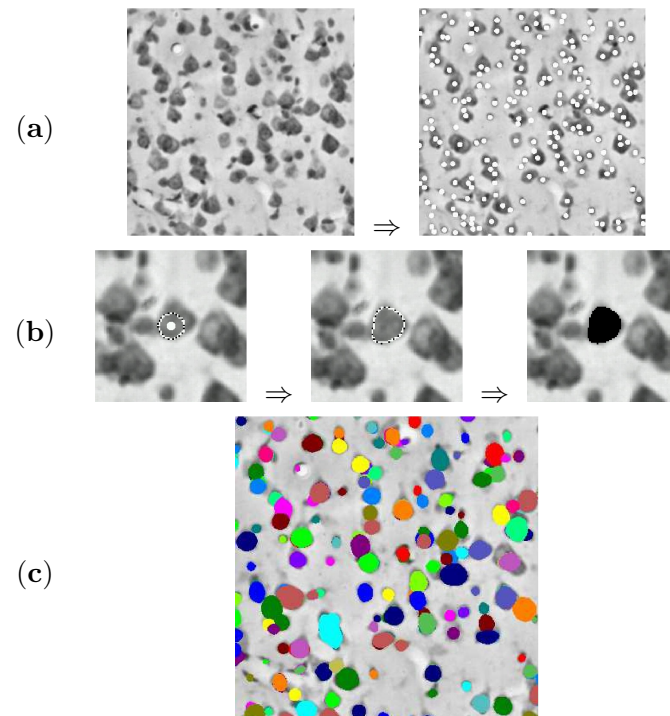


Figure 3.4: **(a)** Over-marking the image with a hexagonal grid of points that lay on the thresholded foreground and center points of a traditional watershed segmentation. Points within 5 pixels are combined to avoid redundancy. **(b)** Active contour segmentation: using each starting location found in **(a)**, a segmentation (clustering) process is performed within a small region of the image to find one possible neuron cell body. This process is then repeated for each starting location until all starting locations are exhausted. **(c)** The final set of *computer segments*, shown in different solid colors, is the output of the OSM.

E_{MS} and E_c :

$$E(f, u, C) = E_{MS}(f, u) + \alpha E_c(C) . \quad (3.2)$$

A qualitative understanding of the energy terms is presented in Fig. 3.7. E_{MS} is the Mumford-Shah energy term, which determines how well the contour separates lighter and darker gray scale regions in the image f_{ij} . $E_c(C)$ is the contour energy term, which quantifies the similarity of the contour to a previously chosen set of training shapes (in our case, the training shapes are oval-like). E_{MS} is high when C does not separate different contrasts well, and is low if it does. $E_c(C)$ is high if the shape is very contorted, and low if it is oval-like. α changes the relative influence of the two energy terms. If α is a high value, then C will evolve into a rigid perfect oval, ignoring all image information. If α is zero, then C will surround any nearby object in the image with no regard to the final shape of C . When the two energy terms are balanced with an appropriate α and the system is evolved to minimize E then objects in an image are encircled properly. Fig. 3.6 shows a typical evolution of C with an appropriate α value. u_{ij} is a variable image, similar to a blurred version of f_{ij} , which is used in the algorithm, as described below.

The *Mumford-Shah energy term* $E_{MS}(f, u)$ quantifies the alignment of the contour with edges in the image f_{ij} :

$$E_{MS}(f, u) = \frac{1}{2} \sum_{ij} \{ (f_{ij} - u_{ij}(t))^2 + \lambda^2 |\nabla u_{ij}(t)|^2 \} \quad (3.3)$$

where λ is the Mumford-Shah energy parameter that determines relative strengths of the terms. $|\nabla u_{ij}(t)|^2$ is the square of the magnitude of the picture gradient:

$$|\nabla u_{ij}(t)|^2 = \left(\frac{\partial u}{\partial x} \right)^2 + \left(\frac{\partial u}{\partial y} \right)^2 = \frac{[u_{i+1,j}(t) - u_{i-1,j}(t)]^2 + [u_{i,j+1}(t) - u_{i,j-1}(t)]^2}{4} \quad (3.4)$$

It should be noted that Cremers et al. (2000) includes an additional term $\nu \|C\|$ to Eq. 3.3, which minimizes the length $\|C\|$ of the contour within its evolution. We do not include

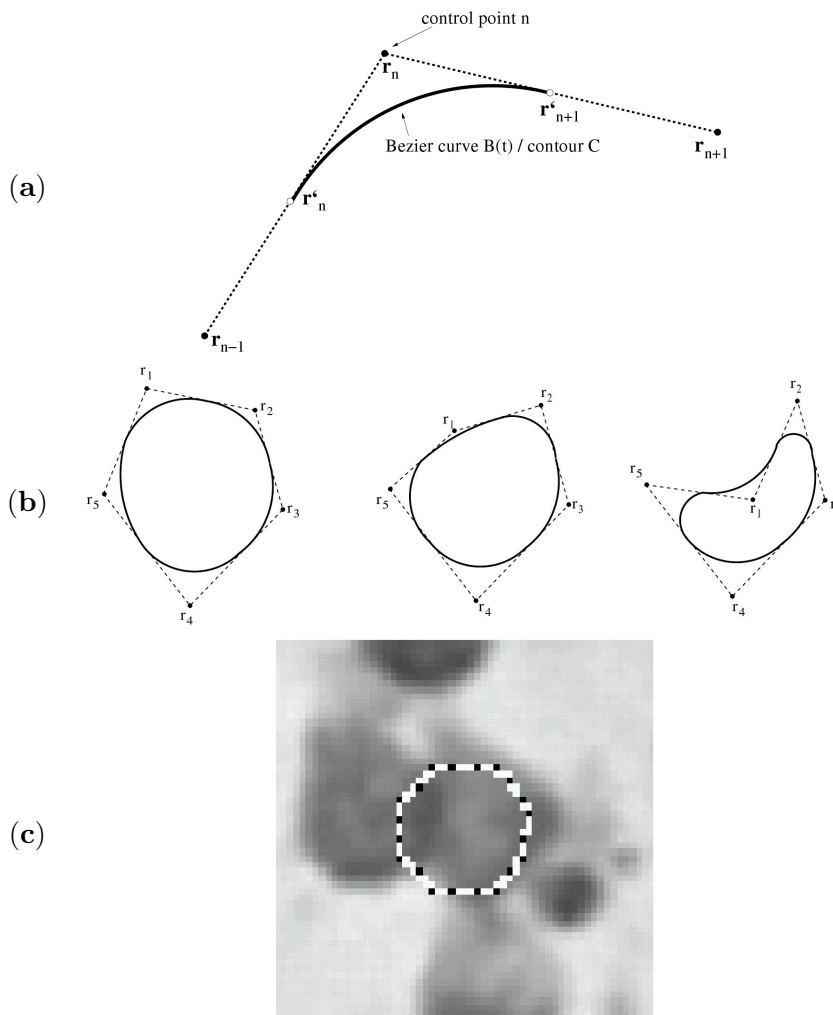


Figure 3.5: (a) The contour C is described by the control points $\mathbf{r}_1, \mathbf{r}_2, \dots, \mathbf{r}_N$. (a) Quadratic Bezier curve $B(t)$ is defined for control point n using the control points \mathbf{r}_{n-1} , \mathbf{r}_n , and \mathbf{r}_{n+1} . The points \mathbf{r}'_n are halfway between \mathbf{r}_{n-1} and \mathbf{r}_n . The equation for the contour is $B(t) = (1-t)^2\mathbf{r}'_n + 2t(1-t)\mathbf{r}_n + \mathbf{r}'_{n+1}t^2, t = 0..1$. The equations guarantee that at the points \mathbf{r}' the curve is continuous and smooth. Combining several Quadratic Bezier curves creates a quadratic B-spline contour. An example with 5 control points is presented in (b) which shows how the B-spline contour moves when one control point (\mathbf{r}_1) moves. (c) Contour C (white pixels) with 20 control points (single black pixels) that is overlaying the image.

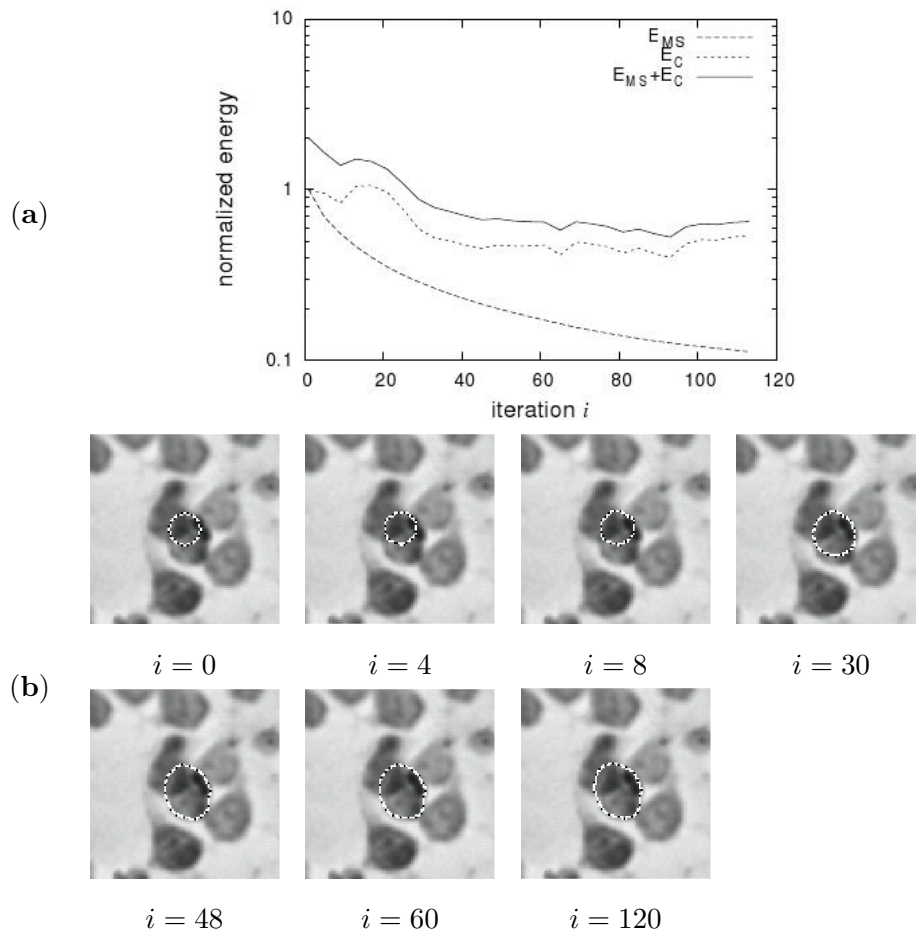


Figure 3.6: Examples of the active contour movement within the image during the OSM segmentation phase. The number of control points (black dots) is 20. The B-spline contour is white. The contour starts at a location determined by the over-marking step of the OSM. **(a)** Evolution of the energy terms E_{MS} and E_c **(b)** Contour evolution after 0, 4, 8, 30, 48, 60, and 120 steps. When a local minima is reached, the contour no longer moves, and the points internal to the contour are saved.

this term because it adds an additional free parameter and does not contribute to the functionality of the algorithm when identifying cell shaped objects.

Eq. 3.3 is differentiated with respect to control point movement. Setting the solution of the differentiation to a minimum of $E_{MS}(f, u(t))$ gives the evolution equation for each individual control point $n = 1..N$ during each iteration dt (Mumford and Shah, 1989):

$$\begin{aligned}\dot{x}_n(t) &= (e^+ - e^-) \mathbf{n}_x \\ \dot{y}_n(t) &= (e^+ - e^-) \mathbf{n}_y,\end{aligned}\tag{3.5}$$

where e^+ and e^- are E_{MS} (Eq. 3.3) summed over the single line of pixels right outside (e^+) and right inside (e^-) the segment of C centered around control point (x_n, y_n) (Fig. 3.8). \mathbf{n}_x and \mathbf{n}_y are the outer normal vectors of C at each control point \mathbf{r}_n in the x and y direction respectively. $\dot{x} = dx/dt$ and $\dot{y} = dy/dt$, where t is the artificial time parameter.

Eq. 3.3 is then differentiated with respect to the variable image u_{ij} . Setting the solution to a minimum of $E_{MS}(f, u(t))$ gives the evolution equation for each pixel u_{ij} during each iteration dt (Mumford and Shah, 1989):

$$u_{ij}(t + dt) = \begin{cases} u_{ij}(t) + \{f_{ij} - u_{ij}(t) + \lambda^2 \nabla^2 u_{ij}(t)\} dt & \text{if } ij \ni C \\ u_{ij}(t) & \text{if } ij \in C \end{cases}\tag{3.6}$$

At $t = 0$, $u_{ij}(0) = f_{ij}$. $\nabla^2 u_{ij}(t)$ is the Laplacian in 2-D Cartesian coordinates:

$$\nabla^2 u_{ij}(t) = \left(\frac{\partial^2 u}{\partial x^2} \right) + \left(\frac{\partial^2 u}{\partial y^2} \right) = u_{i+1,j} + u_{i-1,j} + u_{i,j+1} - u_{i,j-1} - 4u_{i,j}\tag{3.7}$$

Eq. 3.6 describes a diffusion ($\nabla^2 u_{ij}(t)$) process limited by the original image ($f_{ij} - u_{ij}(t)$). The key component is that u_{ij} never evolves at the pixels that make up C . u_{ij} becomes stable once C separates contrasted regions. Therefore, minimizing E_{MS} tends to evolve C so that the gray scale values vary slowly (smoothly) in the areas inside and outside the contour but vary strongly (discontinuously) across the contour C .

The *contour energy term* E_c affects the shape of the contour irrespective of the images f_{ij} and u_{ij} . E_c is minimized for contour shapes most similar to a previously chosen set of training shapes $\chi = \{z_1, z_2, \dots\}$. The energy is calculated using the following equation:

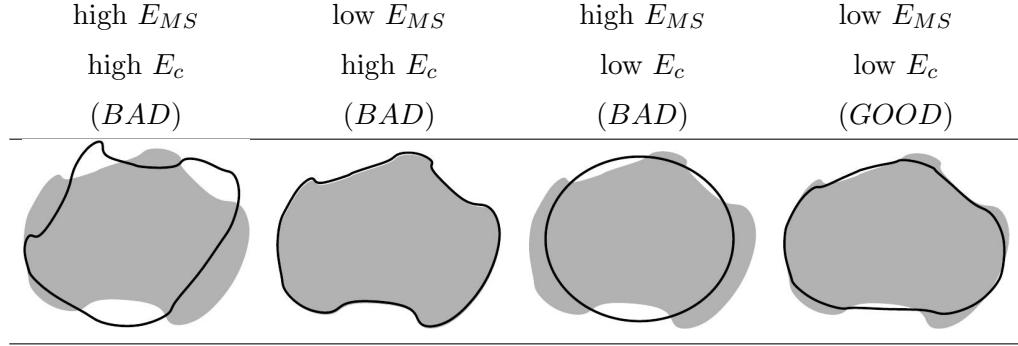


Figure 3.7: Schematic drawing showing the relative energies of E_{MS} and E_c for the same image (shown as gray) and four different contour shapes (shown as black loops). The first three cases are examples of improperly fit contours with a high overall energy $E = E_{MS} + \alpha E_c$. The last case is an example of an optimal contour minimizing the overall energy.

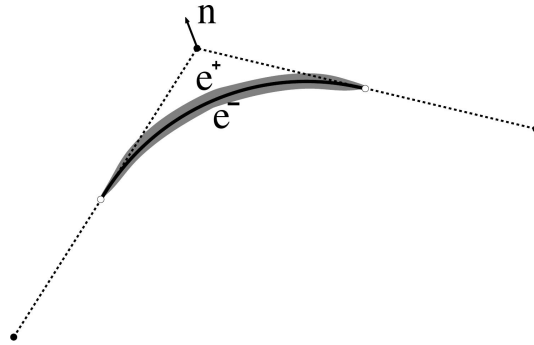


Figure 3.8: Control point movement based on E_{MS} follows Eq. 3.12. The terms e^+ and e^- are E_{MS} (Eq. 3.3) integrated over the single line of pixels right outside (e^+) and right inside (e^-) of the contour centered around each control point n . \mathbf{n}_x and \mathbf{n}_y are the x and y components of the outer normal vector of C at the control point.

$$E_c(C) = \frac{1}{2} (z - z_0)^T \Sigma^{-1} (z - z_0) , \quad (3.8)$$

where the vector z_0 and the matrix Σ (with an inverse Σ^{-1}) contain the mean and covariant information of the previously chosen set of training shapes $\chi = \{z_1, z_2, \dots\}$:

$$z_0 = \langle z_i \rangle \quad (3.9)$$

$$\Sigma = \langle (z_i - z_0)^T (z_i - z_0) \rangle , \quad (3.10)$$

Here $\langle \rangle$ denotes the sample average. z_0 is a $2N$ vector and Σ is a $2N \times 2N$ matrix. Creating z_0 and Σ for a set of shapes $\chi = \{z_1, z_2, \dots\}$ is equivalent to modeling the distribution of shapes in \mathbb{R}^{2N} as a Gaussian distribution (Cremers et al., 2000).

To minimize $E_c(C)$, the following evolution equation for each control point is used:

$$\dot{z}(t) = \Sigma^{-1} (z(t) - z_0) . \quad (3.11)$$

Combining the two equations 3.5 and 3.11 gives the final evolution equation for each control point n during each iteration:

$$\begin{aligned} x_n(t + dt) &= x_n(t) + \left\{ (e^+ - e^-) \mathbf{n}_x + \alpha [\Sigma^{-1} (z(t) - z_0)]_{2n-1} \right\} dt \\ y_n(t + dt) &= y_n(t) + \left\{ (e^+ - e^-) \mathbf{n}_y + \alpha [\Sigma^{-1} (z(t) - z_0)]_{2n} \right\} dt , \end{aligned} \quad (3.12)$$

recalling that e^+ and e^- are E_{MS} (Eq. 3.3) summed over the single line of pixels right outside (e^+) and right inside (e^-) the segment of C centered around control point (x_n, y_n) (Fig. 3.8), and are dependent on λ and u_{ij} .

The evolution of the contour is driven by Eqs. (3.12,3.6), with variables u_{ij} and contour points $(x_1, y_1, \dots, x_N, y_N)$. Note that Eqs. (3.12,3.6) are coupled and must be solved simultaneously.

Performing a step by step evolution of the control points (Eq. 3.12) and u_{ij} (Eq. 3.6), C evolves in the following way: If C begins to change into a contorted, non-ovular shape to

minimize E_{MS} (such as “leaking” out of an area of weak or missing boundary information in the image), then E_c will increase, hence there will be a force opposing the movement. Similarly, if the contour begins to move back to a perfect oval to minimize E_c , E_{MS} will increase and thus limit such a change. When a local minimum is reached and the contour no longer moves, the points internal to the contour are saved, and the process starts again at a new location until all starting locations are exhausted.

There are several free parameters (α , λ , dt , N , etc.) that must be set within the OSM algorithm. Some of these parameters, called *secondary parameters*, do not greatly affect the evolution, and can be set the same for all Nissl-stained images. The secondary parameters are as follows: N is set to 20, so that for a typical 80 μm circumference of a neuron cell body, neighboring control points are 3 μm , or roughly 4 pixels away from each other. z_0 and Σ define the training that depend on the typical shapes of the object of interest, in our case a neuron. We build these parameters by creating a sample of 100 ellipses, ranging linearly from an eccentricity of 0 to 0.4, a simple representation of the average shape of neuron cell bodies. To speed up the evolution, we allow for different “time” steps and Mumford-Shah parameters in Eqs. (3.12,3.6). In Eq. 3.12, $dt \rightarrow dt_c$ and $\lambda \rightarrow \lambda_c$. In Eq. 3.6, $dt \rightarrow dt_u$ and $\lambda \rightarrow \lambda_u$. In this schema, dt_c , dt_u , and λ_u can be set as secondary parameters which do not need to change for any of the pictures. We set $dt_c = 100$, $dt_u = 0.05$, and $\lambda_u = 1$.

In addition to the secondary parameters, there are two *primary parameters* which greatly affect segmentation, and must be determined empirically: the energy ratio α between E_{MS} and E_c , and the energy parameter λ_c within the E_{MS} term.

Because the active contour algorithm described above was designed for generic object recognition, the algorithm itself (in addition to the free parameters) can be “tuned” for the task of finding dark elliptical features that are overlapping or relatively close to each other on a lighter background. We adjust the above algorithm in a simple way to accommodate overlapping: if $f_{ij} - u_{ij}(t) > 0$ near and inside the given control point, the contour is “leaking” out to find the edge of another feature next to it. We therefore multiply this control point’s contribution to E_{MS} by a free parameter η greater than 1. Here, η is a

secondary parameter, and is set to 1.5 for all images.

We now discuss each step in ANRA.

3.2.3 Step I: Image Acquisition

We test ANRA on Nissl-stained tissue samples of seven young adult (6.4-11.8 years; mean 8.5 years) and seven aged (24.7-32.9 years; mean 30.1 years) female Rhesus monkey subjects that were part of an ongoing study of the effects of aging on cognitive function (Cruz et al., 2004). For each subject, eight (4 from each of 2 sections) gray scale (1-256) 512x512 pixel images with 1.5 pixels/micron resolution (~ 150 neurons per image) were taken from area 46, layer 3 of the prefrontal cortex in the ventral bank of sulcus principalis. 3 subjects had appreciable differences in image quality between the two sections, therefore the total number of different subject/image-qualities is 17. Fig. 3.1b shows 12 of the 17 subject/image-qualities.

3.2.4 Step II: Segmentation Training

All images are normalized as described in Sec. 3.2.1. Out of each of the 17 subject/image-qualities, one image is randomly selected as a *training image*. The digital image is marked for neuron cell bodies by an expert observer who “paints” sets of pixels over the neurons using a small graphical program. Different objects can share pixels, or overlap, but the sets exist as separate entities even if there is an overlap. We designate these sets of pixels created by an expert observer the *training segments*. The training segments will be compared to *computer segments* from the OSM output. The manual identification is relatively quick (2-4 seconds per neuron), and does not require a model image, ie: no feature overlap (Lin et al., 2005). Furthermore, the cell marking method creates knowledge of the extents of each cell body as viewed by an expert observer, independent of and unbiased to our segmentation procedure. This information is saved and used repeatedly for multiple training runs as needed, and does not have to be repeated for the same image if different training parameters are checked (Lin et al., 2005; ?).

We next determine the values of the primary parameters α and λ_c , the two primary free parameters which greatly affect the segmentation. We find that there is significant loss in functionality when α is outside the $[10^{-9}, 10^{-8}]$ range and λ_c is outside the $[1, 5]$ range. We therefore search this space of α and λ_c by comparing the resulting computer segments to the training segments. A training segment is “found” if the computer segment shares more than 70% of the pixels with the training segment (Fig. 3.9). The set called the final OSM parameters, denoted α^* and λ_c^* , is the set that correctly identifies 95% or more training segments. The (α^*, λ_c^*) values are then recorded and used for the rest of ANRA.

The OSM with the correct primary parameters (α^*, λ_c^*) identifies 95% or more of neurons in the images, but it also identifies other non-neuron objects, such as staining errors, glial cells, and improper coverings of neurons. To separate neurons from non-neurons, computer training is performed.

First, we compare the (α^*, λ_c^*) -parameter OSM computer segments to the training segments. Each computer segment is either placed in the neuron segment category or non-neuron segment category based on whether the segment mutually overlaps any training segment (Fig. 3.9). Second, each segment is represented by seven *segment properties* $\mathbf{v} = (v_1, v_2, \dots, v_7)$. The seven segment properties were chosen to be the most salient measures of identifying neurons within an image. For the calculations of the segment properties, we denote the total number of pixels within the segment as A_c and the total number of pixels within the contour as $|C|$. The properties are based on the optical density of the original image f_{ij} as well as the square of the magnitude of the image gradient $|\nabla f_{ij}|^2$. The segment properties are presented in Table I. \sum^A is a sum over all of the pixels within the segment area, \sum^C is a sum over the edge pixels of the segment circumference, r_c is the location of the center of the segment, and r_{ij} is the location of the pixel (ij) .

Table I

	description	equation
v_1	segment area	A_c
v_2	average optical density (\bar{f})	$\frac{1}{A_c} \sum^A f_{ij}$
v_3	variance of optical density	$\frac{1}{A_c} \sum^A (f_{ij} - \bar{f})^2$
v_4	radius of gyration of optical density	$\frac{1}{A_c} \sum^A r_{ij} - r_c f_{ij}$
v_5	segment edge length ($ C $) vs. segment area	$ C /A_c$
v_6	average gradient of segment edge	$\frac{1}{ C } \sum^C \nabla f_{ij} ^2$
v_7	average change in gradient of segment edge	$\frac{1}{ C } \sum^C \nabla f_{i+1j} ^2 - \nabla f_{ij} ^2$

Using the WEKA machine learning toolkit (Witten, 2005), we assess the following machine learning algorithm's ability to discriminate between neuron property vectors $\{\mathbf{v}_1^+, \mathbf{v}_2^+, \dots\}$ and non-neuron property vectors $\{\mathbf{v}_1^-, \mathbf{v}_2^-, \dots\}$: the 1-rule classifier (Holte, 1993), naive Bayes classifier (John, 1995), support vector machine classifier (Platt, 1998), nearest neighbor classifier (Aha, 1991), decision tree classifiers (Quinlan, 1993), Bayes net and multi-layer perceptron (Witten, 2005). The cost between Type 1 errors (marking a non-neuron property vector as a neuron) and Type 2 errors (marking a neuron property vector as a non-neuron) is scanned by tuning the cost ratio term in the training algorithm. A stratified cross-validation evaluation for various cost ratios (3:1, 2:1, ..., 1:3) creates a receiver operator characteristic (ROC) curve (Duda et al., 2001) for each training method (Fig. 3.10). The Multilayer Perceptron (MLP) using a single, 4-node hidden layer, has the best ROC curve, as it provides the highest percentage of neuron property vectors identified and the smallest percentage of non-neuron property vectors incorrectly identified. MLP is therefore chosen as the main training method for ANRA.

3.2.5 Step III: Application

Automatic neuron recognition is now applied on an unlimited number of other images that are normalized and similar in morphology to the training images. The steps are as follows:

1. The OSM with the primary parameters (α^*, λ_c^*) is performed on the new image.
2. The properties \mathbf{v} are calculated for each computer segment.

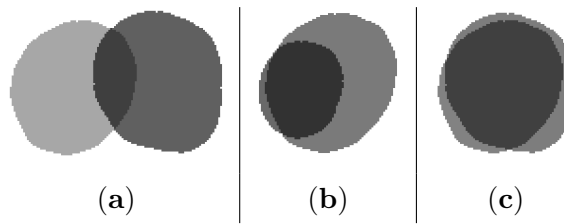


Figure 3.9: Two segments represent the same object when they *mutually* share more than 70% of their pixels. The two segments in (a) do not pass the required criteria because neither segment overlaps the other by more than 70%. The two segments in (b) do not pass the required criteria because only one segment overlaps the other by more than 70%. Only in (c) does the required overlap occur. This analysis is used when computer segments are compared to “gold standard” training segments and either designated a neuron or non-neuron, and during the overlap deletion phase, when the segment with the highest probability of being a neuron is selected among all overlapped segments.

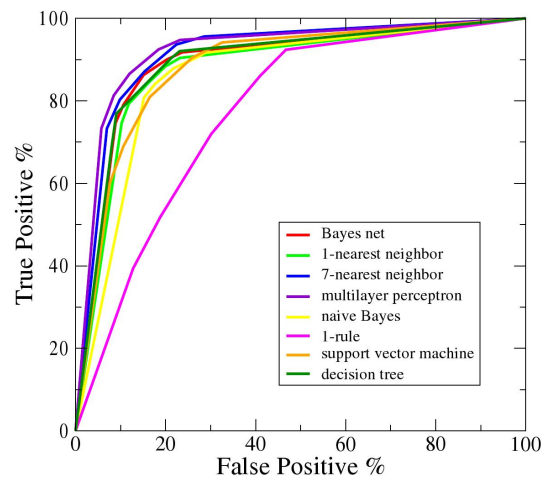


Figure 3.10: Receiver operating characteristic (ROC) curve for each training method evaluated. It is seen that the Multilayer Perceptron (MLP) has the best ROC curve - the highest percentage of neuron property vectors identified with the smallest percentage of non-neuron property vectors incorrectly identified. MLP is chosen as the main training method for ANRA.

3. A cost ratio is selected by the user.
4. All computer segments deemed non-neurons by the MLP are discarded.
5. For any two remaining computer segments that mutually overlap by more than 70%, the computer segments with the smaller probability of being a neuron (as determined by the MLP) is discarded.

The (x,y) centers, sizes, and shapes of the remaining computer segments are the final result of ANRA.

3.2.6 Comparison method

A semi-automatic method (semi-auto) was used in prior neuron density maps correlation studies (Cruz et al., 2005). In the semi-auto method a combination of computer software and human intervention for each image is employed to identify neurons. Because the amount of human intervention scales with the number of images analyzed, the semi-auto method represents a standard with which we evaluate our completely automated recognition method.

3.2.7 Density Map Method and Microcolumnar Strength

We give a description of the density map method, as it is the main analysis to be applied to the results of ANRA. The density map method was initially described by Buldyrev et al. (2000) and a more detailed description and validation was given by Cruz et al. (2005). The density map is a 2D representation of the density correlation function $g(x,y)$, which uses as input the (x,y) locations of all neurons in the region of interest (ROI). This function $g(x,y)$ is mapped to a two-dimensional gray scale image (density map) in which different shades of gray are proportional to the average local neuronal density. Thus, the density map quantifies the average neuronal neighborhood surrounding a typical neuron within the ROI.

Operationally, the density map is calculated by first assigning indices ($i = 1, 2, 3 \dots N$) to all the neurons in the sample. Next, we center a grid of bins of size D over each neuron

and count how many other neurons fall in each bin constructing one matrix of accumulated neurons $m(x, y)$. We define $g(x, y) = m(x, y)/N \cdot D \cdot 2$, in which $g(x, y)$ has units of an average density of objects at position (x, y) . As an example, the density map would be uniform if locations of objects (neurons) are uncorrelated, but will show patterns when there are regular spatial arrangements between the objects.

For the case of neurons forming microcolumns, their density map exhibits one central vertical ridge, sometimes accompanied by two less pronounced parallel neighboring ridges. For this study, we are interested in the microcolumn strength S , which is extracted from the density map by taking the ratio of the neuronal density within the average microcolumn to the average neuronal density (Cruz et al., 2005). For the same images, S is calculated using ANRA (x, y) locations as well as semi-automatic (x, y) locations, and the results are compared.

3.3 Results

For each of 17 subject/image-qualities, an *evaluation image* is randomly selected from the remaining images and marked for neuron cell bodies by the expert. The evaluation image is used as a “gold standard” to assess the accuracy of ANRA and the comparison methods. A total of 2448 “gold standard” neurons are analyzed, for an average of 144 neurons per subject/image-quality. For each of the two recognition methods (semi-auto and ANRA), we compare the method’s identified neurons to the “gold standard”, and retrieve the following numbers (Fig. 3.11):

$$a = \text{number of correctly identified neurons} , \quad (3.13)$$

$$b = \text{number of non-neurons incorrectly identified as neurons} , \quad (3.14)$$

and

$$c = \text{number of non-identified neurons} . \quad (3.15)$$

To compare methods for the different subject/image-qualities, we define the following normalized metrics:

$$A = \frac{a}{a + c} \cdot 100 , \quad (3.16)$$

and

$$B = \frac{b}{a + c} \cdot 100 . \quad (3.17)$$

A is the percent of correctly identified neurons (“true positives”). B is the percentage of non-neurons that are incorrectly identified as neurons (“false positives”).

The results are shown in Fig. 3.12. The semi-auto method is characterized by one (A, B) set. Because of the ability to adapt the cost ratio as described in Sec. 3.2.5, ANRA is shown at 7 different ratios (3:1, 2:1, 1:1, 1:2, 1:3, 1:5, and 1:10), ranging from very selective, to no selectivity, creating an “adapted” ROC curve. Since each point is an average of the 17 subject/image-qualities, the error bars show the standard deviation of the spread for both A and B . We choose the 1:2 cost ratio for further analysis because it is at the inflection point of the “adapted” ROC curve, and it has the closest average (A, B) to that of semi-auto. Table II and Fig. 3.13a shows the individual results for each subject/image-quality for the semi-auto method and the ANRA with 1:2 cost ratio. Fig. 3.13b shows an example of semi-auto and ANRA points compared to the gold standard.

Table II

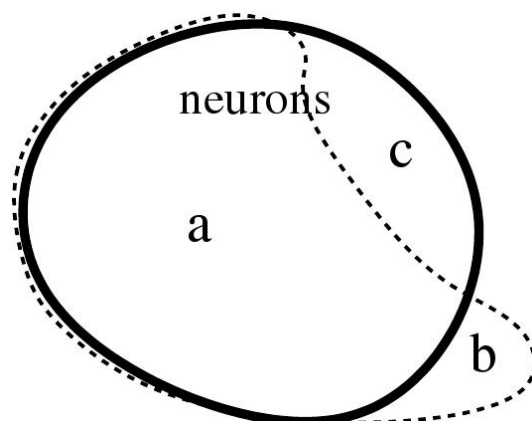


Figure 3.11: Venn diagram showing the relative quantities for evaluating the quality of a neural recognition method. The bold black line separates neuron from non-neuron objects in the image. The dotted area shows the objects that are identified by a method. The method correctly identifies most of the neurons (**a**), but misses some neurons (**c**) and identifies some non-neurons as neurons (**b**). Using the quantities **a**, **b**, and **c**, standardized percentages of neuron vs. non-neurons can be calculated.

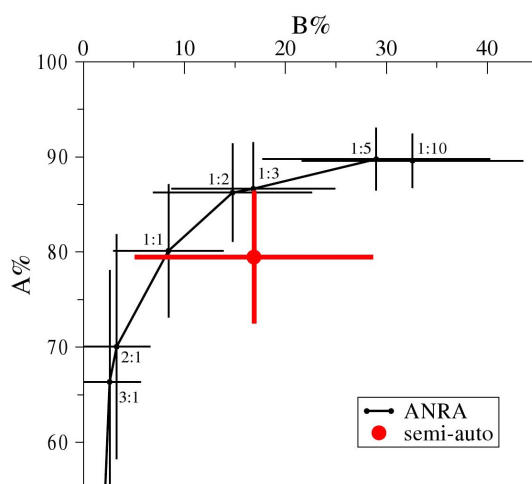


Figure 3.12: Results of ANRA. The semi-auto method is characterized by one (A, B) set. Because of the ability to adapt the cost ratio as described in Sec. 3.2.5, ANRA is shown at 7 different ratios (3:1, 2:1, 1:1, 1:2, 1:3, 1:5, and 1:10), creating an “adapted” ROC curve. Since each point is an average of the 17 subject/image-types, the error bars show the standard deviation of the spread for both A and B.

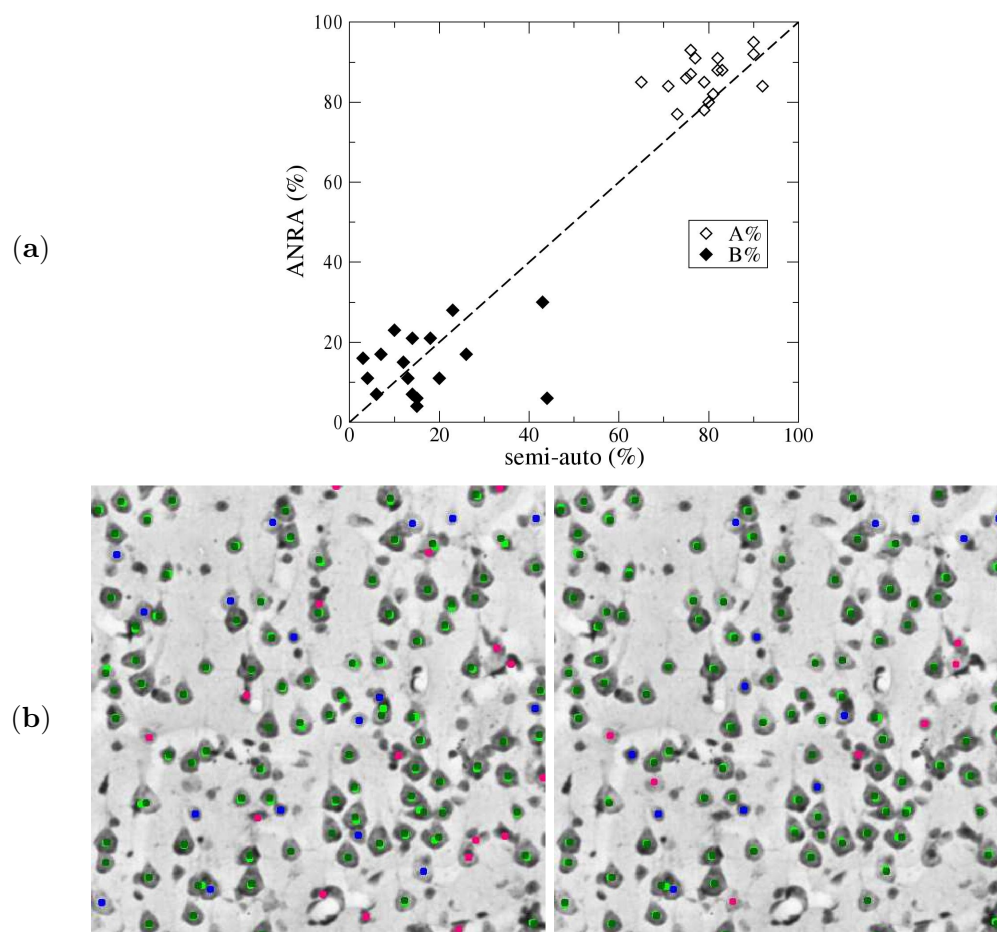


Figure 3.13: (a) Individual results for 17 subject/image-types for the semi-auto method and the ANRA (with 1:2 cost ratio). (b) Recognition results for the semi-auto method (left) and the ANRA method (right) for example subject/image-quality #1 (Table II). Dark green: gold standard marks that match with the method. Blue: gold standard marks that DO NOT match with the method. Light Green: method points that match with gold standard points. Pink: method points that do not match with gold standard points.

#	semi-auto		ANRA	
	A(%)	B(%)	A(%)	B(%)
1	81	13	82	11
2	71	14	84	7
3	82	14	91	21
4	79	15	78	4
5	90	43	92	30
6	65	3	85	16
7	76	18	87	21
8	83	15	88	6
9	76	12	93	15
10	79	10	85	23
11	73	6	77	7
12	82	4	88	11
13	92	44	84	6
14	90	26	95	16
15	80	20	80	11
16	77	23	91	28
17	75	7	86	17
avg.	80±7	17±12	86±5*	15±8

The results show that ANRA has a significantly higher A value of recognition (P-value: 0.002) and a similar B value of recognition compared to the semi-auto method.

We also compare microcolumnar strength S (Sec. 3.2.7) using the (x, y) locations from both ANRA and semi-auto methods of neuron identification for the entire image database of rhesus monkey subjects as described in Sec. 3.2.3. 14,000 neuron locations were used, for an average of 1000 neuron locations for each subject. We find significant correlations between microcolumnar strength measurements of the ANRA and semi-auto methods of neuron recognition (Fig. 3.14). This shows that ANRA has the ability to find significant changes in advanced neuron spatial arrangements within different subjects, and can therefore be applied to large datasets where manual or semi-auto recognition are not viable.

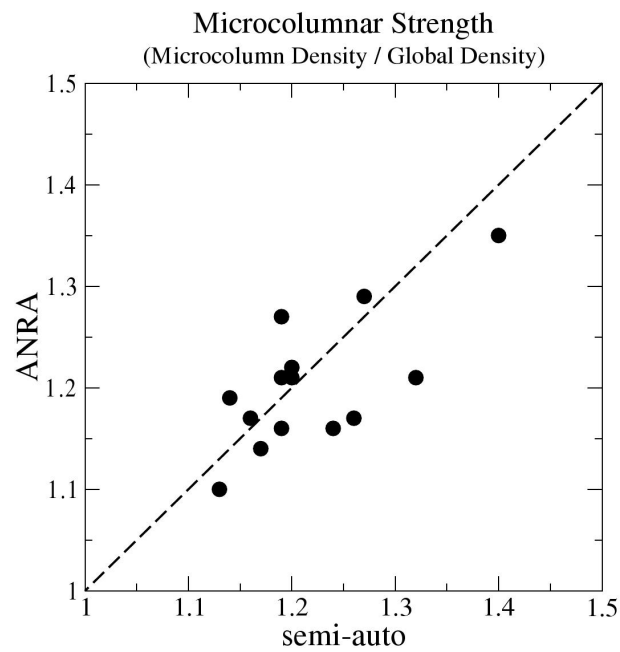


Figure 3.14: Comparison of microcolumnar strength measurement (S) using the (x, y) locations from both ANRA (with 1:2 cost ratio) and semi-auto methods of neuron identification. A total of 14,000 neuron locations were used, for an average of 1000 neuron locations for each subject (plot point). Both the neuron density and microcolumnar strength show significant correlations of ANRA with the semi-auto method.

3.4 Discussion

In the present work we introduce a method called an Automated Neuron Recognition Algorithm (ANRA) which uses a combination of image segmentation and machine learning to retrieve neuron locations within digitized images of Nissl-stained Rhesus monkey brain tissue. Despite challenges, such as overlapping of neuron cell bodies and the presence of glial cells and artifacts in the tissue, we demonstrate that ANRA has a significantly better recognition capability than a semi-auto method (Cruz et al., 2005) which requires expert manual intervention for each image. ANRA's recognition quality is combined with computational efficiency, resulting in recognition of ~ 100 neurons per minute using a standard personal computer. Consequently, large numbers of neuron locations can be retrieved, spanning considerably larger brain regions than ever before. Furthermore, because ANRA is capable of efficiently extracting neuron locations from durable and commonly used Nissl-stained tissue, it can potentially be applied to vast stores of archival material existing in laboratories and research collections around the world.

Such a large dataset of (x,y) neuron locations will allow for a variety of systematic analyses that have previously not been possible. The ability to identify every neuron in entire sections of the brain will allow for both global and local analyses of neuron numbers, glial cell numbers, regional cell densities, and local variations in cell densities. Also, as was shown in the Results section, studies of microcolumnarity or other spatial features of cortex, including spatial inter-relationships among neurons and glia using autocorrelation and cross-correlation, are possible. Lastly, ANRA also allows for less obvious applications, including the investigation of the spatial network of the brain using the neuron locations as nodes. None of these studies are possible with the elegant sampling methods of modern stereology.

We highlight the need for large datasets of neuron locations ($10^3 - 10^4$) in comparative studies proposed in the Introduction and defined in Sec. 3.2.7. Generally, the goal of a comparative study is to find a statistically significant difference in a measured quantity

(i.e., microcolumn strength) due to a change in an independent variable (age, species, sex, disease state, etc.). In the case of a 1D correlation between nearest neighbors or the 2D microcolumnar analysis, the neuron locations are used to create 1D and 2D histograms, respectively. The number of neurons must be high enough to resolve the effect of the independent variable above random noise of the histogram. Buldyrev et al. (2000) showed that for a resolution of interest (seeing 3% changes between 10 micron bins), $\sim 10^4$ neuron locations are needed in the comparative study of microcolumnarity. For the same resolution in a 1D correlation comparative study, such as nearest-neighbor distances, only ~ 1000 neurons are needed (Schmitz et al., 2002). For a given bin size, the theoretical calculation shows that the required number of neurons scales as a power of dimensions that are being correlated. Thus, automatic recognition becomes critical in higher dimension correlations. As an example we consider a 30 subject study of neuron spatial arrangement using $\sim 10^5$ neuron locations, making 100 different measurements of 1000 neurons each through a certain layer across several Brodmann regions. The semi-automatic approach, which allows for acquisition of 10 neurons per second, would take 83 human hours to complete. Comparatively, ANRA could complete the same task in 24 hours on 20 Intel P4 processors with less than 1 hour of preparation time.

ANRA has a further advantage of reducing experimental drift. Specifically, in terms of human bias, the “criteria” for neuronal identification will necessarily differ between different observers that are often required for a huge analysis extending over months to years, while ANRA’s criteria, once established from the training algorithm, remains constant. Furthermore, ANRA’s criteria will not be subject to the kind of experimental drift that can occur over time when one observer manually identifies thousands of neurons over a period of weeks to months.

Recently, there have been advances in level set methods to recognize overlapped cell nuclei (?). The recognition challenges with Nissl-stained tissue are far greater than the challenges using confocal microscopy using fluorescence. ? show how neurons and glia cells completely separate into two regions of parameter space using only two parameters

(texture and intensity) of the identified segmentations. If plotted in a similar way, no two parameters that we consider (size, intensity, texture, gyration, edge vs. area, etc.) would yield such a separation. Thus, in a Nissl-stained tissue visualized by optical microscopy, the parameterized method of Cremers et al. (2000), which, by design, overcomes the challenges of noisy images and missing boundary data (Sec. 3.2.2), is most efficient.

Our results suggest that the ANRA method is performing as maximal efficiency: when a second expert's marks are compared with the gold standard on the same Nissl-stained image, the performance ($A = 88 \pm 5\%$) is not significantly higher than ANRA's performance ($A = 86 \pm 5\%$).

Although there are 10 free parameters within the algorithm, only two of them called the *primary parameters* must be explored to find the correct values for proper segmentation. These *primary parameters* are automatically found in the OSM parameter search during training. The other eight free parameters, which we call the *secondary parameters*, can be fixed for the general task of identifying elliptical features within noisy images with missing boundary data, thereby solidifying them for the broadly applicable problem of neuron recognition in all Nissl-stained tissue. For a given morphological feature of interest, once a small set of representative images have been trained to, the training and parameters can be reused, due to the normalization of images of different quality. This setup will allow for the study of large areas of montaged images, or large datasets of hundreds of slides, all with the same training. Furthermore, the free parameters and training can be adapted for identification of other types of neurons, glial cells, etc.

Lastly, because of the modular nature of the method (Fig. 3.2), it will be relatively easy to replace partial aspects of the overall algorithm by considering advances in recent published work. For example, Tscherepanow et al. (2006) independently developed a method to identify living cells that uses a larger set of training properties that is reduced with principle/independent component analysis, and Costa and Bollt (2006) has applied advanced pattern matching to the identification of neuron cell bodies in Nissl-stained tissue. By replacing the respective aspects of ANRA with such methods, the ideal overall identification

algorithm can be found for not only the recognition of neuron cell bodies, but also the recognition of other objects of scientific interest, for example living cells or glial cells.

3.5 Software

The ANRA software is available at <http://physics.bu.edu/~ainglis/ANRA/>.

3.6 Validation by comparing with Stereology

As was stated in Sec. 1.2, the application of design-based stereology to obtain estimates of total cell number has led to valuable insights into structural features of the brain. Although there are many benefits, stereology has some limitations for studies that involve comparatively large regions of interest (ROIs) and large number of subjects. The Automatic Neuron Recognition Algorithm (ANRA) takes advantage of advances in computing power, digital storage, and computer vision algorithms in order to create automatic, objective measurements from stained sections. ANRA endeavors to address stereology's inability to assess heterogeneity, time consuming nature, and risk of experimental drift by attempting to locate all cells within the ROI using computing algorithms which perform similarly over large numbers of sections and cases over extended time periods. In this validation study, we compared neuron numbers retrieved from both stereology and ANRA in the supragranular, granular and infragranular laminar subdivisions of the monkey primary visual cortex. In addition to using color information of the cells to differentiate between brown NeuN+ neurons and blue Nissl-stained glial cells, we employed the novel z-stacking procedure that both increases the depth of field of the 20x objective as well as provides bounding limit information for proper counting of cells. Recognition results showed that ANRA recognizes 95% of neurons cells, with less than 5% false positive rate for both populations (the glial cells were not analyzed in this validation, however the stark color difference between neurons and glial helped with the recognition accuracy). With a test set of 3 monkeys ranging in age from 7.5 - 28.9 years, we applied both ANRA and stereology on the same ROIs within the

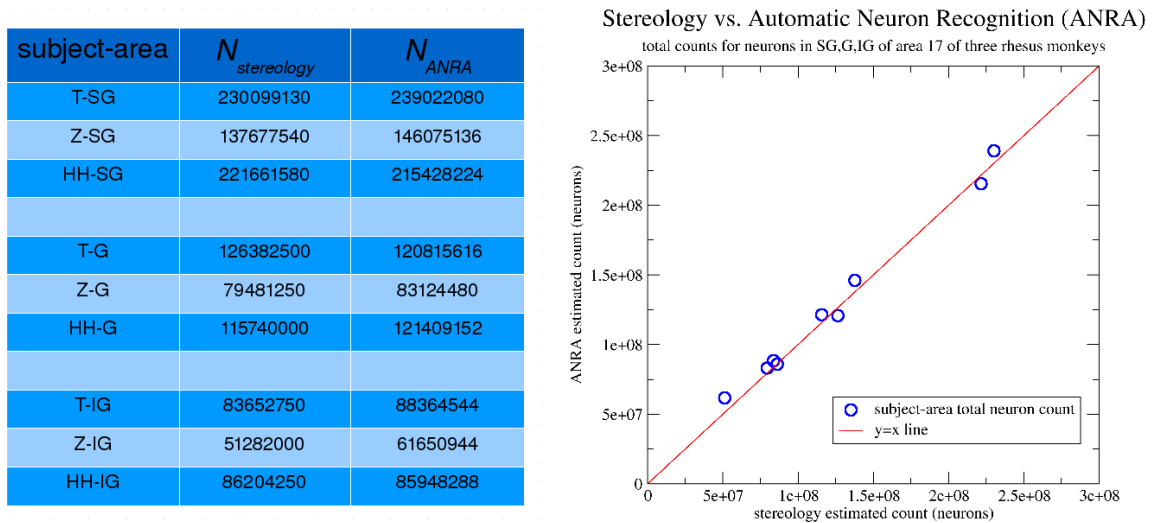


Figure 3.15: Comparison of ANRA with stereology for a neuron counting study

same tissue sections. The equations of importance in the study are total count number that is obtained with stereology versus ANRA. Stereology's equation is

$$N_{stereology} = (OC) \left(\frac{1}{SSF} \right) \left(\frac{1}{ASF} \right) \left(\frac{ATT}{HOD} \right) \quad (3.18)$$

where OC is the object counted, SSF is the section sampling fraction, ASF is the area sampling fraction, and ATT is the average thickness of tissue, and HOD is the height of the disector. The ANRA equation is

$$N_{stereology} = (AC) \left(\frac{1}{ASF} \right) \left(\frac{ATT}{HOD} \right). \quad (3.19)$$

Note that the difference lies in the fact that for each section, whereas the stereologist counts a fraction of cells in that section's ROI , ANRA counts all cells (at sub 100% accuracy). The results are shown in Fig. 3.15. We see that there is strong agreement between the stereological results and that of ANRA. There are several things to note. The exact lay of the correlation on the $x=y$ line, although pleasing, is not the most impressive part of the result. In fact, the author believes that the lay of the trend on the $y=x$ line is due to an increase in the number of cells counted because we put the same guard volume in

as the stereologist into the equation (*averagethicknessoftissue*) when in reality we were counting cells even outside of this volume. This is counteracting with the simplified version of ANRA that was used on the segmentation portion of the algorithm, which has difficulty separating clumps of cells, and is therefore undercounting. The more important result is that the jitter around any best fit line $y = mx + b$ is lower than 10%, which makes it a viable alternative to seeing biological changes in measurement traditionally performed by stereology.

Chapter 4

Results

In this chapter we give the results obtained by the new method focusing on proof of concept and validation of the automatic model. The results revolve around two datasets: the brown rat brain from the University of Arizona, and the macaque monkey brain from the Boston University Medical school.

4.1 Macaque Monkey

4.1.1 Subjects

The subjects for all of the monkey studies came from the same cohort. Animals were selected from the population of monkeys at the Yerkes National Primate Research Center (YNPRC) at Emory University according to strict selection criteria that excluded any monkeys with health or experimental histories that could have affected the brain and cognitive functions. The life span of the rhesus monkey compared to the human corresponds approximately to a ratio of 1:3. Monkeys, can be considered young adults at age 5 when they reach sexual maturity and would roughly correspond to a 15 year old human. Few monkeys live beyond 30 years of age which would correspond roughly to humans over 90 years old.

4.1.2 Area 46 Dorsal Ventral Studies

We performed this study of area 46 of the frontal lobe (see Fig. /refbrainAnatomy) right before the automated methods of ANRA (see Sec. 3) were implemented, so they provide a good stepping stone and comparison for the automated results (Cruz et al., 2009). To locate all of the neurons in every image, a semi-automatic method of neuron detection was first applied (Cruz et al., 2005) to get the majority of the neuronal locations with an accuracy of about 80–85% but with the disadvantage of obtaining about 15–20% false positives. Using an off-the-shelf image editing program, all of these neuronal markings were then manually corrected to eliminate the false positives and to add the missed neurons in every image after which the (x,y) coordinates for detected neurons were recorded. All of these (x,y) coordinates were independently corroborated using our newly developed automated neuron recognition algorithm (ANRA) (A. Inglis and Rosene, 2008).

Brain tissue was obtained from 19 female rhesus monkeys ranging from 6.4 to 32.9 years of age. When comparing means between groups of parameters from our density map analysis we used t-tests with a significance level of $p < 0.05$ two-tailed. Whenever testing for correlations between two sets of parameters we used the more traditional Pearson correlation coefficient as well as the Spearman's rank correlation coefficient. While the Pearson correlation calculations measure linear trends in data, we used the Spearman correlation coefficient to assess how well the relationship between two variables could be related to an arbitrary monotonic function without making any assumptions about the frequency distribution of the variables, i.e. without the assumption that the relationship between the variables is linear or requiring the variables to be measured on interval scales. For these correlation calculations we set the significance level to $p < 0.05$ two-tailed. Throughout this paper, error bars in graphs represent the standard error of the mean. We examined digital images acquired from ROIs from area 46 in the dorsal and ventral banks of sulcus principalis. We note that results from 14 of the 16 monkeys examined for area 46 ventral were studied previously, but only results on microcolumnar strength were reported (Cruz et al., 2004). For behavioral correlations we discarded those cases in which the interval between

Case	Age	Dorsal (N=19)			Ventral (N=16)		
		Number of neurons	Area (microns ²)	Density (neurons/ μm^2)	Number of neurons	Area (microns ²)	Density (neurons/ μm^2)
2	20.4	1274	869,639.06	0.0014650	1272	842,646.74	0.0015095
20	11.8	1168	777,935.94	0.0015014	1076	903,038.94	0.0011915
23	32.3	1108	776,342.97	0.0014272	848	876,961	0.0009670
26	29	1215	769,847.66	0.0015782	1091	813,187.05	0.0013416
41	31.9	1230	760,883.98	0.0016165	1116	880,355.38	0.0012677
65	32.9	1034	772,062.5	0.0013393	963	866,637.05	0.0011112
76	6.4	1061	773,761.33	0.0013712	1414	867,924.48	0.0016292
77	6.4	1039	798,823.44	0.0013007	1080	832,301.1	0.0012976
90	24.9	1845	781,601.56	0.0023605			
96	9	1043	736,386.33	0.0014164	849	868,018.51	0.0009781
97	8.8	983	768,789.06	0.0012786	771	839,924.97	0.0009179
100	24.7	1256	799,665.63	0.0015707	1187	835,582.74	0.0014206
104	28.9	481	367,912.11	0.0013074	951	844,015.43	0.0011268
119	31	1004	780,706.64	0.0012860	1133	866,540.79	0.0013075
125	19.8	1050	766,764.45	0.0013694	686	790,115.63	0.0008682
129	6.7	794	729,950.78	0.0010877	900	800,796.26	0.0011239
130	7.7	1046	775,167.58	0.0013494			
180	29.6	786	769,381.25	0.0010216			
188	6.5	824	723,244.53	0.0011393	701	860,583.14	0.0008146

Figure 4.1: Age, number of neurons, total area, and neuronal density for each of the female monkey brains analyzed.

DNMS data collection and their date of death was greater than 2.5 years, thus reducing some of our data sets when correlating behavior to microcolumnar properties.

In Fig. 4.1 we list the total number of neurons found in all ROIs per monkey, tissue area, and neuronal density for all sections from each of the monkeys analyzed. On average, there were 1,037 neurons found per ROI per monkey over an average tissue area of about 796,786 m^2 per ROI per monkey. When analyzing all the cases as one population, we find that the average density $\langle \rho \rangle = 0.001305 \pm 0.000282 \text{neurons}/\mu\text{m}^2$. When grouping neuronal density by region (dorsal or ventral), the average neuronal density $\langle \rho \rangle = 0.001410 \pm 0.000064 \text{neurons}/\mu\text{m}^2$ in 46 dorsal and $\langle \rho \rangle = 0.001180 \pm 0.000059 \text{neurons}/\mu\text{m}^2$ in 46 ventral (Fig. 4.1). This difference between the densities in the two regions is statistically significant ($p=0.012$). In Fig. 4.3a we show the individual neuronal densities (in units of thousands of neurons per μm^2) as a function age. This graph shows that there is no significant effect of age on neuronal density confirming previous reports that neurons from area 46 are not lost with age (David E. Smith and Tuszynski1, 2004).

Case	Age	Dorsal (N=19)			Ventral (N=16)		
		Number of neurons	Area (microns ²)	Density (neurons/ μm^2)	Number of neurons	Area (microns ²)	Density (neurons/ μm^2)
2	20.4	1274	869,639.06	0.0014650	1272	842,646.74	0.0015095
20	11.8	1168	777,935.94	0.0015014	1076	903,038.94	0.0011915
23	32.3	1108	776,342.97	0.0014272	848	876,961	0.0009670
26	29	1215	769,847.66	0.0015782	1091	813,187.05	0.0013416
41	31.9	1230	760,883.98	0.0016165	1116	880,355.38	0.0012677
65	32.9	1034	772,062.5	0.0013393	963	866,637.05	0.0011112
76	6.4	1061	773,761.33	0.0013712	1414	867,924.48	0.0016292
77	6.4	1039	798,823.44	0.0013007	1080	832,301.1	0.0012976
90	24.9	1845	781,601.56	0.0023605			
96	9	1043	736,386.33	0.0014164	849	868,018.51	0.0009781
97	8.8	983	768,789.06	0.0012786	771	839,924.97	0.0009179
100	24.7	1256	799,665.63	0.0015707	1187	835,582.74	0.0014206
104	28.9	481	367,912.11	0.0013074	951	844,015.43	0.0011268
119	31	1004	780,706.64	0.0012860	1133	866,540.79	0.0013075
125	19.8	1050	766,764.45	0.0013694	686	790,115.63	0.0008682
129	6.7	794	729,950.78	0.0010877	900	800,796.26	0.0011239
130	7.7	1046	775,167.58	0.0013494			
180	29.6	786	769,381.25	0.0010216			
188	6.5	824	723,244.53	0.0011393	701	860,583.14	0.0008146

Figure 4.2: Average values of measures of microcolumnarity

Microcolumnar Measures

The average strength of microcolumns S (ratio of the density of neurons in the microcolumn to the total density of neurons in the ROI) for the whole population is $\bar{S}_i = 1.204 \pm 0.013$. When grouping by region we obtain $\bar{S}_i^D = 1.202 \pm 0.020$ for 46D and $\bar{S}_i^V = 1.207 \pm 0.018$ for 46V with no statistically significant difference between the two areas. Figure 5 shows S per region vs age and documents a significant age-related reduction in S as a function of age in both, area 46D and 46V (Pearson and Spearman correlation coefficients are listed in Table 3 in the S vs age row). These data confirm our previous findings on some of the same subjects for 46V (Cruz et al., 2004) and extend the observation of an age-related alteration in microcolumnar strength to the larger cohort in 46V as well as to 46D. The other measures of microcolumnar organization derived from the density map do not show significant changes with age. In particular, Figure 4(b) shows the microcolumnar width W . The population average is $\bar{W}_i = 12.303 \pm 0.552$ m with region averages $\bar{W}_i^D = 12.592 \pm 0.873$ m and $\bar{W}_i^V = 11.959 \pm 0.641$ m which are not significantly different. This figure also shows that there is no significant relationship of microcolumnar width with age. The

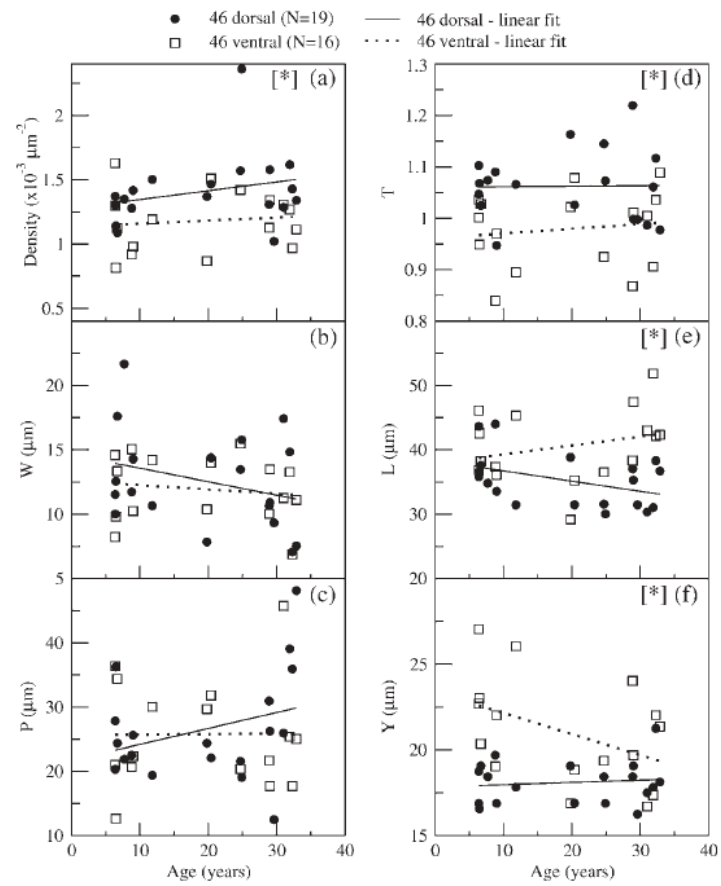


Figure 4.3: Microcolumnar relationships in area 46 of the female monkey

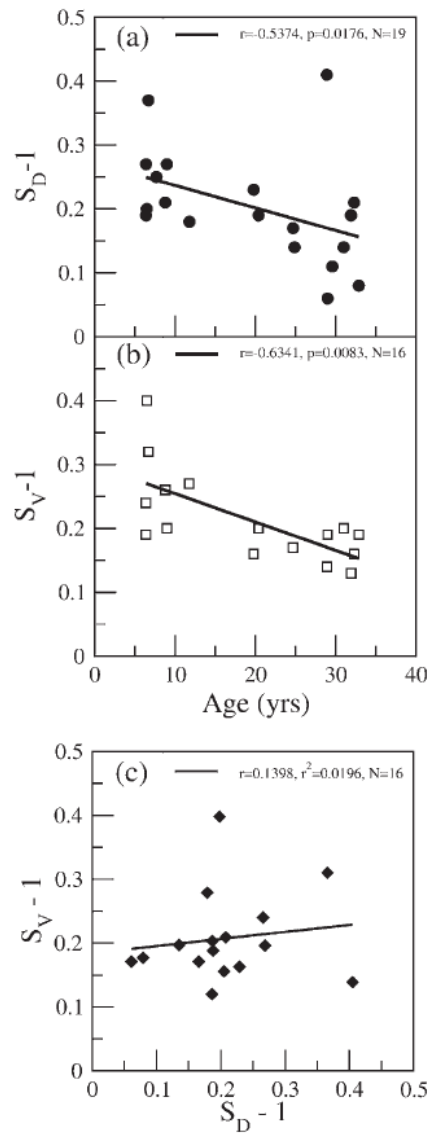


Figure 4.4: Microcolumnar strength per case for (a) dorsal SD (N=19) and (b) ventral SV areas (N=16). In both areas the microcolumnar strength decays with age where the correlations are significant. The values of strength are plotted subtracting 1 (S-1) to indicate that a zero value of S corresponds by definition to a lack of microcolumnar organization. The lines are regression (best fit) lines. (c) Plot of S_V vs. S_D to determine possible correlations between microcolumnar strength from both areas. The small value for the correlation coefficient indicates a lack of correlations between these two quantities.

distance between microcolumns P has a population average of $\bar{P}_i = 26.188 \pm 1.400$ m. When comparing this by region we found that on average $\bar{P}_iD = 26.52 \pm 1.92$ m and $\bar{P}_iV = 25.79 \pm 2.11$ m, which is not significantly different. Moreover, like W, there is no significant change in the distance between microcolumns with age as shown in Fig. 4.3c.

Fig. 4.3d and e shows the degree of microcolumnar periodicity T and length L. Both differences in T and in L per region are significant ($P=0.002$ for T; $P=0.004$ for L). However, similar to W and P, no significant age-related changes in either of these parameters with age are detected.

The population average for the vertical distance between neurons within a microcolumn Y (i.e. neuron-neuron distance along the microcolumn) is $\bar{Y}_i = 19.43 \pm 0.45$ m. Grouping by region the average Y are $\bar{Y}_iD = 18.09 \pm 0.29$ m and $\bar{Y}_iV = 21.03 \pm 0.77$ m, which are significantly different ($p=0.002$). However, when plotted as a function of age, Y does not show any significant age-related change (Fig. 4.3f). In summary, areas 46 dorsal and ventral show some similarities in the values for P and W but some distinct differences in the values for T and L, Y, and neuronal density, listed in Fig. 4.2. These two areas are also similar in their values for S as well as showing similar age-related reductions in S, the strength of the microcolumn.

The average strength of microcolumns S (ratio of the density of neurons in the microcolumn to the total density of neurons in the ROI) for the whole population is 1.204 ± 0.013 . When grouping by region we obtain 1.202 ± 0.020 for 46D and 1.207 ± 0.018 for 46V with no statistically significant difference between the two areas. Fig. 4.4a and b shows S per region vs. age and documents a significant age-related reduction in S as a function of age in both area 46D and 46V (we plot $S-1$ instead of S to obtain a quantity that is zero when there is no microcolumnarity). These data confirm our previous findings based on some of the same subjects for 46V (Cruz et al., 2004) and extend the observation of an age-related alteration in microcolumnar strength to the larger cohort in 46V as well as to 46D.

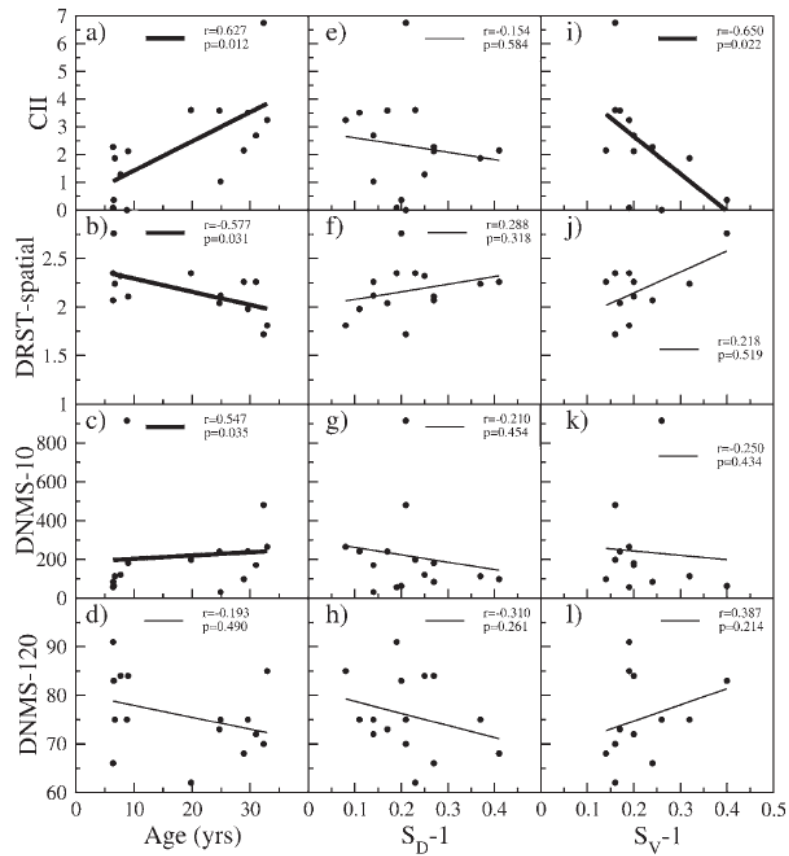


Figure 4.5: Plots of cognitive tests vs. age, SD, and SV. The tests include a global CII, a spatial working memory span task (DRST-spatial), the acquisition at a 10 s delay of the DNMS-10, and recognition memory performance of DNMS-120. Plots showing significant correlations are marked with thick linear ts. For the monkeys from our cohort, only (a) CII, (b) DRST-spatial, and (c) DNMS-10 correlate with age. Correlations between behavior and S show that CII correlates with SV (i).

Relationship to behavior

All of the behavioral tests considered in this paper are sensitive to age-related cognitive impairments (Herndon JG and RJ, 1997). In our cohort of monkeys, however, only three behavioral tests show a significant change with age: (i) the CII (Fig. ??a), (ii) a spatial working memory span task, DRST spatial (Fig. 4.5b), and (iii) the acquisition at a 10 s delay of the DNMS test, DNMS-10 (Fig. 4.5c). The acquisition at a 2 min delay of the DNMS test, DNMS-120 (Fig. 4.5d) does not show changes with age in our cohort. In Fig. 4.5e to l we show all of the cognitive tests versus SD and SV. These plots show that there is no significant relationship between any of the tests and SD. We also observe that the CII significantly correlates with SV.

Summary of study

In this study we use the density map method to quantify the changing structure of microcolumns in two distinct parts of area 46 the dorsal and ventral banks of the middle level of sulcus principalis of the prefrontal cortex in behaviorally characterized aging female monkeys. This quantitative analysis demonstrates that while many microcolumnar properties are similar between area 46 in the dorsal and ventral banks, there are differences in others. Moreover, while there are age-related effects in both areas, only the changes in ventral area 46 show a relationship with aging.

We notice in the study that there are many correlative analysis of spatial measurements of the tissue. This will be a theme of the analysis for the rest of the studies, however, we will now start to use ANRA which will allow us to gather more statistics to perform the correlations.

4.1.3 Area TE Studies

We performed this study of area TE of the temporal lobe (see Fig. /refbrainAnatomy) using the automated methods of ANRA. Because the quick montaging was not online yet, the number of cells and subjects used was not significantly greater than the previous study.

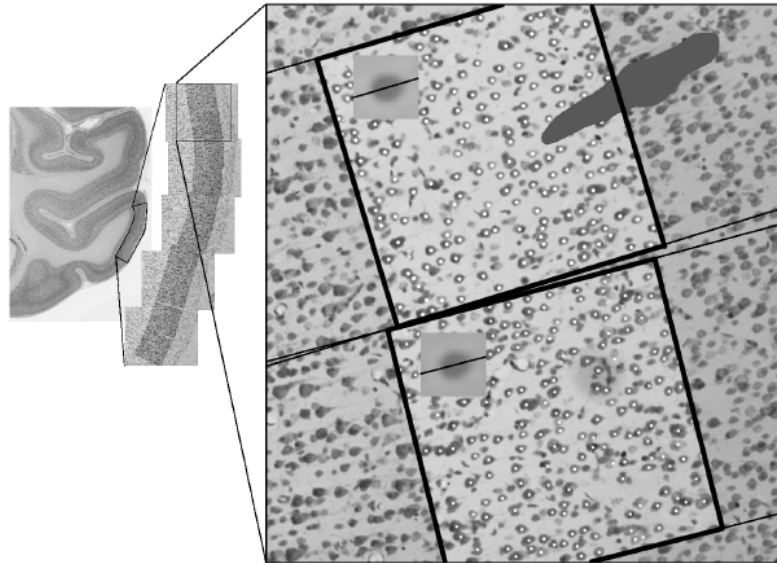


Figure 4.6: Two separate 512x512 analysis windows (150 neurons) are extracted from each of the 5 photomicrographs from two slides for a total of 20 512x512 windows and a total of 3000 neuron locations per subject . The windows are rotated such that they align with the average dendrite direction in layer III, as determined by an average of an overlay of the identified neurons (inset). Gray area shows where the image was masked and not analyzed due to a blood vessel intrusion. The human capital for the analysis window selection process is 1 window per 10 seconds.

What we attempt to do is replicate the same type of study that was performed with manual recognition (see Sec. ??, only replacing the step of finding cell locations from manual to automatic.

Fig. 4.6 shows the method of stitching together results along the temporal lobe section of the brain. Fig. 4.7 shows the raw data, similar to the 46dv study with several more cases (22 vs 17) and more neurons (3000 vs 1200).

We note from Fig. 4.7 that area TE has a statistically significantly higher overall density everywhere, including inside the microcolumn S_{num} , and even after normalization with ρ , still has a higher ratio of neurons inside of the microcolumn (S). When looking at the relationship of microcolumnar strength with age, we see another trend: We find that in the

Case (id#)	Age (years)	CII	Number of Neurons	Area (mm ²)	Density (neurons/ μm^2)
065	32.9	3.24	3046	1.90	0.00160
066	11.2	---	3313	1.94	0.00171
077	6.4	2.27	3364	1.84	0.00183
096	9.0	2.12	2514	1.60	0.00157
097	8.8	0.00	2877	1.73	0.00166
100	24.7	3.59	2971	1.62	0.00184
104	28.9	2.15	2797	1.85	0.00151
119	31.0	2.69	3076	1.99	0.00155
125	19.8	3.61	3500	2.00	0.00175
129	6.7	1.87	2424	1.58	0.00153
130	7.7	1.28	2605	1.68	0.00155
149	19.8	0.34	2488	1.99	0.00125
161	19.2	1.88	2582	1.58	0.00163
162	22.3	2.32	3019	1.75	0.00173
179	23.6	6.99	3403	1.85	0.00184
180	29.6	3.51	3660	1.84	0.00199
190	18.0	1.79	3004	1.76	0.00171
194	11.9	2.26	3084	1.91	0.00161
199	10.6	1.61	3120	1.85	0.00169
202	10.3	0.08	3135	1.86	0.00169

Figure 4.7: Age, number of neurons, total area, and neuronal density for each of the female monkey brains analyzed.

	TE3	46D	46V
age	17.62 \pm 8.81	19.41 \pm 10.71	19.16 \pm 10.94
CII	2.29 \pm 1.57	2.30 \pm 1.74	2.39 \pm 1.87
$\rho \times 10^{-3}$	1.66 \pm 1.56	1.41 \pm 2.79	1.17 \pm 2.36
S	1.26 \pm 0.06	1.20 \pm 0.09	1.21 \pm 0.07
$S_{\text{num}} \times 10^{-3}$	2.09 \pm 1.80	1.69 \pm 3.09	1.42 \pm 2.70
T	1.04 \pm 0.04	1.06 \pm 0.07	0.98 \pm 0.07
$T_{\text{num}} \times 10^{-3}$	1.73 \pm 1.53	1.50 \pm 3.20	1.15 \pm 2.65
W	14.57 \pm 2.16	12.60 \pm 3.81	12.12 \pm 2.66
P	24.50 \pm 6.30	26.53 \pm 8.38	25.29 \pm 9.27
L	34.66 \pm 3.15	34.93 \pm 4.34	41.45 \pm 7.38
Y	18.44 \pm 1.64	18.09 \pm 1.25	20.95 \pm 2.97

Figure 4.8: Microcolumnar relationships in area TE of the female monkey, compared with 46dv

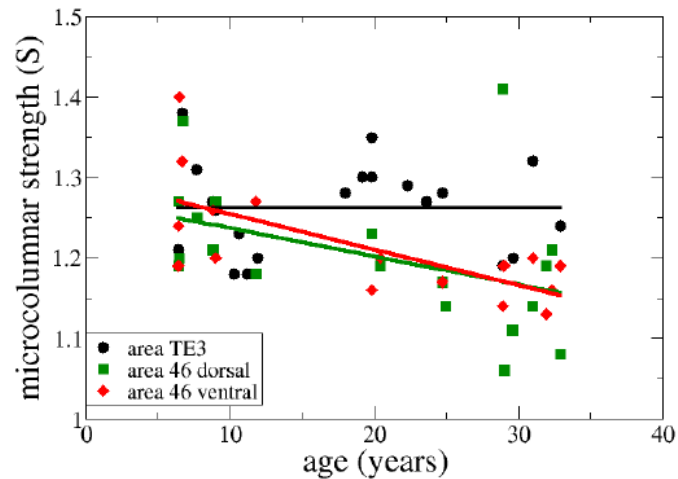


Figure 4.9: Microcolumnarity of TE vs age, compared with 46dv

early years, microcolumnar strength is at the same level in all 3 areas. Then through middle age to aging, while S decreases in area 46, it remains constant in TE3. We also find no correlations of microcolumnar properties with cognitive ability. We hypothesize that this lack in changes within spatial arrangement is due to a non-deteriorating set of functions that are performed in area TE (visual recognition tasks) compared with that of area 46 dorsal and ventral (attention and working memory).

4.1.4 Area TE Comparison with model

Because of the heightened level of statistics that were obtained with area TE from the automated method, we explored the trends that were found between microcolumnar properties with the dataset. We used the model developed by Cruz et al. and briefly discuss it here.

Microcolumnar modelling

We develop a relationship between these 2D density maps and the actual 3D properties of microcolumns by creating a theoretical 3D model of cortical neurons. In seven steps, we transform a 3D initial arrangement of neurons from a crystalline lattice, with distances and neuron numbers approximating the idealized cortical microcolumn as assayed by our

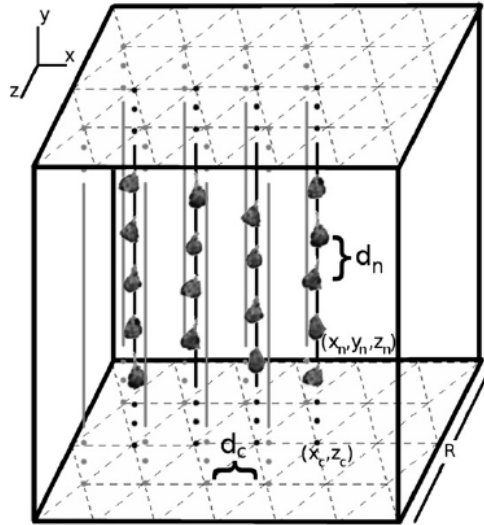


Figure 4.10: The dotted lines form the hexagonal lattice on which microcolumns are initially positioned. The neuronal bodies used in the diagram only serve for illustration purposes, as in the model each neuron is represented by a sphere with the radius

2D density map analysis, into a model whose neuronal locations represent a plausible 3D arrangement of neurons in the brain. Because we constrain the transformations on the 3D model by the 2D density map properties, the transformed 3D model will exhibit properties that are consistent with experimental findings regarding microcolumnar anatomy in the brain. Moreover, because our methodology only requires the x, y locations of neurons from thin sections, it is readily accessible to any set of input data regardless of preparation or staining, from human or animals. By generating 3D model neuronal arrangements and comparing between control, aged, and diseased brain, our method can be used to test hypotheses about the effects of neurological diseases as well as normal aging on the 3D structure of microcolumns in the brain.

A prerequisite for the method presented here is the knowledge of the measures of microcolumnarity of the system for which the 3D model of neurons will be constructed. We define these measures as the “target” (experimental) measures. The method then starts with a theoretical arrangement of neurons in 3D initially arranged in a crystalline lattice based

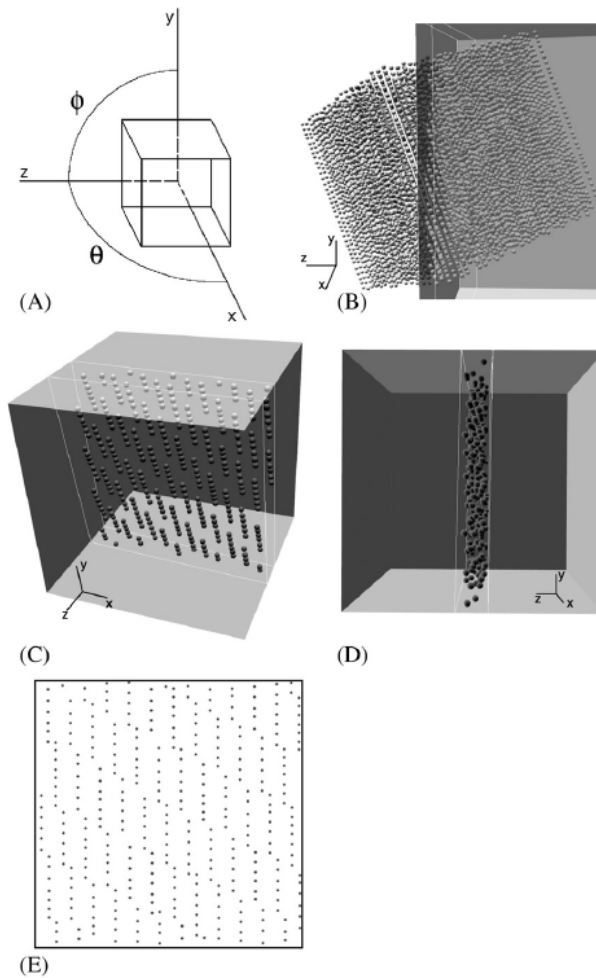


Figure 4.11: (A) shows the axis and angles of rotation in relation to the 3D block of neurons indicated by the cubic wire box. (B) shows a rotated example of a 3D block of neurons where the neurons within the slab indicated by the thin lines are cut in (C) and (D). (E) shows the neurons from (D) collapsed into the xy plane that is used to calculate the density maps. For visual clarity, the example shown is generated using only half of the steps to recreate the biological variance within the model of points.

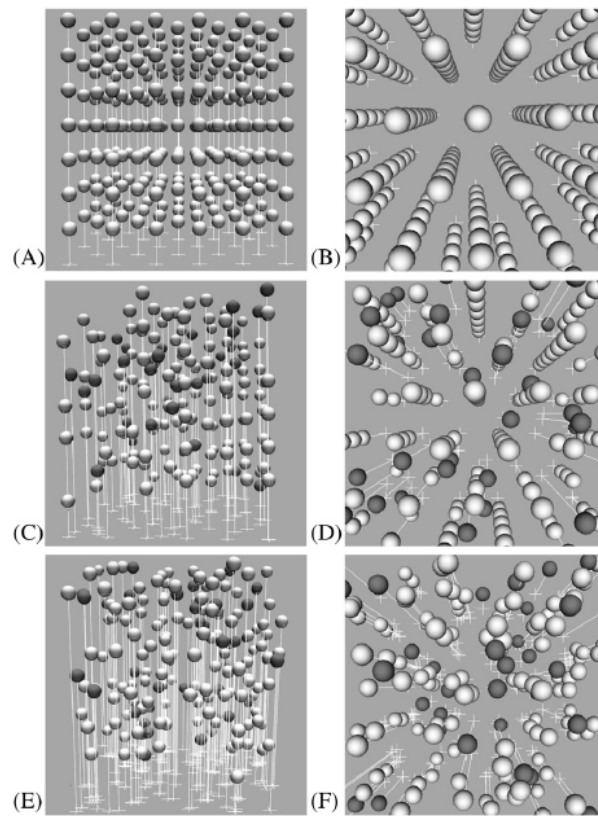


Figure 4.12: Configurations at step 0 (A and B), at step 3 (C and D), and at step 6 (E and F). The darker spheres are interneurons. Each neuron has a vertical thin line whose base in the xz plane is indicated by a thin cross.

on morphological data where neurons are individually and progressively adjusted over the course of six remaining steps to produce a 3D model that best fits the target measures. Each step is designed to affect at least one of the measures while producing only minor changes to the other measures. After each step, we monitor the effect of that change on all of the measures of microcolumnarity of the model and adjust the magnitude of the change to match the measure from the 3D model to the target value. In general, each step consists of (i) generating N 3D blocks of neurons modified by the number of steps under scrutiny (each block is denoted as one “realization”), (ii) “cutting” one thin slice through each transformed model block (to obtain N slices) at a random orientation and inclination to generate a set of 2D “sections”, (iii) applying the density map analysis to those N sections to derive one set of microcolumnar measures corresponding to that step, and (iv) comparing the microcolumnar measures from the model to the target experimental measures.

We apply the model to the analysis of the real data in the following way. First, we noticed trends in some of the microcolumnar properties with respect to each other and with density (Fig. 4.13). We attempt to recreate similar behaviors in microcolumnar properties based on changing some of the variables of the model, such as inter columnar spacing, interneuron percentage, and angle of cut. We observe a change in density relating to microcolumnar properties in the tissue, so we test two possible mechanisms for this relationship: an increasing number of interneurons, or a decreasing in the space between columns. Running the two models, we note that the latter recreates all of the trends seen in the tissue (Fig. 4.14), whereas the former doesn’t (not shown).

As a conclusion to this section, we have performed three validations to the use of ANRA: first, the recognition rates of 95% and 5% false positive (Sec. 3.3) for most tissue and staining procedures studied, a comparison with stereological numbers showing numbers obtained from ANRA are within natural variance levels of stereological numbers (Sec. 3.6) and lastly an analysis run that shows results from an unmeasured brain region, area TE. Further validation will come from continued use, and duplication of previous studies that used manual methods.

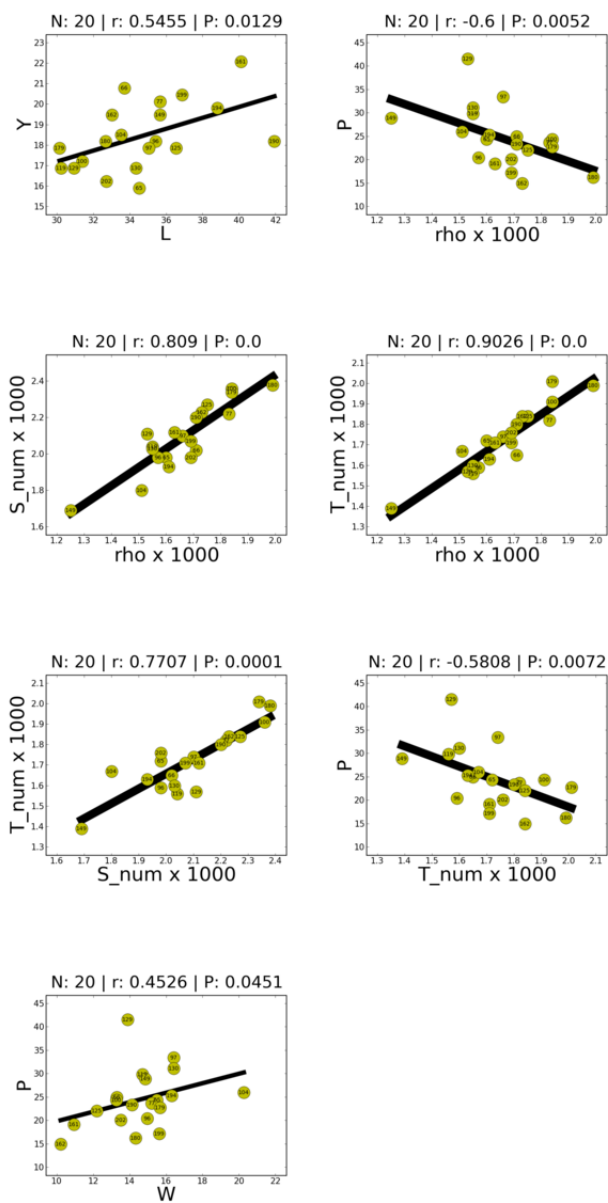


Figure 4.13: Correlations of microcolumnar properties with each other and density

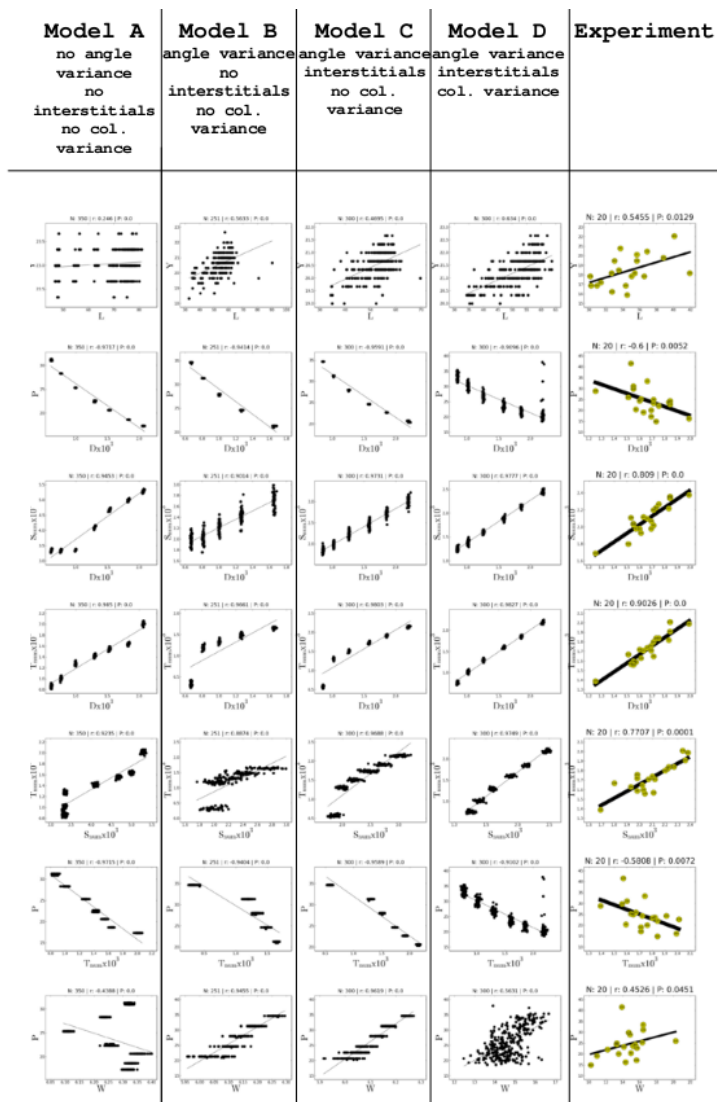


Figure 4.14: Model generation to align with features of area TE

4.2 Rat Tissue

The utility of these measures to the study of the rat brain has been explored over the last year. We adapted applied the methods described above to quantify columnar organization in rat cortex using digitized images captured with the DMetrix DX-40 scanning array microscope. This instrument contains 80 miniaturized 20X objectives and can image 40 slides per hour, a hundredfold increase in rate of image acquisition compared to other commercial solutions. This increase in digitization speed, when coupled with computing systems able to store and automatically analyze terabytes of image data, removes the restriction of focusing on a limited cortical region such as area 46 and allows assessment of the entire rat neocortex. Initial results demonstrate 95% accuracy for recognition of both neurons and glial cells when applying ANRA to the DMetrix images. We attribute the high level of recognition, even with a single colored stain to the more discernable differences between neuron and glial cells in the rat tissue. Applying density map analysis to Nissl-stained sections of adult Fischer-344 rat somatosensory cortex revealed a microcolumnar strength of 1.10, exceeding a value of 1.00 which indicates a non-columnar, uniform distribution. These data provide evidence for an identifiable, statistical tendency among neurons to be organized into microcolumns in rat neocortex. Extension of these methods to compare the cortex of young and old rats will allow determination of whether rat cortex shows age-related changes in microcolumns and if there is region selective vulnerability.

Because of the fast digitization of the tissue, we have been able to apply ANRA to locate neurons and glial in entire rat brains (see Fig. 4.15). In the beginning analysis, we are investigating the differences in layers of the cortex, as preliminary studies have shown that microcolumn properties do not change drastically through the somatosensory and motor cortex (not the case in monkeys). A preliminary result using the number of points needed to have less than 1% statistical error to show differences in microcolumnar features that are near to this 1% difference (about 50,000 points, See Sec. 2.3.1) in fact shows such small differences in the microcolumnar structure, thereby showing a strong result dependant on

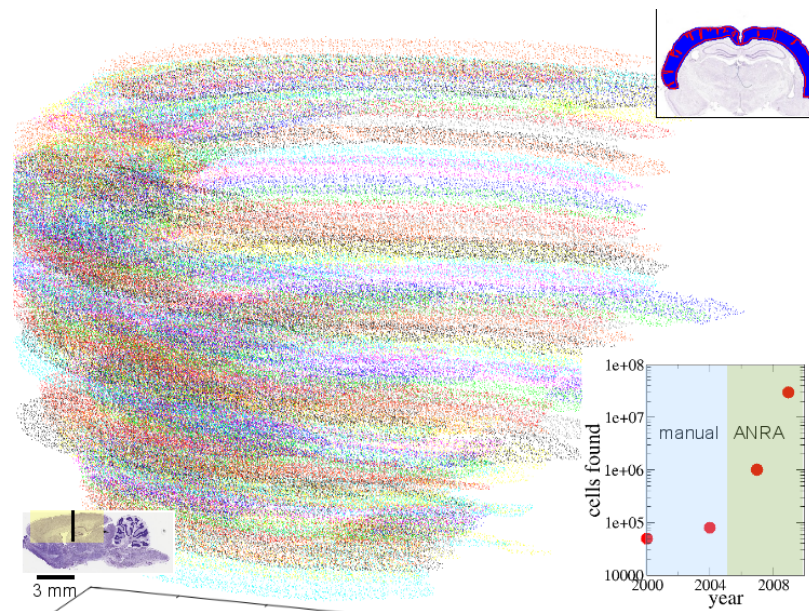


Figure 4.15: (center) depiction of the 5 million cell bodies that are recognized by ANRA in a single rat cortex. The colors represent different $30\mu m$ layers (upper right) $300\mu m$ apart. Every 10th location is plotted to show structure. (lower left) shows the saggital (side) view of the slices (black line) through the cortex (yellow highlight). (lower right) plot showing the number of cells located to date with manual methods in our lab (blue), and ANRA (green).

the large numbers obtained by automated methods, and at the same time casting doubt on being able to scan smaller regions for heterogeneous changes.

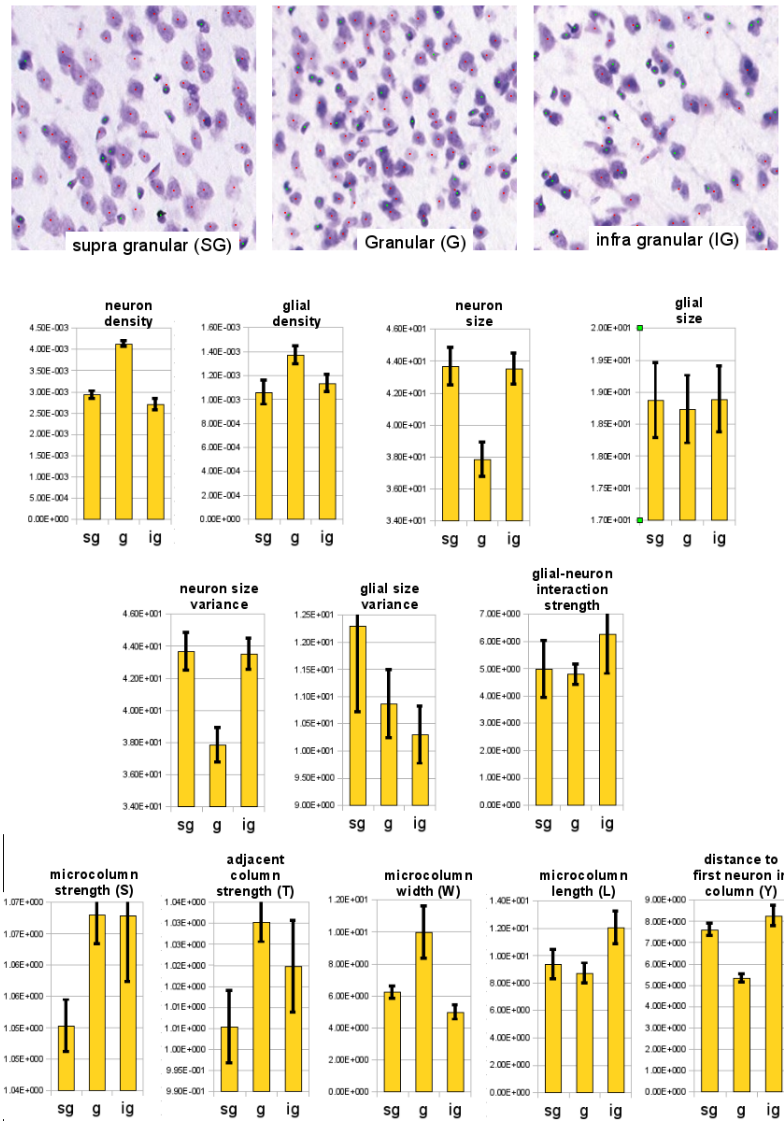


Figure 4.16: (top) Sample image of supra granular (SG), granular (G), and infragranular (IG) tissue with located glial cells (green) and neurons (red) in somatosensory and motor cortex of young rats. The probe was selected to three layer groupings. Both somatosensory and motor cortex were used for the SG and IG layers, and the granular layer was only in the somatosensory area. Roughly 35000 neuron cells per probe measurement were used in the analysis, and roughly 15,000 glial cells. the glial cells were not used in the microcolumnar property measurements, but were used in the radial neuron-glial attachment measurement.

Appendices

Bibliography

- L. Cruz D. Roe H. E. Stanley A. Inglis, B. Urbanc and D. Rosene. Automated identification of neurons and their locations. 230:339–352, 2008.
- M. Abeles. *Corticonics: Neural circuits of the cerebral cortex*. Cambridge University Press, 1991.
- D. Aha, D. & Kibler. Instance-based learning algorithms. 6:37–66, 1991.
- Lewis DA Anderson SA, Volk DW. Increased density of microtubule associated protein 2- immunoreactive neurons in the prefrontal white matter of schizophrenic subjects. 19: 111–119, 1996.
- E. Asare. Neuronal pattern correlates with the severity of human immunodeficiency virus-associated dementia complex. *American Journal of Pathology*, 148:31–36, 1996.
- A. Benali, I. Leefken, U. F. Eysel, and E. Weiler. A computerized image analysis system for quantitative analysis of cells in histological brain sections. *Journal of Neuroscience Methods*, 125:33–43, 2003.
- F. M. Benes and E. D. Bird. An analysis of the arrangement of neurons in the cingulate cortex of schizophrenic patients. *Archives of General Psychiatry*, 44(7):608–616, 1987.
- Paola Bezzi and Andrea Volterra. A neuron-glia signalling network in the active brain. 11: 387–394, 2001.
- A. Blake and M. Isard. *Active Contours*. Springer, London, 1998.

- V. Braitenberg and A. Shu uz. *Cortex: statistics and geometry of neuronal connectivity*. Springer.
- S. V. Buldyrev, L. Cruz, T. Gomez-Isla, E. Gomez-Tortosa, S. Havlin, R. Le, H. E. Stanley, B. Urbanc, and B. T. Hyman. Description of microcolumnar ensembles in association cortex and their disruption in alzheimer and lewy body dementias. *pnas*, 97:5039–5043, 2000.
- D. Buxhoeveden and W. Lefkowitz. The linear organization of cell columns in human and non-human anthropoid tpt cortex. *Anat. Embryol.*, 194:23–36, 1996.
- Daniel Buxhoeveden, Emil Roy, Andrew Switala, and Manuel F. Casanova. Reduced interneuronal space in schizophrenia. *Biol Psychiatry*, 47:681–682, 2000.
- Daniel P. Buxhoeveden and Manuel F. Casanova. Minicolumn hypothesis in neuroscience, the. *Brain*, 125:935–951, 2002.
- Daniel P. Buxhoeveden, Ulla Hasselrot, Nicole E. Buxhoeveden, Rosemarie M. Booze, and Charles F. Mactutus. Microanatomy in 21 day rat brains exposed prenatally to cocaine. *International Journal of Developmental Neuroscience*, 24(5):335–341, 2006.
- M. F. Casanova, A. E. Switala, and J. Trippe. A comparison study of the vertical bias of pyramidal cells in the hippocampus and neocortex. *Developmental Neuroscience*, 29:193–200, 2006.
- Manuel F. Casanova. Preservation of hippocampal pyramidal cells in paraphrenia. *Schizophrenia Research*, 62((1-2)):141–146, 2003.
- Manuel F. Casanova, Daniel P. Buxhoeveden, Andrew E. Switala, and Emil Roy. Minicolumnar pathology in autism. *Neurology*, 58(3):428–432, 2002.
- Switala AE Crow TJ Chance SA, Casanova MF and Esiri MM. Minicolumn thinning in temporal lobe association cortex but not primary auditory cortex in normal human ageing. 111(5):459–464, 2006.

- Vanhoutte P. Pags C. Borrelli E. Charvin, D. and J. Caboche. Unraveling a role for dopamine in huntington's disease: The dual role of reactive oxygen species and d2 receptor stimulation. *102(34):12218–12223*, 2005.
- L. Costa and E. Bollt. A fast and accurate nonlinear spectral method for image recognition and registration. *Applied Physics Letters*, 89:174102, 2006.
- D. Cremers, C. Schnorr, J. Weikert, and C. Shelleward. Diffusion-snakes using statistical shape knowledge. In G. Sommer and Y.Y.Zeevi, editors, *Algebraic Frames for the Perception-Action Cycle, Lecture Notes in Computer Science*, volume 1888, pages 164–174. Springer, 2000.
- L. Cruz, S. Buldyrev, S. Peng, D. Roe, B. Urbanc, and H.E. Stanley. A statistically based density map method for identification and quantification of regional differences in microcolumnarity in the monkey brain. *Journal of Neuroscience Methods*, 141:321–332, 2005.
- L. Cruz, D. L. Roe, B. Urbanc, H. Cabral, H. E. Stanley, and D. L. Rosene. Age-related reduction in microcolumnar structure in area 46 of the rhesus monkey correlates with behavioral decline. *pnas*, 101:15846–15851, 2004.
- L. Cruz, D. L. Roe, B. Urbanc, A. Inglis, H. E. Stanley, and D. L. Rosene. Age-related reduction in microcolumnar structure correlates with cognitive decline in ventral but not dorsal area 46 of the rhesus monkey. *Neuroscience*, 158:1509–1520, 2009.
- L. Cruz, B. Urbanc, A.Inglis, H. E. Stanley, and D. L. Rosene. Generating a model of the three-dimensional spatial distribution of neurons using density maps. *Neuroimage*.
- D. R. Riddle D. Purves and A-S. LaMantia. Iterated patterns of brain circuitry (or how the cortex gets its spots). *Trends in Neurosciences*, 15(10):362–368, 1992.
- Friedman S.D. Parow A. Demopoulos C. Stoll A. L. Lyoo I.K. Dunner D. L. Renshaw P.F.

- Dager, S.R. Brain metabolic alterations in medication-free patients with bipolar disorder. *jnm*(61):450–458, 2004.
- Heather M. McKay Jeffrey A. Roberts David E. Smith, Peter R. Rapp and Mark H. Tuszynski. Memory impairment in aged primates is associated with focal death of cortical neurons and atrophy of subcortical neurons. *24*(18):4373–4381, 2004.
- R. Duda, R. Hart, and D. Stork. *Pattern Classification*. John Wiley and Sons, 2001.
- C. Duyckaerts and G. Godefroy. Voronoi tessellation to study the numerical density and the spatial distribution of neurons. *Journal of Chemical Neuroanatomy*, 20:83–92, 2000.
- Jones EG. Microcolumns in the cerebral cortex. *97*(10):5019–5021, 2000.
- I. Feinberg. Schizophrenia: caused by a fault in programmed synaptic elimination during adolescence? *17*(4):319–334, 1982.
- RD Fields and Stevens-Graham. New insights into neuron-glia communication. *298*(5593):556–562, 2002.
- Henry Gray. *Anatomy of the Human Body*. Lea and Febiger, 1918.
- Rosene DL Herndon JG, Moss MB and Killiany RJ. Patterns of cognitive decline in aged rhesus monkeys. *87*:25–34, 1997.
- M. Hildebrandt, T. Pieper, P. Winkler, D. Kolodziejczyk, H. Holthausen, and I. Blümcke. Neuropathological spectrum of cortical dysplasia in children with severe focal epilepsies. *110*:111, 2005.
- P. R. Hof, V. Haroutunian, V. L. Friedrich, Jr., W. Byne, C. Buitron, D. P. Perl, , and K. L. Davis. Loss and altered spatial distribution of oligodendrocytes in the superior frontal gyrus in schizophrenia. *Biological Psychiatry*, 53:1075–1085, 2003.
- R. Holte. Very simple classification rules perform well on most commonly used datasets. *11*:63–91, 1993.

- Wiesel TN Hubel DH. Shape and arrangement of columns in cat's striate cortex. 165: 559–68, 1963.
- Wiesel TN Hubel DH. Functional architecture of macaque visual cortex. 198:1–59, 1977.
- B. Javi. *Image recognition and classification : algorithms, systems, and applications*. Marcel Dekker, 2002.
- P. John, G. H. & Langley. Estimating continuous distributions in Bayesian classifiers. pages 338–345. Proceedings of the Eleventh Conference on Uncertainty in Artificial Intelligence, 1995.
- Byne W Jones LB, Johnson N. Alterations in map2 immunocytochemistry in areas 9 and 32 of schizophrenic prefrontal cortex. 114:137–148, 2002.
- R. A. Krasnoperov and D. Stoyan. Second-order stereology of spatial fibre systems. *Journal of Microscopy*, 216:156–164, 2004.
- Audie G. Leventhal, Yongchang Wang, Mingliang Pu, Yifeng Zhou, and Yuanye Ma. Gaba and its agonists improved visual cortical function in senescent monkeys. *Science*, 300 (5620):812–815, 2003.
- G. Lin, M. K. Chawla, K. Olson, J. Guzowski, C. Barnes, and B. Roysam. Hierarchical, model-based merging of multiple fragments for improved three-dimensional segmentation of nuclei. *Cytometry*, 63A:20–33, 2005.
- X. Long, W. L. Cleveland, and Y. L. Yao. A new preprocessing approach for cell recognition. *IEEE Transactions on Information Technology in Biomedicine*, 9:407–412, 2005.
- X. Long, W. L. Clevelandb, and Y. L. Yao. Automatic detection of unstained viable cells in bright field images using a support vector machine with an improved training procedure. *Computers in Biology and Medicine*, 36:339–362, 2006.
- T. M. Mayhew. A review of recent advances in stereology for quantifying neural structure. *Journal of Neurocytology*, 21:313–328, 1991.

- Marshall N. Sham P.C. Bullmore E.T. Schulze K. Chapple B. Bramon E. Filbey F. Quraishi S. Walshe M. McDonald, C. and R.M. Murray. Regional brain morphometry in patients with schizophrenia or bipolar disorder and their unaffected relatives. 163:478–487, 2004.
- Poline J-B Kohn P.D. Holt J.L. Egan M.F. Weinberger D.R. Meyer-Lindenberg, A. and K.F. Berman. Evidence for abnormal cortical functional connectivity during working memory in schizophrenia. 158:1809–1817, 2001.
- Schettler S.P. Killiany-R.J. Herndon J.G. Luebke J.I. Moss M.B. Moore, T.L. and D.L. Rosene. Cognitive impairment in aged rhesus monkeys associated with monoamine receptors in the prefrontal cortex. 160(2):208–221, 2005.
- VB. Mountcastle. Modality and topographic properties of single neurons of cats somatic sensory cortex. 20:408–434, 1957.
- VB. Mountcastle. The columnar organization of the neocortex. 120:701–722, 1997.
- VB. Mountcastle. Untitled - introduction. 13(1):2–4, 2003.
- D. Mumford and J. Shah. Optimal approximation by piecewise smooth functions and associated variational problems. *Communications on Pure Applied Mathematics*, 42:577–685, 1989.
- T. W. Nattkemper, H. J. Ritter, and W. Schubert. A neural classifier enabling high-throughput topological analysis of lymphocytes in tissue sections. *IEEE Transactions on Information Technology in Biomedicine*, 5:138–149, 2001.
- S. Peng, B. Urbanc, L. Cruz, B. T. Hyman, and H. E. Stanley. Neuron recognition by parallel pots segmentation. *pnas*, 100:3847–3852, 2003.
- A. Peters and D. L. Rosene. In aging, is it gray or white?, *journal of comparative neurology*. 462(2):139–143, 2003.
- A. Peters and C. Sethares. Organization of pyramidal neurons in area-17 of monkey visual-cortex. *Journal of Comparative Neurology*, 306(1):1–23, 1991.

- Morrison JH, Rosene-DL, Peters, A and BT Hyman. Are neurons lost from the primate cerebral cortex during normal aging? 8:295–300, 1998.
- J. Platt. *Advances in Kernel Methods - Support Vector Learning*. MIT Press, 1998.
- R. Quinlan. *C4.5: Programs for Machine Learning*. Morgan Kaufmann Publishers, 1993.
- N. Ray, S. T. Acton, and K. Ley. Tracking leukocytes in vivo with shape and size constrained active contours. *IEEE Transactions on Medical Imaging*, 21:1222–1234, 2002.
- C. H. Rickert. Cortical dysplasia: neuropathological aspects. 22(8):821–826, 2006.
- C. Di Rocco and G. Tamburrini. Surgical treatment of epilepsy in children. 22(8):743, 2005.
- D.L. Roe. From dopa to parkinsons disease: The early history of dopamine research. 6(3): 291–301, 1997.
- J. Stone S. Mikula, I. Trotts and E. G. Jones. Internet-enabled high-resolution brain mapping and virtual microscopy. 35(1):9–15, 2007.
- K. S. Saleem, K. Tanaka, and K. S. Rockland. Specific and columnar projection from area teo to te in the macaque inferotemporal cortex. *Cerebral Cortex*, 3(5):454–464, 1993.
- C. Schmitz, N. Grolmes, P. R. Hof, R. Boehringer, J. Glaser, and H. Korr. Altered spatial arrangement of layer v pyramidal cells in the mouse brain following prenatal low-dose x-irradiation. a stereological study using a novel three-dimensional analysis method to estimate the nearest neighbor distance distributions of cells in thick sections. *Cerebral Cortex*, 12:954–960, 2002.
- C. Schmitz and P. R. Hof. Designed-based stereology in neuroscience. *Neuroscience*, 130: 813–831, 2005.
- Matthew T. Schmolesky, Youngchang Wang, Mingliang Pu, and Audie G. Leventhal. Degradation of stimulus selectivity of visual cortical cells in senescent rhesus monkeys. *Nature Neuroscience*, 3(4):384–390, 2000.

- P. J. Sjöström, B. R. Frydel, and L. U. Wahlberg. Artificial neural network-aided image analysis system for cell counting. *Cytometry*, 36:18–26, 1999.
- D. Slater, G. Healey, P. Sheu, C. W. Cotman, J. Su, A. Wasserman, and R. Shankle. A machine vision system for the automated classification and counting of neurons in 3-d brain tissue samples. In *IEEE Workshop on Applications of Computer Vision (WACV)*, Washington, DC, USA, 1996. IEEE Computer Society.
- N. V. Swindale. Is the cerebral cortex modular? *Trends in Neurosciences*, 13(12):487–492, 1990.
- M. S. Todtenkopf, S. L. Vincent, and F. M. Benes. A cross-study meta-analysis and three-dimensional comparison of cell countin in the anterior cingulate cortex of schizpphtronic and bipolar brain. *Schizpphrenia Research*, 73:79–89, 2005.
- M. Tommerdahl, O. Favorov, B. L. Whitsel, B. Nakhle, and Y. A. Gonchar. Minicolumnar activation patterns in cat and monkey si cortex. *Cerebral Cortex*, 3(5):399–411, 1993.
- Colwyn Trevarthen. brain development. from www.answers.com/topic/brain-development, 2004.
- M. Tscherepanow, F. Zöllner, and F. Kummert. Classification of segmented regions in brightfield microscope images. In *Proceedings of the 18th International Conference on Pattern Recognition*, Washington, DC, USA, 2006. IEEE Computer Society.
- B. Urbanc, L. Cruz, R. Le, J. Sanders, K. Hsiao-Ashe, K. Duff, H.E. Stanley, M. C. Irrizarry, and B. T. Hyman. Neurotoxic effects of thioflavin s-positive amyloid deposits in transgenic mice and alzheimers disease. *pnas*, 97:13990–13995, 2002.
- G. W. VanHoesen and A. Solodkin. Some modular features of temporal cortex in humans as revealed by pathological-changes in alzheimers-disease. *Cerebral Cortex*, 3(5):465–475, 1993.

- Alessandro E. Vercelli, Diego Garbossa, Roberta Curtetti, and Giorgio M. Innocenti. Somatodendritic minicolumns of output neurons in the rat visual cortex. *European Journal of Neuroscience*, 20(2):495–502, 2004.
- E. Witten, I. H. & Frank. *Data Mining: Practical machine learning tools and techniques*. Morgan Kaufmann, 2005.
- Santiago Ramon y Cajal. *Comparative study of the sensory areas of the human cortex*. 1899.
- C. Zimmer, E. Labruyère, V. Meas-Yedid, N. Guillén, and J. Olivo-Marin. Segmentation and tracking of migrating cells in videomicroscopy with parametric active contours: A tool for cell-based drug testing. *IEEE Transactions on Medical Imaging*, 21:1212–1221, 2002.

CURRICULUM VITAE

Andrew Inglis

Boston University, Physics Department
Center For Polymer Studies
590 Commonwealth Avenue
Boston, Massachusetts 02215 USA

Telephone: 617-353-3891
Facsimile: 617/353-3783
E-mail: ainglis@bu.edu

EDUCATION

- 2010, Ph.D. Physics, Boston University, Boston, MA
Advisor: H. Eugene Stanley
Thesis: *Measuring neuron/glial cellular arrangement in the mammalian cortex.*
- 2002, M.A.T, Johns Hopkins University, Baltimore, MD
Advisor: Susan Small
- 2000, B.S., Engineering Science, University of Virginia, Charlottesville, VA
Thesis: *The design and creation of the heartbeat-music playback system.*

TEACHING EXPERIENCE

- 2004-2005, Chelsea School District, Chelsea, MA. *Teaching assistant*
- 2003-2004, Media and Technology Charter High School, Boston, MA. *Teacher*

- 2002-2003, KIPP Ujima Village Academy Charter Middle School, Baltimore, MD. *Teaching assistant*
- *summer* 2002, Center For Talented Youth, Pepperdine University, Malibu, CA. *Teacher*
- 2002-2000, Frederick Douglass High School, Baltimore, MD. *Teacher*
- *summer* 2000, Davis High School, Houston, TX. *Teacher*
- 1998-2000, University of Virginia, Charlottesville, VA. *Teaching assistant*

PROFESSIONAL RESPONSIBILITIES

- 2009, Reviewer for the *Proceedings of the National Academy of Sciences*
- 2007-2009, Chief computing system administrator Center for Polymer Studies at Boston University

AWARDS

- 2009, Best poster award at Science and Engineering Day, Boston University.
- 2006, Chairman Book Award, Physics Department, Boston University.

RESEARCH PAPERS

1. L. Cruz, B. Urbanc, A. Inglis, D. L. Rosene, and H. E. Stanley, "Generating a Model of the Three-dimensional Spatial Distribution of Neurons Using Density Maps," *Neuroimage* **40**, 1105-1115 (2008).
2. A. Inglis, B. Urbanc, L. Cruz, D. Roe, H. E. Stanley, and D. Rosene, "Automated Identification of Neurons and Their Locations," *Journal of Microscopy* **230**, 339-352 (2008).

3. L. Cruz, D. L. Roe, B. Urbanc, A. Inglis, H. E. Stanley, D. L. Rosene, "Age-Related Reduction in Microcolumnar Structure Correlates with Cognitive Decline in Ventral but Not Dorsal Area 46 of the Rhesus Monkey," *Neuroscience* **158**, 1509-1520 (2009).
4. R. Alvaro, H. Tomita, S. Ahlen, D. Avery, A. Inglis, J. Battat, D. Dujmic, P. Fisher, S. Henderson, A. Kaboth, G. Kohse, R. Lanza, J. Monroe, G. Sciolla, N. Skvorodnev, H. Wellenstein, R. Yamamoto. "A Background-Free Direction-Sensitive Neutron Detector," *Nuclear Instruments and Methods in Physics Research Section A* **608**, 2, 305-309 (2009).